Department of Chemistry

Density Functional Theory Investigation of Carbon- and Porphyrin-based Nanostructures

Victor Hugo Posligua Hernandez

Thesis submitted for the degree of

Doctor of Philosophy

Supervisor: Dr Ricardo Grau-Crespo

January 2021

Abstract

The present doctoral thesis examines the properties of carbon-based, porphyrin-based and hybrid carbon-porphyrin nanostructures as promising candidate materials for catalysis (including photocatalysis) applications. I use density functional theory simulations, together with experimental insights from collaborators, to both explain known behaviour and suggest ways in which these materials can be modified for improved catalytic efficiency.

Since the catalytic activity of graphitic materials is concentrated on the edges, I investigate their properties in several ways. First, I attempt to understand the properties of folded edges of graphitic nanostructures and quantify their thermodynamic stability, and explain how the application of an electric field leads to their opening. Edge folding can reduce catalytic activity by allowing bond saturation at the edge, but at the same time they provide a way to achieve highly porous carbon-based materials, which could be very useful for catalytic applications. My calculations rationalise the experimental observations about these folded edges. Additionally, I investigate catalysts based on carbon- and iron-based nanostructures, in collaboration with experimentalists. I present models for N-doped graphitic/ferrihydrite nanocatalysts for CO_2 reduction, and for Fe-N active sites in graphite-based catalysts.

In contrast with carbon nanostructures, porphyrin nanostructures exhibit a well-defined band gap which makes them more useful in photocatalytic applications. In this thesis I explore possible routes to engineer the electronic properties of two types of porphyrin-based materials. The first type consists of fully-organic porphyrin nanostructures with various dimensionalities, and we show how the length of the linkers

between porphyrin can be used to engineer their electronic band structures. The second type consists of two-dimensional (2D) porphyrin-based metal-organic frameworks, where we explored different strategies to optimise the photocatalytic behaviour, by changing metal centres, partially reducing the porphyrins or changing the bridges between the porphyrin units.

Finally, I consider mixed graphitic/porphyrinic structures, based on the idea that such composites could combine the advantages of both types of structures, leading to superior photocatalytic behaviour. I discuss the adsorption of porphyrins on the surfaces or edges of graphene nanoribbon, and how the interaction affects the electronic properties of the combined structures.

Overall, the thesis shows how computer simulation approaches can be used to understand, and also to design and optimise the electronic properties of carbon and porphyrin-based nanostructures to be applied in catalysis and photocatalysis.

List of publications

1. **The closed-edge structure of graphite and the effect of electrostatic charging**

   Victor Posligua, Joana Bustamante, Cesar H. Zambrano, Peter J. F. Harris, Ricardo Grau-Crespo.

   RSC Adv. **2020**, 10, 7994-8001.

   https://doi.org/10.1039/C9RA09913A

2. **Band structures of periodic porphyrin nanostructures**

   Victor Posligua, Alex Aziz, Renée Haver, Martin D. Peeks, Harry L. Anderson, Ricardo Grau-Crespo.

   J. Phys. Chem. C. **2018**, 122, 41, 23790-23798.

   https://pubs.acs.org/doi/10.1021/acs.jpcc.8b08131

3. **Operando spectroscopy study of the carbon dioxide electro-reduction by iron species on nitrogen-doped carbon**

   Chiara Genovese, Manfred E. Schuster, Emma K. Gibson, Diego Gianolio, Victor Posligua, Ricardo Grau-Crespo, Giannantonio Cibin, Peter P. Wells, Debi Garai, Vladyslav Solokha, Sandra Krick Calderon, Juan J. Velasco-Velez, Claudio Ampelli, Siglinda Perathoner, Georg Held, Gabriele Centi, and Rosa Arrigo.

   Nat. Commun. **2018**, 9, 935.

   https://www.nature.com/articles/s41467-018-03138-7

Manuscripts in press or in preparation

1. **Engineering the electronic and optical properties of 2D porphyrin-paddlewheel metal-organic frameworks**

   Victor Posligua, Dimpy Pandya, Alex Aziz, Miguel Rivera, Rachel Crespo-Otero, Said Hamad, Ricardo Grau-Crespo.

   Accepted in *J. Phys. Energy.*

   https://arxiv.org/abs/2011.06956

2. **Adsorption of porphyrin molecules at the surface of graphene and in-plane heterostructures of porphyrin linear chains at the edge of graphene nanoribbon**

   Victor Posligua, Umesh V. Waghmare, Ricardo Grau-Crespo.

To my parents,

you made me into who I am…

Declaration

I confirm that this is my own work and the use of all material from other sources has been properly and fully acknowledged.

Victor Hugo Posligua Hernandez

Acknowledgments

Although writing up the PhD thesis might be the effort of one person, the reason that person even gets as far as starting to write up is thanks to all the people supporting that PhD student. I am grateful for everyone who has been there to support my journey towards the finished thesis.

I am indebted to and grateful for my PhD supervisor, Dr Ricardo Grau-Crespo, for all the support and letting me find my own path whilst at the same time showing me which alternate paths I might be missing. Never forcing, always suggesting suits me perfectly.

Besides my supervisor, I would like to express my gratitude toward the collaborators of our group. Dr Rosa Arrigo at Diamond Light Source for her useful insights and inspiring motivation. Prof. Umesh Waghmare from JNCASR in Bangalore – India for his support during my visit to his group and also Prof. Aloysius Soon at Yonsei University in Seoul – Korea for giving me the valuable chance to collaborate with Dr Jongmin Yun and the rest of his team. Prof. Harry Anderson at University of Oxford for his support and valuable guidance through the porphyrin world. Dr Cesar Zambrano at Universidad San Francisco de Quito in Quito – Ecuador and Dr Peter Harris at University of Reading for their support to make possible one of our research collaboration and publication. Also, I would like to thank Dr Rachel Crespo-Otero, Dr Miguel Rivera and Dr Alex Aziz at Queen Mary University of London for the valuable contribution, effort and useful insights to improve my research. Also, I want to thank my examiners, Dr Pooja Goddard and Dr David Nutt for an intellectually stimulating and enjoyable viva.

I also want to thank the National Secretariat for Higher Education, Science, Technology and Innovation of Ecuador (SENESCYT) for the financial support to my final years of my PhD under the scholarship program "Convocatoria Abierta 2018". Computational time given by ARCHER, the UK's national high-performance computing service is also acknowledged.

I am appreciative to all the members of the Grau-Crespo's Materials Theory (GCMT) group past (Dr Alex Aziz and Dr Jorge Ontaneda) and present (Scott, Shivani and Furqan) who have made the office (our lab) a great place to be.

To my friends outside of Reading, in particular: Joana Bustamante, Diana Vargas and Marcos Becerra for all the support during my PhD and for been there for the important stuff.

Finally and most importantly, I want to dedicate this thesis to my parents and my sister. Thank you for everything! You have been a fundamental pillar in my life. With your love and unconditional support, you give me the strength and motivation to move forward. My last lines go to you, I would not be at this point if it had not been for your enormous belief and encouragement. Now I understand that it does not matter who hurt you or broke you down. What matters is who made you smile again.

Victor Posligua
Reading, September, 2020.

Contents

Do not be dismayed by the brokenness of the world.
All things break. And all things can be mended.
Not with time, as they say, but with intention.
So go. Love intentionally, extravagantly, unconditionally.
The broken world waits in darkness for the light that is you.

- L. R. Knost

1 Introduction

This thesis describes the computer simulations of nanostructures made of carbon and/or porphyrins, with potential applications in catalysis, photocatalysis and other functionalities. In this Chapter, I will introduce basic concepts related to these nanostructures, and summarise relevant previous work, to put ours in context.

1.1 Carbon nanostructures

The ability of carbon atoms to chemically bond with other carbon atoms (catenation property), creating large stable frameworks of interconnecting bonds with different hybridisation allows carbon to form a wide range of nanostructures with varying dimensionalities. There are several carbon allotropes including a few crystalline ones and many amorphous and semi-crystalline solids (for example lonsdaleite and chaoite), but the most recognised forms are the crystalline ones of diamond and graphite.

A recent addition to this large family of carbon structures is graphene. This is an allotrope whose structure is a single layer of hexagonal arrangement of sp^2-bonded carbon atoms (which are among the strongest bonds in nature, even stronger than carbon bonds in diamond). This name was first given by Mouras *et al.* [1] to describe a single layer of graphite. Nowadays, graphene has become a material of significant scientific and technological interest due to its outstanding electrical and mechanical performances, high specific surface area and stability [2-8].

Graphene is a two-dimensional (2D) sheet of carbon atoms in which each carbon atom is bound to its three neighbours to form the honeycomb structure (see **Figure 1.1a**). In graphite, its three-dimensional (3D) parent structure, each graphene layer is arranged

such that half of atoms lie directly over the centre of a hexagon in the lower graphene sheet, and half of the atoms lie directly over an atom in the lower layer. This stacking of graphene layers is called the Bernal stacking (see **Figure 1.1b**). Other types of stacking can also occur, and they give different electronic properties to graphite.

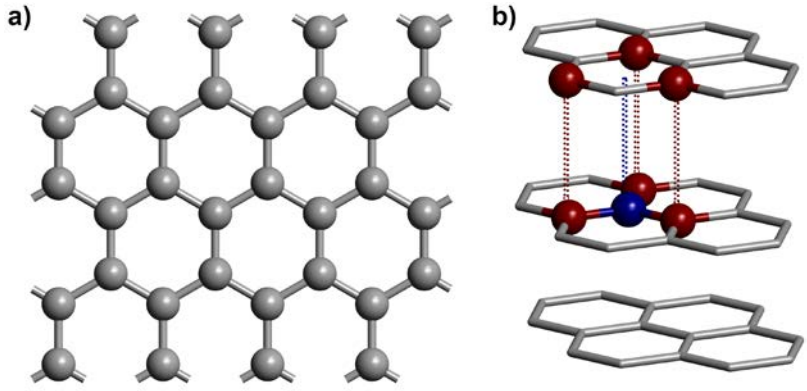

Figure 1.1. a) Crystal structure of graphene showing the honeycomb structure and b) graphite with the Bernal or AB stacking (dark blue carbon atoms are over the centre of the hexagons in the adjacent layers and dark red carbon atoms are stacked exactly below or above each other.

Due to their sp^2 bonds, graphene has an exceptional stability which is very important for electronic applications and especially for nanoelectronics, where structures are subjected to extremely large thermal and electrical stresses. The most important graphene properties emerge from the unique band structure of this material, which will be explained in detail in the next sections.

In contrast to the very strong bonds between the carbon atoms in a graphene sheet, the inter-sheet van der Waals (vdW) bonding in graphite is more than 100 times weaker and ranks among the weakest bonds. This very weak interlayer bond causes the layers to become essentially decoupled from each other, which produces large anisotropies in the electronic and thermal properties. Also, these thin graphene layers are easily mechanically cleaved from a larger graphite crystal by rubbing it against a surface, for example paper,

causing the familiar pencil trace. In fact, graphite derives its name from this property since *graphein* is Greek for *to draw* [9].

Several other graphitic nanostructures, for example carbon nanotubes (CNTs), are directly related to graphene. CNTs can be seen as rolled up graphene sheets [10], and the CNT properties are most easily described and understood in terms of those of graphene [11].

Carbon nanotubes are classified based on their curvature and chirality. In an unwrapped representation of a nanotube (basically graphene sheet), the chirality describes how the hexagonal structure of the graphene lattice is orientated with respect to the axis of the tube. In **Figure 1.2**, it is clear how the desired chirality can be achieved. In this graphene sheet, the one of the carbon atoms is the origin. Picking this point up and curling the sheet onto one of the labelled atoms that fall between the two vectors creates a unique CNT. Due to the symmetry of graphite lattice, only those atoms between the two vectors need to be considered for a unique tube. The vector pointing from the origin to the atom picked to describe the CNT is known as the chiral vector ($\overrightarrow{C_h}$), which is defined in terms of the graphene lattice vectors labelled $\vec{a}$ and $\vec{b}$ as:

$$\overrightarrow{C_h} = n\vec{a} + m\vec{b} \equiv (n, m) \qquad (1.1)$$

where *n* and *m* are integers.

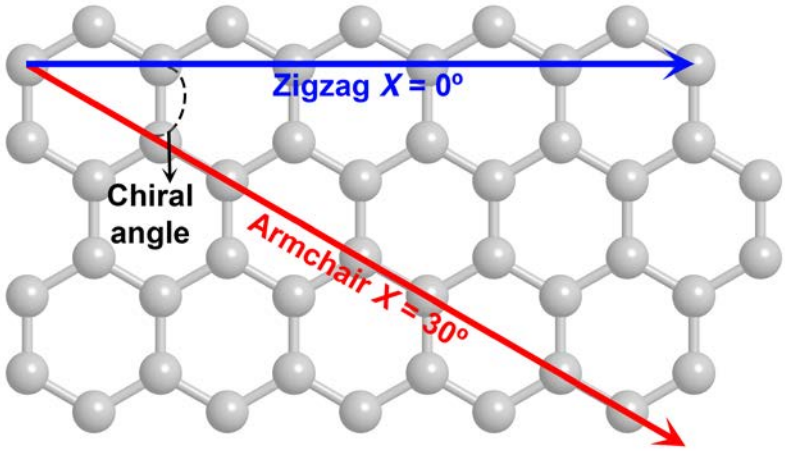

Figure 1.2. Chirality described by CNTs wrapping angle of a graphene sheet.

The angle formed by the $\overrightarrow{C_h}$ and $\vec{a}$ is called chiral angle (χ). CNTs with χ = 0º are known as zigzag nanotubes and are described by the chiral vector (*n*,0). The moniker of zigzag comes from the sawtooth like structure that is found around the tube circumference. When χ = 30º, the nanotube edges exhibit the so-called armchair termination and these are defined by the case when *n* = *m*, *i.e.* the chiral vector is (*n*,*n* or *m*,*m*). All other tubes that fall between these limits are referred to as chiral tubes (*n*,*m*). In **Figure 1.3** we show some examples of these terminations.

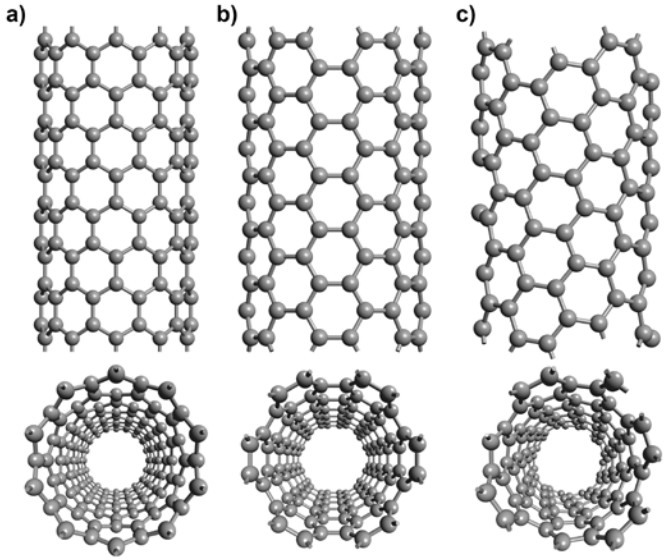

Figure 1.3. CNTs with a) zigzag, b) armchair and c) chiral terminations.

Nanotubes can exist as single layered structures known as single-walled carbon nanotubes (SWCNTs) or can be composed by several coaxial SWCNTs nested inside one another and referred to as multi-walled carbon nanotubes (MWCNTs).

1.1.1 The electronic structure of graphene

Graphene is not a metal, is it essentially a giant organic molecule and technically a zero-gap semiconductor. The electrons follow the π bonds that connect neighbouring atoms when they travel from one atom to the next. In contrast to metals, the electrons in graphene

interact with the lattice in such a way that they appear to be massless (in metals, electrons behave more like as normal massive particles).

In graphene, four valence electrons in the carbon atoms form the chemical bonds with neighbouring carbon atoms. The orbitals of these electrons in graphene arrange in such a way to produce three covalent sigma bonds with neighbouring atoms in the plane. The electrons participating in these bonds give the graphene sheet its exceptional strength. While electrons in the sigma bonds do not participate in the electronic transport, they provide the rigid scaffolding (*i.e.* the rigid hexagonal honeycomb structure) of the graphitic system.

All the electronic properties result from the fourth valence electron of each carbon atom. From this point, whenever we talk about electrons in graphene, we will be referring to these electrons, ignoring the sigma bonded ones. For each carbon atom, the electron is centred on the carbon atom and oscillates up and down through the graphene plane. This up and down motion produces a quantum-mechanical p_z orbital. This orbital consists of two lobes (charge density clouds): one above and one below the graphene sheet (**Figure 1.4**). The motion of the p_z electrons on two neighbouring atoms can be in-phase or out-of-phase with each other. Moreover, the orbitals on neighbouring atoms slightly overlap. The energy of a pair of neighbouring p_z orbitals decreases when their relative motion is in-phase with each other, and it increases when the motion is out-of-phase. Hence, when the motion is in-phase, the pair is said to be in a bonding (attractive) configuration, and when they are 180º out-of-phase, they are in an antibonding (repulsive) configuration. In general, the interaction strength can have any intermediate value depending on the relative phase.

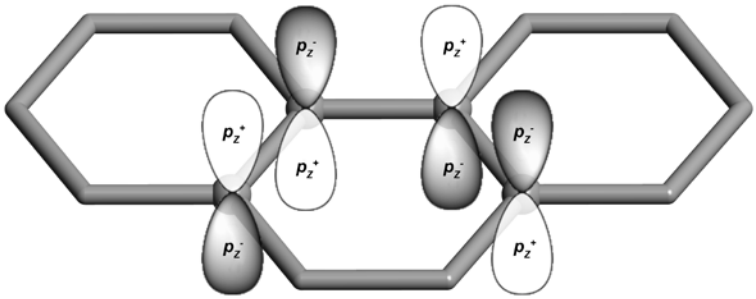

Figure 1.4. p_z^+ and p_z^- orbitals of carbon atoms in graphene.

Due to the non-negligible overlap of the p_z orbitals on neighbouring atoms, the electrons readily "hop" from one atom to its neighbours. This hopping is so rapid that it is impossible to associate a specific electron with a specific atom.

1.1.2 Quantum-mechanical approach of electronic structure of graphene

In the quantum mechanical picture, each electron is described as a wave that extends over the entire surface of graphene sheet. This electron has a specific phase and amplitude at each atom. The total energy of the electron wave is found by summing the energy at each bond, thereby by weighting the amplitude of the electron wave at each atom with a factor that depends on the relative phase of the electron ϕ_{ij} wave at neighbouring atoms *i*, *j*: $E = -\gamma \sum|\Psi(i)||\Psi(j)|\cos(\phi_{ij})$, where $\gamma \approx 3$ eV represents the energy due to the overlap of neighbouring p_z orbitals. Two extreme cases of electron waves can be easily visualised: the first one is when $\phi = 0$ (all in-phase) and $|\Psi| = 1/\sqrt{N}$ at each atom. In this case the total energy of the wave is $E_- = -3\gamma$. In the other case, $\phi = \pi$ so that the wave is exactly out-of-phase at each atom and $E_+ = +3\gamma$. Waves with all intermediate values can be constructed. Those waves for which the total energy is exactly 0 are special as these define the Fermi surface for neutral graphene.

As demonstrated in the two extreme examples above for neighbouring p_z orbitals, the electron waves come in two varieties: π and π^* representing bonding and antibonding

waves, respectively. While for a finite graphene sheet, the electron waves are standing waves, in an infinite sheet they are more aptly represented as traveling waves.

A traveling electron wave in graphene is much like a light wave (photon). It has a wavelength, a direction of propagation, energy, and momentum. It is specifically not a small, localised charged object. Indeed, whereas the spread-out nature of a photon appears more natural, in fact when photons are absorbed, they behave like discrete particles. This particle/wave dichotomy is inherent in the quantum mechanical description of matter.

The momentum p of the electron in a π (or π^*) state is given by $p = hk/2\pi$, where h is Planck's constant and k is the wave number which is a vector of magnitude $2\pi/\lambda$ that points in the propagation direction, and where λ is the wavelength. The energy of a π or a π^* electron, with wave number k propagating in the x direction (perpendicular to a hexagon edge) is $E = \pm hk\left(1 + 2\cos(\pm kd/2)\right)$; (- for π and + for π^*) where d = 0.26 nm, which is the graphene lattice constant. This equation describes the π and π^* energy bands as first found by Wallace *et al.* [12] (see **Figure 1.5a**). The two energy bands cross when $k = K = +4\pi/3d$ and $k = K' = -4\pi/3d$ where $E = 0$. These energy bands have been directly measured by angle resolved photoemission by researchers at Berkeley (see **Figure 1.5b**) [13, 14].

Electrons and fermions (as a result of their half-integer spin which can be either up or down). Consequently, as for all fermions, no two electron waves (of similar spin) in graphene can have exactly the same momentum and energy. This property (Heisenberg exclusion principle) dictates the electronic structure of the graphene.

The electronic structure is found by filling up in energy the π and π^* bands with all the electrons (the fourth valence electron of each carbon atom) in the graphene sheet consistent with the exclusion principle. Hence, starting with the electron with the least energy at the bottom of the π band, electrons are added one by one, until all N electrons

are included. In that situation, the graphene sheet is neutral (since one electron was added for each carbon atom). This procedure fills the bands up to a maximum energy (Fermi energy), which corresponds exactly to the energy of the *K* and *K'* points in neutral graphene. If the sheet is negatively charged, the additional electrons cause the Fermi level to rise to higher energies; if it is positively charged, the Fermi level is lowered.

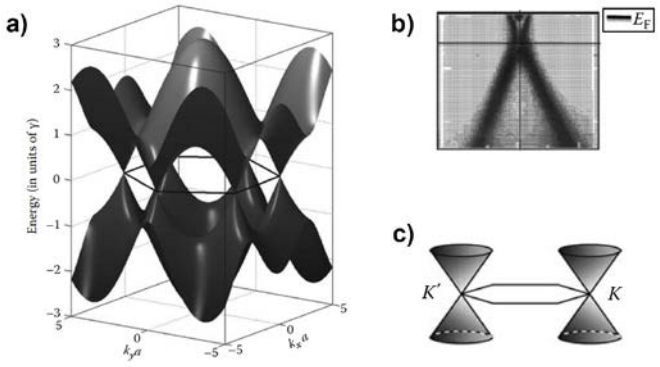

Figure 1.5. a) Calculated band structure of graphene where the valence band meets the conduction band at Dirac points (Figure obtained from Ref. [9]) and b) band structure of graphene measured by angle-resolved photoemission spectroscopy (Figure obtained from Ref. [12]). c) Energy of electron waves at *K* and *K'* points (Figure obtained from Ref. [9]).

It is evident that near the *K* and *K'* points (see **Figure 1.5c**) the energy of the electron waves varies linearly with momentum (*i.e.* with k) as $E = \pm c^* p^*$ where p^* is the momentum measured from the *K* point and $c^* \approx 10^6$ cm s^{-1}. It turns out that taking all directions in the plane into account, this relation still holds: $E = \pm c^* |p^*|$. This is a very interesting situation that is reminiscent of the energy-momentum relation (dispersion relation) of a photon: $E = c|p|$ where p is the momentum of the photon: $p = \hbar k/2\pi$ and k is the wave number. In this case, c is the speed of light. Hence, the dispersion relation of graphene resembles that of a photon, which implies that the velocity of electrons in graphene (its Fermi velocity) is $c^* \approx 10^6$ cm s^{-1}, independent of its energy. This property, that the electron velocity is independent of its energy, provides it with the massless quality

of a photon; however, the speed of these particles is a factor of 300 smaller than the speed of light. It is worth mentioning that in most materials the band structure gives rise to unusual effective masses that range from 0 to ∞. These "effective masses" reflect the property of electrons in a material and not at all the actual masses of the particles involved.

Examining the graphene dispersion relation more carefully reveals that near the Fermi level it is described by two pairs of cones (see **Figure 1.5c**), one pair with its apexes touching the *K* point and the other pair touching the *K'* point. In neutral graphene, the electrons fill the π and π* bands up to the *K* and *K'* points (that is the bottom cones), while above the *K* and *K'* points (that is the top cones) are empty. The facts that there are bottom-filled cones and top-unfilled cones and that the electrons are fermions, indicate that the electrons in graphene actually resemble massless fermions, like neutrinos rather than photons. The cones that define the band structure are referred to as Dirac cones and the *K* and *K'* points as "Dirac points".

Knowing the band structure of graphene allows one to predict some of its electronic transport properties. An electric field E applied to the electrons forces them to move. Specifically, only electrons near the Fermi level (charge carriers) can move by shifting from occupied levels to unoccupied levels. Consequently, the current density J is given by $J = \sigma E$, where the conductivity $\sigma = e^2ND$. Here e is the electronic charge, D is the electronic diffusivity, proportional to the electron mobility μ, and N is the density of states at the Fermi level E_F. The density of states is the number of states per unit energy and per unit area that are available for electrons. Therefore, at the Fermi energy, N reflects the number of charge carriers in the material. In graphene, the density of states at E_F is proportional to the circumference of the circle that is defined by the intercept of E_F and the Dirac cones. For negatively doped graphene (electron doped), E_F is above the Dirac point and for positively doped graphene (hole doped) E_F is below the Dirac point.

Moreover, it is interesting how N varies linearly with E_F and that for neutral graphene $E_F = 0$ so that $N = 0$.

The vanishing of the density of states at E_F in neutral graphene is reminiscent of a zero-gap semiconductor (graphene is actually a semi-metal). In either case, it might be expected that the conductivity of graphene increases with E_F (*i.e.*, with the degree of electron doping) and that it vanishes at zero doping.

As mentioned before, graphite consists of graphene sheets that are Bernal stacked. Even though the layers are only very weakly coupled, the electronic structure especially near the Fermi level is profoundly affected. This is because of the fact that once a second layer is placed over the first one, every second carbon atom in one sheet has an atom in the other sheet directly above it. This causes a lifting of the graphene symmetry in which all atoms are essentially identical.

1.2 Porphyrin-based nanostructures

From the previous section, graphene is responsible for the renewed interest in 2D electronic systems and it can be considered as the starting material for other low-dimensional carbon-based systems [15]. Recently, half-metals based on graphene and organic materials have been studied with motivation to use them in innovative electronic devices [16, 17]. Organometallic monolayered sheets are promising candidates for this purpose because of their magnetic properties suitable for these applications, such as porphyrin-based systems [15].

Porphyrins are stable functional dyes with large extinction coefficients in the visible light region, photochemical electron-transfer ability and rigid structures. They have potential applications in photoharvesting, sensing and photoelectronic devices [18-21]. Due to these properties, porphyrin arrays are potentially good photosynthetic models, in which geometry (distances and angles between components of the structure) strongly

affect the efficiency and rate of photosynthetical processes [22]. The multifunctionality of porphyrin molecules lies in the combination of the redox properties of the metal and its rigid planar aromatic structure which allows such complexes to play relevant roles in electron transfer and light-harvesting processes [23]. It was shown that the immobilisation of molecular species such as cobalt-centred porphyrins on graphite and graphene raises possibilities for multistep reduction products [24, 25].

Recently, porphyrin-based nanostructures have been shown to exhibit properties that facilitate various applications such as optoelectronic [26, 27], hydrogen storage [26], conducting molecular wires [28], spintronics [15, 27, 29], water-splitting photocatalysis [30] and light-harvesting devices [31].

1.2.1 Structure of porphyrin units

The word porphyrin is derived from the Greek *porphura* meaning purple. They are in fact a large class of deeply coloured pigment, of natural or synthetic origin, having in common a substituted aromatic macrocycle ring and consists of four pyrrole rings linked by four methine bridges [32, 33].

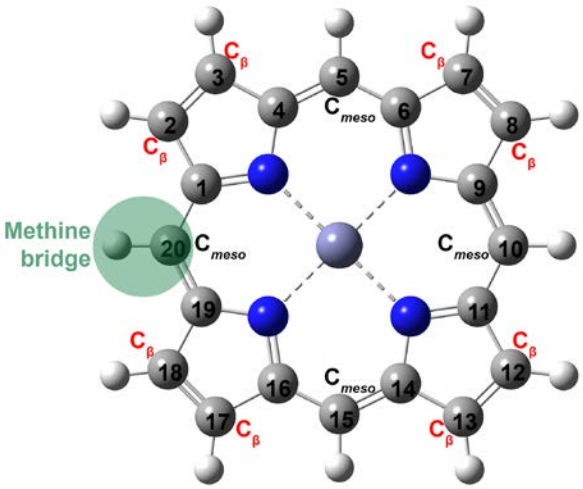

Figure 1.6. Structure of porphyrin with D_{4h} symmetry and nomenclature for carbon atoms (*meso*-substituents = C_{meso}, β-substituents = C_β). Green-shaded circle shows the methine bridge.

The simplest porphyrin, known as porphin, has no substituents on the periphery of the macrocycle. Porphin can be easily functionalised; substituents on the methine carbons are known as *meso*-substituents (C_{meso}) and those on the β positions (C_β) of the pyrrole units are known as β-substituents (see **Figure 1.6**). The nitrogen atoms pointing toward the centre of the macrocycle can ligate to various metals. The strength of this coordination increases with electronegativity and charge of the metal ion and depends on the ionic radius [33]. Zinc atoms form stable complexes with porphyrins, and the resulting complex can reversibly bind another ligand perpendicular to the plane of the ring.

Porphyrins have attracted considerable research attention because they are ubiquitous in natural systems and have prospective applications in mimicking enzymes, catalytic reactions, molecular electronic devices, conversion of solar energy and light-harvesting. Their important roles in nature is due to their special absorption, emission, charge transfer and complexing properties as a result of their characteristic ring structure of conjugate double bonds [34].

1.2.2 Optoelectronic properties

The UV-vis absorption spectra of porphyrins consist of an intense transition in the 380 – 500 nm range (Soret or B band) and a weaker transition at lower energies (500 – 750 nm range) called Q band [35]. The Q band arises from a transition from the ground state to the first singlet excited state ($S_0 \rightarrow S_1$), and the Soret band from a transition from the ground state to the second singlet excited state ($S_0 \rightarrow S_2$). The absorption spectra of metalloporphyrins are largely similar regardless of the coordinated ion [35], indicating that absorption in the visible region of the spectrum is due to π-π* transitions.

The Gouterman four-orbital model can be used to describe these transitions [36]. The highest occupied molecular orbital (HOMO) of an unsubstituted metalloporphyrin monomer with D_{4h} symmetry consists of two orbitals: a_{1u} and a_{2u} which are close together

in energy. The lowest unoccupied molecular orbital (LUMO) consists of two orbitals $e_{g(x)}$ and $e_{g(y)}$, which are degenerate due to the porphyrin symmetry. Instead of producing two coincident absorption bands due to $a_{1g} \rightarrow e_g$ and $a_{2u} \rightarrow e_g$ transitions, the transitions interact with one another in a process of configurational interaction. Constructive interference of the transitions results in the high intensity Soret band and destructive interference gives the weaker Q band (see **Figure 1.7**).

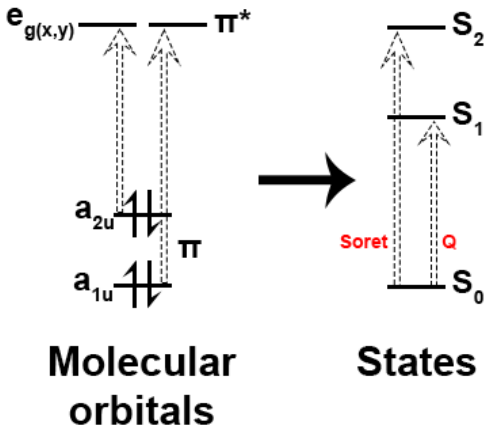

Figure 1.7. Configurational interaction of the $a_{1u}e_g$ and $a_{2u}e_g$ transitions leads to the Soret and Q bands seen in the absorption spectra of D_{4h} symmetric porphyrin molecule.

While variations of the peripheral substituents on the porphyrin ring often cause minor changes to the intensity and wavelength of the absorption features, protonation of two of the inner nitrogen atoms or the insertion/change of metal atoms into the macrocycle usually strongly change the visible absorption spectrum.

When the porphyrinic macrocycle is protonated or coordinated with any metal, there is a more symmetrical situation than in the porphyrin free base and this produces a simplification of Q bands pattern for the formation of two Q bands.

1.2.3 Porphyrins in nature

As explained above, the absorption bands of porphyrins significantly overlap with the emission spectrum of the solar radiation reaching the biosphere, resulting in efficient tools

for conversion of radiation to chemical energy. In such a conversion, the favourable emission and energy transfer properties of porphyrin derivates are indispensable as in the case of chlorophylls, which contain magnesium ion in the core of the macrocycle. Also, metalloporphyrins can be used in artificial photosynthetic systems, modelling the most important function of the chlorophyll pigments in plants [34].

Photosynthesis is a process whereby photosynthetic organisms fix solar energy into a chemically useful form. The initial "light" stages of this process occur in protein-pigment complexes embedded in the photosynthetic membrane of the cell. These protein-pigment complexes known as photosystems consists of two major components: the light harvesting complex and the reaction centre. The role of the light harvesting complex is to capture incident solar radiation and efficiently funnel it to the reaction centre, where the resulting charge separation powers the production of adenosine triphosphate (ATP), and ultimately reduces atmospheric carbon dioxide to complex sugars.

The light harvesting complex is comprised of a protein scaffold that supports a mixture of chlorophyll and carotenoid pigments, which absorb solar radiation and transfer this energy by Förster resonance energy transfer to the reaction centre. Chlorophylls are more saturated derivatives of a porphyrin. Plant chlorophylls have the C17-C18 double bond missing (see **Figure 1.6** for reference) giving stereochemistry at two β-pyrrole positions and are called "chlorins" (see **Figure 1.8**) [32]. Although the stereocentres impact on their biological properties, the 18 π electron delocalisation pathway of porphyrins is conserved, so their optical and photophysical properties are similar.

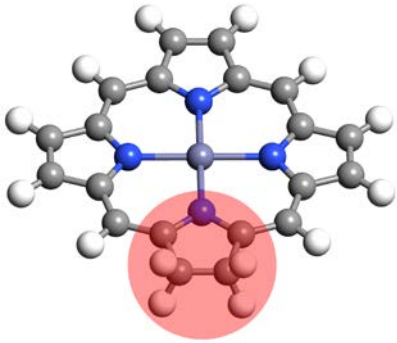

Figure 1.8. Structure of chlorin where the C_β atoms of the red-shaded pyrrole are reduced.

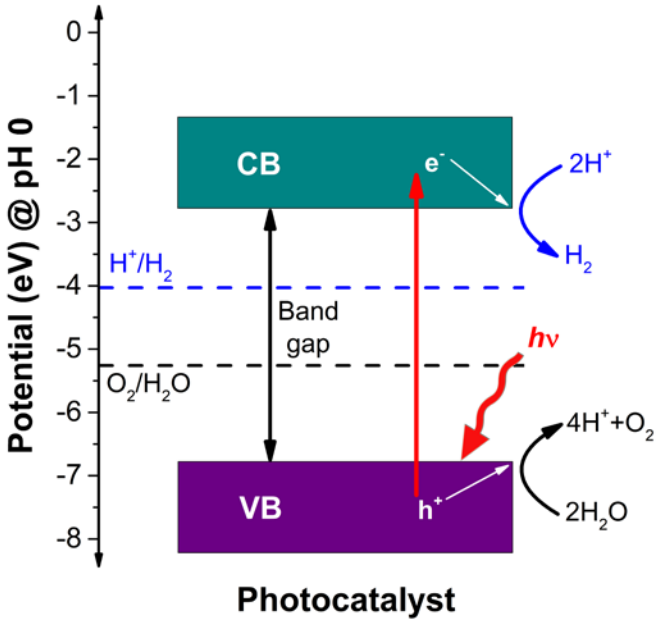

Figure 1.9. Energy diagram of photocatalytic water-splitting.

The light-absorbing power of porphyrins and related compounds makes them very interesting for photocatalytic applications, *i.e.* water-splitting. **Figure 1.9** exhibits a simplified schematic of the reaction processes involved in photocatalytic water-splitting. A photocatalyst needs to have a band gap between the conduction band (CB) and the valence band (VB). When the photocatalyst absorbs photons with sufficient energy, the electrons in the VB are excited into the CB, leaving positive holes in the VB. For efficient photocatalysis, this electron-hole pair must be separated, and both the excited electron and excited hole should travel to the surface of the catalyst where the oxidation and reduction

half-reactions take place. The photogenerated carriers can drive reduction (electrons) and oxidation (holes) reactions if the energy level for charge injections makes these processes thermodynamically favourable. Therefore, to achieve an overall water-splitting reaction, valence and conduction bands must straddle the redox potentials for the photocatalytic reaction. The VB edge should be below the energy of the oxygen evolution reaction (OER) while the conduction band edge should be above the energy of the hydrogen evolution reaction (HER). The redox potentials values in the vacuum scale for water-splitting at a neutral pH and room temperature are -5.26 eV and -4.03 eV for OER (O_2/H_2O) and HER (H^+/H_2), respectively.

1.3 Designing graphene/porphyrin materials

As explained above, the properties of graphene, arising from its 2D sp^2 hybridised carbon lattice, make it an enticing material for developing novel carbon-based electronics and a formidable playground to explore fundamental solid-state physics [8, 37]. Due to its excellent electronic conductivity, mechanical properties, and large specific surface area, graphene is considered as a suitable component for solar energy conversion systems, including artificial photosynthesis and photovoltaic devices [38-43].

The covalent chemistry of graphene has become a hot topic recently, since it can realise the combination of the properties of graphene with functional molecular and periodic systems [18, 44]. For example, porphyrins can interact with various carbon materials, such as graphite, fullerenes and carbon nanotubes, through π-π interactions that take place between their electron-abundant aromatic cores and conjugated surfaces of the carbon materials, making them photoactive [45-47]. Therefore, similar interactions are expected to occur between graphene and porphyrins.

1.3.1 Combining graphitic systems with porphyrin units/nanostructures

As explained in previous sections, porphyrins have remarkable properties that make them the best option for charge transfer interaction between graphitic systems. For example, strong interactions between reduced graphene oxides and 5,10,15,20-tetrakis(1-methyl-4-pyridinio)porphyrin tetra(p-toluenesulfonate) (TMPyP) has been evidenced by a red shift in porphyrin absorbance (see **Figure 1.10**) [45].

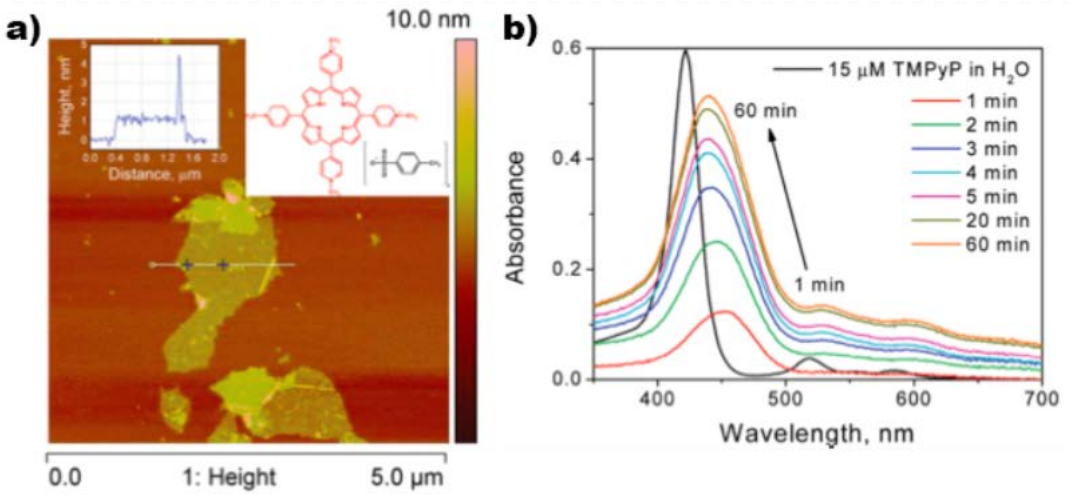

Figure 1.10. a) AFM image of single-sheet reduced graphene oxide with depth profile along the line of interest on reduced graphene oxide sheet. b) Adsorption of TMPyP on reduced graphene oxide film monitored by UV-vis spectroscopy. (Figures from Ref. [45])

Another approach in the formulation of hybrid nanostructured materials combining graphene and porphyrins has been reported for visible light photocatalytic applications. For this purpose, different porphyrin monomers (free or Zn complexed) were performed and as a result these systems showed a degradation efficiency greater in the visible-light range much higher than other similar devices containing nanoporphyrin units reported in literature [48].

Also nanohybrid materials have been reported, for example the fabrication of systems using graphene/TiO_2/self-assembled tetrakis (4-carboxyphenyl) porphyrin, which exhibited promising photocatalytic degradation of Rhodamine B under simulated sunlight

with excellent stability [49]. Also, porphyrin-based architectures had been considered for photovoltaic applications incorporating Zn-porphyrin and ZnO nanoparticles. These structures were used as model systems to probe the effectiveness of reduced graphene oxide in promoting the charge separation and charge transport in dye-sensitised solar cells [50]. The inorganic/organic architecture built with reduced graphene oxide/ZnO/porphyrin utilised a unique electron transfer cascade beginning with photoexcitation of the Zn-porphyrin.

Porphyrins can also be used in a new method to prepare graphene via exfoliation of graphite [47]. Graphite was dispersed in solutions of 5,10,15,20-tetraphenyl-21*H*, 23*H*-porphyrin and its derivatives containing functionalised alkyl groups at the *para*-positions of benzene rings. It has been shown that alkyl chains improve the π-π interactions of the porphyrins with graphene, which enhance the exfoliation promoting undisturbed sp^2 carbon networks [47].

Other studies of porphyrins have shown that these macrocycles are highly versatile to exfoliate graphite and to afford functional nanographene based charge-transfer hybrids. For this purpose, 5,10,15,20-tetrabutylporphyrin and its copper complex were used [51]. The formation and characterisation of novel nanographene/porphyrin hybrids and their implementation into solar cells have been reported, providing solid evidence for shifting electron density from the porphyrins to nanographene upon excitation [51].

Another application of porphyrin/graphene hybrid systems is based on the ability of porphyrins to change their magnetism in the presence of graphene. Recent progress in this area has shown that the introduction of defects in graphene show ferromagnetic and antiferromagnetic exchange interactions between a Ni (111) surface and iron-porphyrin [52]. This theoretical study suggests a new way of manipulating molecular magnetism that could lead to robust spin qubits for spin logic operations.

In the same line of magnetism within porphyrin-based systems, recent improvement has been achieved designing nearly perfect spin filters using porphyrin covalently coupled to graphene edges [44]. In this theoretical work, considered *M*-porphyrins (*M* = Cr, Mn, Fe and Co) decorating the graphitic terminations. Mn-porphyrin/graphene hybrid system exhibits an extremely high spin polarisation coefficient in a parallel magnetic configuration. Their results confirm that the magnetic configuration plays an important role in realising high-performance spin filter.

Finally, porphyrin molecules have been used to create graphene-based sensors. The interaction of these molecules with nitrogen-doped graphene has been investigated using scanning tunnelling microscopy and *ab initio* calculations [37]. It was explained that, due to the high polarizability of graphene, the adsorption of porphyrin induces a charge rearrangement on the substrate. This charge polarisation is enhanced around nitrogen site, leading to an increased interaction of molecules with their image charges on graphene.

Through all these interesting applications of porphyrins interacting with graphitic structures, it is evident that in most cases the key to achieve this interaction is the use of specific functional groups as linkers to decorate or incorporate the porphyrin units or nanostructures within the carbon-based ones.

1.3.2 Objectives of the thesis

The central objective of this thesis is to advance our understanding of the properties of carbon-based, porphyrin-based and hybrid carbon-porphyrin nanostructures, so that we can suggest ways to enhance their catalytic and photocatalytic behaviour.

Below we set more specific objectives and associate them with the work we present in each chapter:

- To understand the fundamental concepts and methods implemented in the calculations through all the nanostructures mentioned above (**Chapter 2**).

- To explore carbon- and porphyrin-based nanomaterials in terms of their interlayer interactions and bending stiffness and compare them with experimental results in order to validate the methods employed in this thesis (**Chapter 3**).
- To study the inter and intralayer interactions of graphitic structures to know the thermodynamics of the closed edges of graphite and how the application of an electric field leads to the separation of the folded edges (**Chapter 4**).
- To investigate the role of pyridinic N dopants in stabilising the interface between graphite and the iron oxo-hydroxide particles useful for CO_2 reduction reaction activity of these nanostructures supported on oxygen- and nitrogen-doped graphite (**Chapter 5**).
- To obtain the band structures of porphyrin nanostructures and understand the electronic properties of linear chains, 2D nanosheets and nanotubes made of Zn-porphyrins, which are connected by butadiyne (C4) or ethyne (C2) linkers or "fused" (C0), *i.e.* with no linker. These results are useful to evaluate the ability of these materials to tune light absorption by changing the linkers and use them for artificial photosynthesis (**Chapter 6**).
- To explore and evaluate possible routes to engineer the electronic properties of two-dimensional (2D) porphyrin-based metal-organic frameworks (MOFs) for photocatalysis (**Chapter 7**).
- To theoretically investigate a range of arrays including adsorbed porphyrin molecules on the top of graphene surface and also at the interface of the zigzag edges of graphene nanoribbon, in order to predict their structural and electronic properties in terms of their interactions (**Chapter 8**).

Although there are different goals here, the overarching theme of this thesis is that we can use computer simulations based on modern electronic structure theory to not only understand, but also to find routes to engineer the electronic and catalytic properties of these nanostructures. In particular, I hope that this work will stimulate new efforts to design more efficient photocatalysts, taking simultaneous advantage of the excellent conducting properties of graphitic structures, and of the ability of porphyrins to absorb light.

1.4 References

1. Hamwi, A., et al., *New synthesis of first stage graphite intercalation compounds with fluorides.* Journal of Fluorine Chemistry, 1987. **35**(1): p. 151.
2. van Engers, C.D., et al., *Direct Measurement of the Surface Energy of Graphene.* Nano Letters, 2017. **17**(6): p. 3815-3821.
3. Li, D. and R.B. Kaner, *Graphene-Based Materials.* Science, 2008. **320**(5880): p. 1170.
4. Katsnelson, M.I., *Graphene: carbon in two dimensions.* Materials Today, 2007. **10**(1): p. 20-27.
5. Rao, C.N.R., et al., *Graphene, the new nanocarbon.* Journal of Materials Chemistry, 2009. **19**(17): p. 2457-2469.
6. Rao, C.N.R., et al., *Graphene: The New Two-Dimensional Nanomaterial.* Angewandte Chemie International Edition, 2009. **48**(42): p. 7752-7777.
7. Rao, C.N.R., et al., *Some Novel Attributes of Graphene.* The Journal of Physical Chemistry Letters, 2010. **1**(2): p. 572-580.
8. Geim, A.K. and K.S. Novoselov, *The rise of graphene.* Nature Materials, 2007. **6**: p. 183.
9. Sattler, K., *Handbook of Nanophysics.* Vol. Functional Nanomaterials. 2010, Boca Raton: CRC Press.

10. Iijima, S., *Helical microtubules of graphitic carbon.* Nature, 1991. **354**(6348): p. 56-58.

11. Dekker, C., *Carbon nanotubes as molecular quantum wires.* Physics Today, 1999. **52**: p. 22-28.

12. Wallace, P.R., *The Band Theory of Graphite.* Physical Review, 1947. **71**(9): p. 622-634.

13. Ohta, T., et al., *Controlling the Electronic Structure of Bilayer Graphene.* Science, 2006. **313**(5789): p. 951.

14. Rollings, E., et al., *Synthesis and characterization of atomically thin graphite films on a silicon carbide substrate.* Journal of Physics and Chemistry of Solids, 2006. **67**(9): p. 2172-2177.

15. Singh, H.K., P. Kumar, and U.V. Waghmare, *Theoretical Prediction of a Stable 2D Crystal of Vanadium Porphyrin: A Half-Metallic Ferromagnet.* The Journal of Physical Chemistry C, 2015. **119**(45): p. 25657-25662.

16. Son, Y.-W., M.L. Cohen, and S.G. Louie, *Half-metallic graphene nanoribbons.* Nature, 2006. **444**: p. 347.

17. Kan, E.-j., et al., *Half-Metallicity in Organic Single Porous Sheets.* Journal of the American Chemical Society, 2012. **134**(13): p. 5718-5721.

18. Dasler, D., et al., *Direct Covalent Coupling of Porphyrins to Graphene.* Journal of the American Chemical Society, 2017. **139**(34): p. 11760-11765.

19. Wang, H.-X., et al., *Photoactive graphene sheets prepared by "click" chemistry.* Chemical Communications, 2011. **47**(20): p. 5747-5749.

20. Wang, A., et al., *Covalent functionalization of reduced graphene oxide with porphyrin by means of diazonium chemistry for nonlinear optical performance.* Scientific Reports, 2016. **6**: p. 23325.

21. Zargari, S., R. Rahimi, and A. Yousefi, *An efficient visible light photocatalyst based on tin porphyrin intercalated between TiO2–graphene nanosheets for inactivation of E. coli and investigation of charge transfer mechanism.* RSC Advances, 2016. **6**(29): p. 24218-24228.

22. Paschenko, V.Z., et al., *Excitation energy transfer in covalently bonded porphyrin heterodimers.* Optics and Spectroscopy, 2012. **112**(4): p. 519-527.

23. Jiménez Castillo, U., A.E. Torres, and S. Fomine, *Zinc-, cadmium-, and mercury-containing one-dimensional tetraphenylporphyrin arrays: a DFT study.* Journal of Molecular Modeling, 2014. **20**(4): p. 2206.

24. Shen, J., et al., *DFT Study on the Mechanism of the Electrochemical Reduction of CO_2 Catalyzed by Cobalt Porphyrins.* The Journal of Physical Chemistry C, 2016. **120**(29): p. 15714-15721.

25. Genovese, C., et al., *Operando spectroscopy study of the carbon dioxide electro-reduction by iron species on nitrogen-doped carbon.* Nature Communications, 2018. **9**(1): p. 935.

26. Zhu, G., et al., *Porphyrin-based porous sheet: Optoelectronic properties and hydrogen storage.* International Journal of Hydrogen Energy, 2015. **40**(9): p. 3689-3696.

27. Albert, I.D.L., T.J. Marks, and M.A. Ratner, *Large Molecular Hyperpolarizabilities. Quantitative Analysis of Aromaticity and Auxiliary Donor−Acceptor Effects.* Journal of the American Chemical Society, 1997. **119**(28): p. 6575-6582.

28. Kang, B.K., et al., *Length and temperature dependence of electrical conduction through dithiolated porphyrin arrays.* Chemical Physics Letters, 2005. **412**(4): p. 303-306.

29. Cho, W.J., et al., *Chromium Porphyrin Arrays As Spintronic Devices.* Journal of the American Chemical Society, 2011. **133**(24): p. 9364-9369.

30. Hamad, S., et al., *Electronic structure of porphyrin-based metal–organic frameworks and their suitability for solar fuel production photocatalysis.* Journal of Materials Chemistry A, 2015. **3**(46): p. 23458-23465.

31. McDermott, G., et al., *Crystal structure of an integral membrane light-harvesting complex from photosynthetic bacteria.* Nature, 1995. **374**: p. 517.

32. Milgrom, L.R., *The Colours of Life.* 1997, Oxford: OUP.

33. Dolphin, D., *The Porphyrins.* 1978, New York: Academic Press. 664.

34. Giovannetti, R., *The use of spectrophotometry UV–vis for the study of porphyrins.* InTechOpen, 2012. **Macro To Nano Spectroscopy**.

35. Gouterman, M., *Study of the Effects of Substitution on the Absorption Spectra of Porphin.* The Journal of Chemical Physics, 1959. **30**(5): p. 1139-1161.

36. Gouterman, M., *Spectra of porphyrins.* Journal of Molecular Spectroscopy, 1961. **6**: p. 138-163.

37. Pham, V.D., et al., *Molecular adsorbates as probes of the local properties of doped graphene.* Scientific Reports, 2016. **6**: p. 24796.

38. Lightcap, I.V. and P.V. Kamat, *Graphitic Design: Prospects of Graphene-Based Nanocomposites for Solar Energy Conversion, Storage, and Sensing.* Accounts of Chemical Research, 2013. **46**(10): p. 2235-2243.

39. Liu, Z., S.P. Lau, and F. Yan, *Functionalized graphene and other two-dimensional materials for photovoltaic devices: device design and processing.* Chemical Society Reviews, 2015. **44**(15): p. 5638-5679.

40. Loh, K.P., S.W. Tong, and J. Wu, *Graphene and Graphene-like Molecules: Prospects in Solar Cells.* Journal of the American Chemical Society, 2016. **138**(4): p. 1095-1102.

41. Lu, Q., et al., *2D Transition-Metal-Dichalcogenide-Nanosheet-Based Composites for Photocatalytic and Electrocatalytic Hydrogen Evolution Reactions.* Advanced Materials, 2015. **28**(10): p. 1917-1933.

42. Yang, M.-Q., et al., *Artificial photosynthesis over graphene–semiconductor composites. Are we getting better?* Chemical Society Reviews, 2014. **43**(24): p. 8240-8254.

43. Umeyama, T., et al., *Remarkable Dependence of Exciplex Decay Rate on Through-Space Separation Distance between Porphyrin and Chemically Converted Graphene.* The Journal of Physical Chemistry C, 2016. **120**(49): p. 28337-28344.

44. Zeng, J. and K.-Q. Chen, *A nearly perfect spin filter and a spin logic gate based on a porphyrin/graphene hybrid material.* Physical Chemistry Chemical Physics, 2018. **20**(6): p. 3997-4004.

45. Wojcik, A. and P.V. Kamat, *Reduced Graphene Oxide and Porphyrin. An Interactive Affair in 2-D.* ACS Nano, 2010. **4**(11): p. 6697-6706.

46. Bala Murali Krishna, M., et al., *Synthesis and structural, spectroscopic and nonlinear optical measurements of graphene oxide and its composites with metal and metal free porphyrins.* Journal of Materials Chemistry, 2012. **22**(7): p. 3059-3068.

47. Geng, J., et al., *Preparation of graphene relying on porphyrin exfoliation of graphite.* Chemical Communications, 2010. **46**(28): p. 5091-5093.

48. Ussia, M., et al., *Freestanding photocatalytic materials based on 3D graphene and polyporphyrins.* Scientific Reports, 2018. **8**(1): p. 5001.

49. La, D.D., et al., *Fabrication of a Graphene@TiO2@Porphyrin Hybrid Material and Its Photocatalytic Properties under Simulated Sunlight Irradiation.* ChemistrySelect, 2017. **2**(11): p. 3329-3333.

50. Hayashi, H., et al., *Electron Transfer Cascade by Organic/Inorganic Ternary Composites of Porphyrin, Zinc Oxide Nanoparticles, and Reduced Graphene Oxide on a Tin Oxide Electrode that Exhibits Efficient Photocurrent Generation.* Journal of the American Chemical Society, 2011. **133**(20): p. 7684-7687.

51. Kiessling, D., et al., *Novel nanographene/porphyrin hybrids – preparation, characterization, and application in solar energy conversion schemes.* Chemical Science, 2013. **4**(8): p. 3085-3098.

52. Bhandary, S., O. Eriksson, and B. Sanyal, *Defect controlled magnetism in FeP/graphene/Ni(111).* Scientific Reports, 2013. **3**: p. 3405.

2 Methodology

2.1 Computational materials science

Computational chemistry is the use of computer simulations to investigate the behaviour of chemical systems at the molecular level. It has become a viable and indispensable tool for the analysis of properties of materials, thanks to the development of massively parallel computing. Computational materials science complements experimental techniques in different ways. For example, it is possible to computationally study unstable compounds which are problematic or dangerous to investigate experimentally. Calculations are becoming easier to perform and less costly, while experiments are often still expensive. That means that it has become practical to use calculations to screen the properties of a large family of compounds, to find out the most promising candidates for a particular application, which are then investigated experimentally.

The basic task of computational chemistry is to describe the properties of a collection of atoms (*i.e.* nuclei and electrons). One of the fundamental features to know about these atoms is their energy, and specifically, to understand the changes of this energy in function of the atomic positions. The graphical representation of the energy of the atoms considering their spatial arrangement is called potential energy surface (PES) [1]. The PES can be obtained either by solving the Schrödinger equation for the nuclei and electrons, or as a sum of classical interatomic potentials whose parameters are fitted to experiment or high-level calculations. In this Chapter, I will summarise the methods used to solve the Schrödinger equation for materials, and the approximations used in this thesis.

2.2 Quantum chemistry methods

In quantum mechanics, the wavefunction contains all the information about a quantum system, such as the electronic structure of atoms, molecules and solids [2, 3]. In a non-relativistic treatment, the wavefunction is calculated from the time-independent Schrödinger equation which, for a single electron in an external potential $v(r)$ would be [3, 4]:

$$\left[-\frac{\hbar^2\nabla^2}{2m}+v(r)\right]\Psi(r)=E\Psi(r) \tag{2.1}$$

Considering the case for more than a single electron, the Schrödinger equation (Eq. 2.1) turns into:

$$\left[\sum_{i}^{N}\left(-\frac{\hbar^2\nabla^2}{2m}+v(r_i)\right)+\sum_{i<j}U(r_i,r_j)\right]\Psi(r_1,r_2,\dots,r_N)=E\Psi(r_1,r_2,\dots,r_N) \tag{2.2}$$

where N is the number of electrons, the first sum is the sum of single-electron Hamiltonians and $U(r_i,r_j)$ is the electron-electron interaction. This formulation does not take into consideration the nuclear motion, because the so-called Born-Oppenheimer approximation is applied. This approximation is based on the decoupling of the electronic and nuclear motions, which is carried out considering that the mass of the nucleus is much greater than the mass of the electrons and therefore its speed is negligible in comparison to the speed of electrons. In this way, for the nuclei, the electrons are just a negative charge medium, and for the electrons the nuclei are static. As consequence, the electrons adapt instantaneously to any change of position of the nuclei [5, 6].

The repulsive Coulombic electron-potential follows the expression:

$$\widehat{U}=\sum_{i<j}U(r_i,r_j)=\sum_{i<j}\frac{e^2}{|r_i-r_j|} \tag{2.3}$$

where *e* is the elementary charge. $\widehat{U}$ is the same operator for any system having Coulomb interactions, just as the kinetic energy operator is the same for any group of electrons:

$$\hat{T} = -\frac{\hbar^2\nabla^2}{2m}\sum_i \nabla_i^2 \tag{2.4}$$

The external potential, however, is system dependent. In the case of a single atom, it can be written as:

$$v(r_i) = -\frac{Qe}{|r_i - R|} \tag{2.5}$$

where *Q* is the nuclear charge and *R* is the position of the nucleus. In a monoatomic system, *R* is usually the origin of the coordinate system. For the case of a molecule or a solid:

$$v(r_i) = -\sum_k \frac{Q_k e}{|r_i - R_k|} \tag{2.6}$$

where the sum over *k* is over all the nuclei of the system, each with charge $Q_k = Z_k e$ and position R_k.

Any given system is defined by the potential $v(r)$, from which, using the Schrödinger equation, it is possible to find the equation of the wavefunction Ψ. Finally any observables can be calculated using expected values of the operators of this wavefunction [7]:

$$v(r) \xrightarrow{\text{Schrödinger Eq.}} \Psi(r_1, r_2, \dots, r_N) \xrightarrow{\langle\Psi|\dots|\Psi\rangle} \text{observables} \tag{2.7}$$

However, it is still not an easy job to solve the Schrödinger equation due to the electron-electron interaction. The Hartree approximation reduces the many-body equation to a one-electron equation, by representing Ψ as a product of one-electron wavefunctions:

$$\Psi = \Psi(r_1, r_2, \dots, r_N) = \Psi_1(r_1)\Psi_2(r_2)\cdots\Psi_N(r_N) \tag{2.8}$$

Unfortunately, the Hartree method does not take the exchange interaction into consideration. Adding Fermi statistics to Hartree method develops the Hartree-Fock approximation. The procedure to derive the ground state electron wavefunction is the usage of a trial wavefunction to solve the equation until the convergence is reached (self-consistent field method - SCF). The final field computed from the charge distribution should be self-consistent with the assumed initial field.

2.2.1 Hartree-Fock Approximation

Within the Hartree method, the electronic spin does not appear explicitly except for the fact that no more than two electrons may go into a single orbital. The existence of the Pauli exclusion principle, however, needs to be accounted for in order to go beyond the Hartree method, and that is what the Hartree-Fock method is all about [8, 9].

Considering an arbitrary three-dimensional orbital $\boldsymbol{\phi}$ for electron *i* by writing it as the product of a purely space-dependent part ξ and a spin function (α or β) characterising spin-up or spin-down electron, for example $\boldsymbol{\phi_i(x_i) = \xi_i(r_i)\alpha_i}$ where $\boldsymbol{x}$ is a variable that includes both space ($\boldsymbol{r}$) and spin (α). A Hartree-like product wavefunction between two one-electron wavefunctions $\boldsymbol{\phi_1}$ and $\boldsymbol{\phi_2}$ can be written as $\Psi' = \xi_1(\boldsymbol{r_1})\alpha_1\xi_2(\boldsymbol{r_2})\beta_2$ but also as $\Psi'' = \xi_1(\boldsymbol{r_2})\alpha_2\xi_2(\boldsymbol{r_1})\beta_1$, since both are equally suitable.

Due to any fermionic wavefunction must be antisymmetric with respect to an exchange of electrons, the wavefunction is:

$$\Psi = \Psi' - \Psi'' = \xi_1(\boldsymbol{r_1})\alpha_1\xi_2(\boldsymbol{r_2})\beta_2 - \xi_1(\boldsymbol{r_2})\alpha_2\xi_2(\boldsymbol{r_1})\beta_1 = \begin{vmatrix} \xi_1(\boldsymbol{r_1})\alpha_1 & \xi_2(\boldsymbol{r_1})\beta_1 \\ \xi_1(\boldsymbol{r_2})\alpha_2 & \xi_2(\boldsymbol{r_2})\beta_2 \end{vmatrix} \quad (2.9)$$

which is called a Slater determinant [10] and is an antisymmetrised product wavefunction. Switching back to the $\boldsymbol{\phi}$ notation, we have the following expression for a total of *N* electrons:

$$\Psi(\boldsymbol{x}_1, \boldsymbol{x}_2, \ldots, \boldsymbol{x}_N) = \frac{1}{\sqrt{N!}} \begin{vmatrix} \phi_1(\boldsymbol{x}_1) & \phi_2(\boldsymbol{x}_1) & \cdots \\ \phi_1(\boldsymbol{x}_2) & \phi_2(\boldsymbol{x}_2) & \cdots \\ \vdots & \vdots & \end{vmatrix} \tag{2.10}$$

The mathematical feature of the determinant in Eq. 2.10 allows for the compact formulation of the Hartree-Fock equations. The iterative, self-consistent solution of the Hartree-Fock equations proceeds in quite a similar way to the Hartree case, except that they are mathematically more demanding. This is because the antisymmetrisation leads to a nonlocal (dependent on two variables) exchange potential.

Comparing the energy obtained using this method with the exact energy from the many-body Schrödinger equation, there is deviation that is called correlation energy, which, in conjunction with the exchange energy (the energy difference for exchanging electrons in solving the Hartree-Fock equations), is proved to be quite difficult to calculate for a complex system. To access the correlation contributions, it is possible to perform post-Hartree-Fock calculations, where more than one determinant is used to expand the wavefunction (using unoccupied orbitals in the determinants). These methods are generally too expensive to use in computational materials science. In this thesis, in order to introduce correlation effects, which are crucial to obtain accurate electronic structures and to describe van der Waals interactions, I employ density functional theory (DFT).

2.3 Density functional theory (DFT)

2.3.1 Hohenberg-Kohn theorems

The central elements of DFT are the Hohenberg-Kohn theorems and the Kohn-Sham equations [11]. DFT can be considered as a good and versatile option to solve the Schrödinger equation, since this method overcomes the deficiencies of the approximation methods previously mentioned and also systematically simplify the problem of multiple bodies to a problem of a single body. To do this, DFT focuses on the electron density

$\rho(r)$, instead of the wavefunction, as the basis of the calculation for all observables associated with a system. This density for a *N* electron system can be related to the wavefunction by the equation:

$$\rho(r) = N \int \mathrm{d}^3 r_2 \int \mathrm{d}^3 r_3 \dots \int \mathrm{d}^3 r_N \Psi^*(r_1, r_2, \dots, r_N)\Psi(r_1, r_2, \dots, r_N) \qquad (2.11)$$

The fundamental approximation on which DFT is based can be summarised in the following scheme:

$$\rho(r) \Longrightarrow \Psi(r_1, r_2, \dots, r_N) \Longrightarrow \nu(r) \qquad (2.12)$$

Knowing the electron density $\rho(r)$ implies the knowledge of the wavefunction and the potential, and with it all observables. The previous statement corresponds to one of Hohenberg and Kohn existence theorems where it said that when the obtained ρ is the density of the fundamental state associated with the potential $\nu(r)$, the minimum of the density functional can be obtained.

The energy of a system is a functional of the wavefunction having the following expression:

$$E = E[\Psi] = \int \Psi(r_1, r_2, \dots, r_N)\, \widehat{H}\Psi^*(r_1, r_2, \dots, r_N) dr_1 dr_2 \dots dr_N \qquad (2.13)$$

where its domain is in the Hilbert space. The minimisation of the functional $E[\Psi]$ over the entire Hilbert space allows us to obtain the energy of the ground-state E_0 and its wavefunction Ψ_0. It is important to have in mind that $E_0 = E[\Psi_0] \leq E[\Psi]$ [5]. Then, the density functional is the ratio of the energy of the system and the spatial function corresponding to the electron density and it produces a number.

The proofs performed by Hohenberg and Kohn elucidate two very simple existence theorems on which the whole DFT is based [12]:

1) For degenerated ground-states, two distinct Hamiltonians cannot have the same electron density of the basal state, for this reason we can define the energy of basal state as a density functional $\rho(r): E = E[\rho]$.
2) The energy $E[\rho]$ is the lowest when $\rho(r)$ is the density of the basal state.

It should be emphasised that the first theorem of Hohenberg and Kohn forbids two different systems having the same density, but does not guarantee that, given a density ρ there exist at least one system with that density. On the other hand, regarding the second theorem, it is important to mentioned that the minimum of the functional can be obtained when ρ is the density of the fundamental state with the potential $v(r)$.

Those theorems themselves are proofs of existence and they are not proofs of construction. This is the reason why the development of these methods (where these proofs are applied) still to be based on the experience and on trial-and-error techniques.

2.3.2 Kohn-Sham method

Using the definitions explained above, the Hamiltonian can be expressed as follows:

$$H = \hat{T} + \hat{U} + \hat{V} \tag{2.14}$$

where $\hat{T}$ is the operator of the total kinetic energy of the system, $\hat{U}$ is the electron-electron interaction operator and $\hat{V}$ is the external potential operator.

The scheme to treat this problem is based on decomposing the kinetic energy $\hat{T}[\rho]$ into two components: one that represents the kinetic energy of the non-interacting particles of density $\hat{T}_s[\rho]$ and another one $\hat{T}_c[\rho]$ that represents the remainder of the total kinetic energy, *i.e.* $\hat{T}[\rho] = \hat{T}_s[\rho] + \hat{T}_c[\rho]$. The subscripts *s* and *c* refer to a single particle and to correlation, respectively.

The term $\hat{T}_s[\rho]$ depends on the density ρ and is not known exactly, but it is easily expressed in terms of the single-particle orbitals $\boldsymbol{\phi_i(r)}$ of a non-interacting system with density ρ, as Eq. 2.15.

$$T_s[\rho] = -\frac{\hbar^2}{2m}\sum_i^N \int \mathrm{d}^3 r \phi_i^*(\boldsymbol{r})\nabla^2\phi_i(\boldsymbol{r}) \tag{2.15}$$

We now can rewrite the energy functional as follows:

$$E[\rho] = T[\rho] + U[\rho] + V[\rho] \tag{2.16}$$

$$E[\rho] = T_s[\{\phi_i[\rho]\}] + U_H[\rho] + V[\rho] + E_{xc}[\rho] \tag{2.17}$$

where, by definition [13], $E_{xc}[\rho]$ contains the differences $T[\rho]-T_s[\rho]$ which is the term of correlation $T_c[\rho]$, and $U[\rho] - U_H[\rho]$, where $U_H[\rho] = \frac{1}{2}\int \frac{\rho(\boldsymbol{r})\rho(\boldsymbol{r'})}{|\boldsymbol{r}-\boldsymbol{r'}|}\boldsymbol{dr}\boldsymbol{dr'}$. Equation 2.17 is formally exact but E_{xc} is unknown, although the Hohenberg-Kohn theorem guarantees that it is a density functional. This functional $E_{xc}[\rho]$ is called the exchange-correlation energy and it is often decomposed as:

$$E_{xc} = E_x + E_c \tag{2.18}$$

where E_c is an effect caused by the presence of the other electrons (T_c is then a part of E_c) and E_x is due to the Pauli principle (exchange energy). The exchange energy can be written explicitly in terms of the single-particle orbitals as:

$$E_x[\{\phi_i[\rho]\}] = -\frac{q^2}{2}\sum\nolimits_{jk}\int \mathrm{d}^3 r \int \mathrm{d}^3 r' \frac{\phi_j^*(\boldsymbol{r})\phi_k^*(\boldsymbol{r'})\phi_j(\boldsymbol{r})\phi_k(\boldsymbol{r'})}{|\boldsymbol{r}-\boldsymbol{r'}|} \tag{2.19}$$

Some observations can be made on the exchange-correlation functional:

- The definition of $E_{xc}[\rho]$ involves two systems: an interacting system for the calculation of $U[\rho]$ and a non-interacting system for the calculation of $T_s[\rho]$ (both systems have the same density).
- Since the functional $U[\rho]$ is unknown, $E_{xc}[\rho]$ is also unknown and that is the reason why approximations must be used.

- If the explicit form of $E_{xc}[\rho]$ is already known, energy and density of any interacting system can be obtained by minimising the functional.

The most popular approximation used for the exchange-correlation functional calculations are the local density approximation (LDA) and the generalised gradient approximation (GGA).

In LDA, $E_{xc}[\rho]$ is approximated by the exchange-correlation energy of an electron in a homogeneous electron gas of the same density. Despite this simple supposition, LDA gives good results for the systems with slowly changing charge densities. However, an underestimation in some properties, such as lattice parameters, is associated with this approximation. In addition, LDA does not show a successful performance for van der Waals (vdW) interactions and it would also give wrong predictions for some strongly correlated magnetic systems.

The GGA is the best-known class of functional after LDA. In this approximation, the exchange-correlation functional is considered as the functional of the electron density and the gradient of the electron density. There are many ways in which this information could build the gradient of the electron density, so there are a huge number of distinct GGA functionals. Two of the most widely used functionals are the Perdew-Wang functional (PW91) [14, 15] and the Perdew-Burke-Ernzerhof functional (PBE) [16, 17]. For GGA functional is well-known the overestimation of lattice parameters and cannot solve situations concerning the strong correlated systems and the vdW interactions properly, neither. Moreover, finding an accurate and universally-applicable $E_{xc}[\rho]$ remains a significant challenge in DFT.

2.4 Limitations of local DFT approaches

It is important to point out that different functionals will give somewhat different results for any particular configuration of atoms. Hence it is necessary to specify what functional was used in any particular calculation rather than simply referring to a DFT calculation.

Nevertheless, there are some important situations for which DFT cannot be expected to be physically accurate. DFT calculations have limited accuracy in the calculation of electronic excited states. This can be understood in a general way by remembering that the Hohenberg-Kohn theorems only apply to the ground-state energy.

A well-known inaccuracy in DFT is the underestimation of calculated band gaps in semiconducting and insulating materials. Standard DFT calculations, with existing functionals, have limited accuracy for band gaps with errors larger than 1 eV which cannot be ignored.

Other situations where DFT calculations give inaccurate results are associated with the weak vdW interactions that exist between atoms and molecules. The vdW interactions in DFT are a direct result of long-range electron correlation for which the exchange-correlation functional is unknown or not adequately described by the existing approximations. Some techniques have been developed in order to go beyond the aforementioned DFT limits. However, these methods are available and under development for specific or particular systems of interest. The most popular post-DFT methods will be described to facilitate the comprehension using already known cases where DFT has been already improved.

2.5 Correcting the local character of the exchange functional

2.5.1 LDA(GGA)+U

Some insulating transition-metal oxides are falsely predicted as being metals when their electronic structures are calculated on the basis of the LDA or the GGA, because the full amount of the local Coulomb repulsion experienced by the electrons within the *d* orbitals is underestimated, and the inclusion of some extra repulsion *U* is needed to theoretically change them into insulators. This is how the LDA+U (or GGA+U) method is typically justified [18]. The method works well for transition-metal oxides and may also be used for some challenging metals, in particular the *f* elements.

The calculation of *U* requires additional approximations (the so-called constrained LDA method may deal with the problem [19]), but most often *U* is used as a fitting parameter to reproduce a property of interest, for example the band gap or the magnetic coupling in the solid [20].

2.5.2 Hybrid density functionals

DFT provides a rigorous framework for simple models of the many-body effects that dominate the computational cost of wavefunction-based electronic structure calculations [21]. Simple semilocal density functionals (LDA or GGA) can accurately model many ground state properties including lattice parameters [22].

Unfortunately, semilocal density functionals tend to over-delocalise electrons due to their intrinsic self-interaction error* [23]. This makes them problematic for localised

* Self-interaction error refers to the fact that semilocal exchange-correlation functionals allow electrons to interact with themselves.

subsystems such as defects, surface states, and *d* and *f* block elements. They also systematically underestimate band gaps, often mistakenly assigning metallic behaviour to semiconductors [24, 25].

In order to solve this kind of problems, hybrid density functional must be used which incorporate a fraction of exact nonlocal (Hartree-Fock type) exchange. Some hybrid functionals (like PBE0 [26] or B3LYP [27-30]) incorporate a fraction of Hartree-Fock potential at all ranges. Other functionals, the so-called screened hybrid functionals (like HSE [31, 32]), only incorporate Hartree-Fock exchange contributions in the short range. Screened hybrid functionals do not use long-range Hartree-Fock exchange to avoid some undesirable effects, for example exchange interactions at large distances are exactly cancelled by correlation in the uniform electron gas [33], and approximately cancelled by correlation in metals and narrow band gap semiconductors [34-36].

2.5.3 Screened hybrid functionals: the Heyd-Scuseria-Ernzerhof functional (HSE)

The screened hybrid functional of Heyd, Scuseria and Ernzerhof (HSE) [31, 32] was proposed to extend the successes of hybrid functionals into the solid state, by avoiding the problematic effects of long-range Hartree-Fock exchange.

This functional is based on the PBE0 global hybrid [26, 37] of the PBE GGA. PBE0 incorporates 25% full-range Hartree-Fock exchange, 75% full-range PBE exchange and 100% PBE correlation. The fraction of Hartree-Fock is based on perturbation theory arguments [38]. HSE, on the other hand, includes 25% short-range Hartree-Fock exchange and no long-range Hartree-Fock exchange† [39]. HSE is related to the screened hybrid

† A range-separation parameter in this functional is selected empirically and it is set to 0.11 $Bohr^{-1}$ in the latest version of the functional HSE06.

functionals of Bylander and Kleinman [24] and Seidl *et al.* [40] and also to screened Coulomb operator methods previously developed in quantum chemistry [41-43].

One of HSE's most important aspects is its ability to accurately predict semiconductor band gaps. Unlike LDA or GGA functionals, HSE include an approximate derivative discontinuity [44]. This can be incorporated using the generalised Kohn-Sham approach (GKS). GKS treatments of hybrid functionals replace the non-interacting Kohn-Sham reference system with a system containing some part of the electron-electron interaction [40, 45]. (For example, the HSE reference system contains 25% of the short-range interaction). This interaction provides a nonlocal contribution to the exchange-correlation potential, similar to the nonlocal exchange present in Hartree-Fock theory. The resulting GKS band energy differences incorporate the functional's approximate derivative discontinuity.

In this thesis, we use the hybrid density functional HSE whenever accurate band gaps are required, for example, in the examination of the band structure of porphyrin nanostructures in **Chapter 6** and of porphyrin-based MOFs in **Chapter 7**. In the latter case, for example, use of the GGA+U leads to a band gap of 1.02 eV for the Cu-Zn-TCPP, but with HSE the obtained band gap was 2.20 eV. The GGA+U still provides a sensible electronic structure in all cases, so we use this method to optimise the geometries and obtain initial wavefunctions before a final HSE single-point calculation. In the chapters where only carbon nanostructures are considered, HSE is generally not necessary since graphene does not have a band gap. However, nonlocal exchange is sometimes necessary in the calculation of graphitic nanostructures. For example, DFT calculations predict zigzag nanoribbons to be spin-polarised, with up-spin polarisation on one side of the ribbon and down-spin on the other. These have been proposed as "half-metallic" systems that could preferentially conduct one spin flavour under the influence of electric fields [46] or asymmetric edge substitution [47]. Recent HSE calculations on armchair nanoribbons

predict width-dependent band gap oscillations similar to those found in tight-binding calculations [48, 49]. The HSE predictions were later confirmed experimentally [50, 51]. A detailed study of edge substitution suggested that edge oxidation could enhance the half-metallic behaviour of zigzag graphene nanoribbons, lowering the applied field needed to induce half-metallicity [52]. A particularly interesting set of recent studies suggests that the spin polarisation predicted for nanoribbons may also occur in finite graphene nanoparticles [53, 54].

The screened exchange approximation appears to be a very powerful tool for density functional treatments of condensed systems. The HSE screened hybrid provides a reasonably accurate and computationally tractable treatment of ground-state properties and band energies, while incorporating only a single, universal empirical parameter [23].

2.6 Correcting the local character of the correlation functional: dispersion interactions

2.6.1 The dispersion force problem in local DFT approximations

DFT is widely applied with approximate local and semilocal density functional for the description of bulk and surface properties of solids. However, sparse systems, including soft matter, vdW complexes, and biomolecules, are at least as abundant. They have interparticle separations, for which nonlocal, long-ranged interactions (such as vdW forces) are important [55] and these are not well described by the local and semi-local approximations in DFT.

Proper inclusion of vdW interactions in DFT calculations requires that the total energy functional depends on the electron density $\rho(r)$ in a manner that reflects both the long-ranged and medium-ranged nature of vdW interactions [56]. By construction, LDA and GGA neglect the long-range, nonlocal correlations that give rise to the vdW forces.

One solution to this problem is to incorporate empirical potentials known as dispersion-corrected DFT [57, 58]. Another solution is a first-principles DFT treatment of the long-to-medium-ranged forces between fragments across regions with low densities which is the Rutgers-Chalmers vdW-DF method [55].

2.6.2 Empirical dispersion corrections

These approximations are also known as Grimme's dispersion correction methods. In these methods, the empirical dispersion potential has the form $-C_6/R^6$ at long distances, and a damping function is applied at short distances, to scale down contributions from the empirical term within typical bonding distances, at which the local DFT approach performs correctly. The oldest of these approaches is DFT-D2 [59], where the C_6 coefficients are pairwise atomic parameters:

$$E_{\text{disp}}^{\text{D2}} = -\sum_{A}^{\text{atoms}} \sum_{B<A}^{\text{atoms}} \left(\frac{C_{6,AB}}{R_{AB}^6}\right) f_{\text{damp},6}(R_{AB}) \tag{2.20}$$

This damping function in this case is:

$$f_{\text{damp},6}(R_{AB}) = \frac{s_6}{1 + e^{-d\left(\frac{R_{AB}}{R_{0,AB}} - 1\right)}} \tag{2.21}$$

where the parameters are empirically fitted for each functional and atom pair. The quantity $R_{0,AB}$ is the sum of the vdW radii for atoms *A* and *B*. The most important parameter in Eq. (2.20) the inter-atomic coefficient C_6, which can be obtained as geometric means of atom-centred parameters, as in classical force fields.

The DFT-D3 method [60] is an improvement on D2 approach, which considers a similar potential as D2 but including atomic C_8 terms as well:

$$E_{\text{disp}}^{\text{D3}} = -\sum_{A}^{\text{atoms}} \sum_{B<A}^{\text{atoms}} \left[\left(\frac{C_{6,AB}}{R_{AB}^6}\right) f_{\text{damp},6}(R_{AB}) + \left(\frac{C_{8,AB}}{R_{AB}^8}\right) f_{\text{damp},6}(R_{AB})\right] \tag{2.22}$$

Grimme's formulation, which is known as the 'zero-damping' version, uses damping functions of the form:

$$f_{\text{damp},n}(R_{AB}) = \frac{s_n}{1 + 6\left(\frac{R_{AB}}{s_{r,n}R_{0,AB}}\right)^{-\alpha_n}}$$

for n = 6 or 8, α_6 = 14, α_8 = 16 and $s_{r,8}$ = s_6 = 1. The parameters s_8 and $s_{r,6}$ are adjustable whose values depend on the choice of exchange-correlation functional and $R_{0,AB}$ comes from atomic vdW radii. An important difference with respect to the D2 method is that in D3, the dispersion coefficients C_n are geometry-dependent as they are adjusted on the basis of the coordination numbers around the atoms participating in the interaction.

2.6.3 Non-local correlation functional

This method (abbreviated here as vdW-DF) includes vdW forces using a nonlocal exchange-correlation functional. The objective of these methods is to provide, within DFT, a non-empirical but still efficient method for calculating vdW effects. In this regard, the vdW-DF method differs from methods that use empirical, semi-empirical, and ad hoc assumptions for such calculations.

Dispersion interactions emanate from nonlocal electron correlations. This is illustrated in early dipole-model descriptions of the interactions in noble-gas crystals [61]. The electrodynamical coupling between the atomic dipoles gives a shift in the dipolar oscillator frequencies, and the sum of all these shifts gives the vdW binding energy [61].

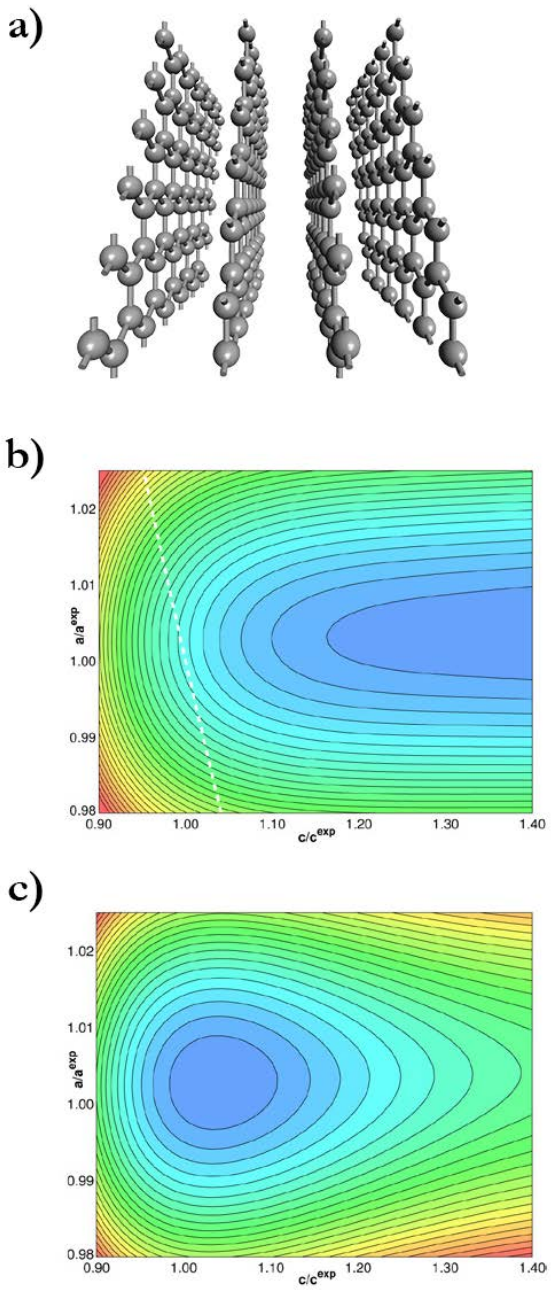

Figure 2.1. a) Atomic configuration of graphene sheets with large intersheet separations ($c_{exp} \approx 3.35$ Å), where a low electron density exists into intersheet regions (the nonlocal correlation acts across these regions). Variation of the interlayer interaction energy of b) GGA (PW91) [14, 15] and c) layered geometry vdW-DF [62, 63], both plotted as functions of in-plane lattice constant a and interlayer separation c, relative to the experimental values (a_{exp} and c_{exp}). (Figures b) and c) obtained from Refs. [56, 62, 63])

The major features of the vdW bond in a prototype DFT application can be illustrated with graphite. **Figure 2.1**, taken from Berland *et al.* and Rydberg *et al.* [56, 62, 63], shows the atomic configuration with dense and sparse regions (**Figure 2.1a**),

binding-energy contours [63] obtained with traditional DFT-GGA (**Figure 2.1b**), and with the vdW-DF method (**Figure 2.1c**) as functions of both the in-plane (intra-sheet) lattice constant a and inter-sheet separation c divided by their experimental reference values (a_{exp} and c_{exp}, respectively). The white dashed-line in **Figure 2.1b** identifies (a, c) values that are consistent with the experimentally observed unit cell volume.

In the GGA description, interlayer binding is absent except at an unphysically large separation and with negligible binding energy. The vdW-DF results reflect a solution to a long-standing challenge in traditional DFT: the state-of-the-art DFT, which was GGA at the time, should not rule out the existence of the most stable carbon allotrope, *i.e.* graphite.

With the development of vdW-DF functional, the binding energy obtained for this graphitic system is 10.3 meV $Å^{-2}$ [64], which corresponds to 43 meV per atom [63] in reasonable agreement with the experimental reference at the time of ~-33 meV/atom [65, 66]. In contrast, LDA calculations yielded 20 meV [67-71] and GGA calculations barely gave binding. The simple fact that vdW-DF has a binding energy with the correct sign and a reasonable magnitude spurred much enthusiasm among the developers in the field and this optimism was communicated by the title of the article '*Hard numbers for soft matter*' [63].

2.7 VASP software package

VASP (Vienna *ab initio* simulation package) is a first-principles calculation code within DFT frame, which uses ultrasoft pseudopotentials or the projector-augmented wave (PAW) method and a plane wave basis set. The approach implemented in this code is based on the LDA with the free energy as variational quantity and an exact evaluation of the instantaneous electronic ground-state at each molecular dynamics time step. It also uses efficient matrix diagonalization schemes and an efficient Pulay/Broyden charge density mixing. Thus, it can give information about total energies, forces and stresses on an atomic

system, as well as calculating optimum geometries, band structures, optical spectra, among others.

In this study, VASP is going to be useful for electronic properties calculations of porphyrin- and carbon-based systems. For geometry optimisation of porphyrin-based structures, the exchange and correlation potential will be treated within the GGA using the dispersion-corrected PBE functional [16, 17], while for accurate electronic band structures the screened hybrid HSE functional will be used [31, 32] since the GGA-PBE method is known to underestimate the band gap [72]. Since dispersion effects commonly exist within these kind of systems, which cannot be ignored, vdW corrections (*i.e.* Grimme's corrections [57-60] explained in **Chapter 2.6.2**) should be considered when relaxing the structures by setting relative parameters in VASP. The inclusion of these effects will make the calculated electronic properties more reliable and closer to real situations.

For the case of carbon-based structures, it is well established that the GGA is inadequate for the description of long-range dispersion interactions [56], which play an important role in graphitic structures. Although the LDA of DFT does lead to interlayer binding and is sometimes used to investigate graphitic and other layered structures, this approximation is also unable to provide an adequate description of long-range dispersion interactions [73]. Therefore, the functional employed here needs to take into account the nonlocal correlation: optPBE-vdW [74, 75]. This functional has been successfully used in modelling graphite and other layered materials [76-79]. In contrast with functionals with an empirical correction added to describe dispersion, like those proposed by Grimme *et al.* [59, 60], nonlocal correlation functionals allow for the charge density to respond to the dispersion interactions, providing a more robust description of interlayer interactions.

2.8 References

1. Jensen, F., *Introduction to computational chemistry*. 2nd Edition ed. 2007, Chichester: John Wiley & Sons, Ltd.
2. Pauling, L., Wilson, E. B., *Introduction to Quantum Mechanics with Applications to Chemistry*. 1935, New York: McGraw-Hill.
3. Eisberg, R., Resnick, R., *Quantum physics of atoms, molecules, solids, nuclei, and particles*. 1985, New York: Wiley.
4. Tijonov, A.N., Samarsky, A. A., *Equations of Mathematical Physics*. 1983, 3rd Edition. MIR Editorial.
5. Maroto, E., *Cálculos computacionales de estructuras moleculares*. 2012, Alicante.
6. Fraga, S., *Química teórica: estructura, interacciones y reactividad*. 1987, Consejo Superior de Investigaciones Científicas.
7. Koch, W., Holthausen, M. C., *A Chemist's Guide to Density Functional Theory*. 2nd ed. 2001, Germany: Wiley-VCH Verlag GmbH.
8. Fock, V., *Näherungsmethode zur Lösung des quantenmechanischen Mehrkörperproblems*. Zeitschrift für Physik, 1930. **61**(1): p. 126-148.
9. Fock, V., *„Selfconsistent field" mit Austausch für Natrium*. Zeitschrift für Physik, 1930. **62**(11): p. 795-805.
10. Slater, J.C., *Note on Hartree's Method*. Physical Review, 1930. **35**(2): p. 210-211.
11. Capelle, K., *A bird's-eye view of density-functional theory*. Brazilian Journal of Physics, 2006. **36**: p. 1318-1343.
12. Hohenberg, P. and W. Kohn, *Inhomogeneous Electron Gas*. Physical Review, 1964. **136**(3B): p. B864-B871.
13. Kohn, W. and L.J. Sham, *Self-Consistent Equations Including Exchange and Correlation Effects*. Physical Review, 1965. **140**(4A): p. A1133-A1138.

14. Perdew, J.P., et al., *Atoms, molecules, solids, and surfaces: Applications of the generalized gradient approximation for exchange and correlation.* Physical Review B, 1992. **46**(11): p. 6671-6687.

15. Perdew, J.P., et al., *Erratum: Atoms, molecules, solids, and surfaces: Applications of the generalized gradient approximation for exchange and correlation.* Physical Review B, 1993. **48**(7): p. 4978-4978.

16. Perdew, J.P., K. Burke, and M. Ernzerhof, *Generalized Gradient Approximation Made Simple.* Physical Review Letters, 1996. **77**(18): p. 3865-3868.

17. Perdew, J.P., K. Burke, and M. Ernzerhof, *Generalized Gradient Approximation Made Simple [Phys. Rev. Lett. 77, 3865 (1996)].* Physical Review Letters, 1997. **78**(7): p. 1396-1396.

18. Eschrig, H., K. Koepernik, and I. Chaplygin, *Density functional application to strongly correlated electron systems.* Journal of Solid State Chemistry, 2003. **176**(2): p. 482-495.

19. Gunnarsson, O., et al., *Density-functional calculation of the parameters in the Anderson model: Application to Mn in CdTe.* Physical Review B, 1989. **39**(3): p. 1708-1722.

20. Grau-Crespo, R., et al., *Electronic structure and magnetic coupling in $FeSbO_4$: A DFT study using hybrid functionals and GGA+U methods.* Physical Review B, 2006. **73**(3): p. 035116.

21. Kurth, S., J.P. Perdew, and P. Blaha, *Molecular and solid-state tests of density functional approximations: LSD, GGAs, and meta-GGAs.* International Journal of Quantum Chemistry, 1999. **75**(4 - 5): p. 889-909.

22. Fuchs, M., et al., *Pseudopotential study of binding properties of solids within generalized gradient approximations: The role of core-valence exchange correlation.* Physical Review B, 1998. **57**(4): p. 2134-2145.

23. Janesko, B.G., T.M. Henderson, and G.E. Scuseria, *Screened hybrid density functionals for solid-state chemistry and physics.* Physical Chemistry Chemical Physics, 2009. **11**(3): p. 443-454.

24. Bylander, D.M. and L. Kleinman, *Good semiconductor band gaps with a modified local-density approximation.* Physical Review B, 1990. **41**(11): p. 7868-7871.

25. Staroverov, V.N., et al., *Tests of a ladder of density functionals for bulk solids and surfaces.* Physical Review B, 2004. **69**(7): p. 075102.

26. Adamo, C. and V. Barone, *Toward reliable density functional methods without adjustable parameters: The PBE0 model.* The Journal of Chemical Physics, 1999. **110**(13): p. 6158-6170.

27. Becke, A.D., *Density - functional thermochemistry. III. The role of exact exchange.* The Journal of Chemical Physics, 1993. **98**(7): p. 5648-5652.

28. Lee, C., W. Yang, and R.G. Parr, *Development of the Colle-Salvetti correlation-energy formula into a functional of the electron density.* Physical Review B, 1988. **37**(2): p. 785-789.

29. Vosko, S.H., L. Wilk, and M. Nusair, *Accurate spin-dependent electron liquid correlation energies for local spin density calculations: a critical analysis.* Canadian Journal of Physics, 1980. **58**(8): p. 1200-1211.

30. Stephens, P.J., et al., *Ab Initio Calculation of Vibrational Absorption and Circular Dichroism Spectra Using Density Functional Force Fields.* The Journal of Physical Chemistry, 1994. **98**(45): p. 11623-11627.

31. Heyd, J., G.E. Scuseria, and M. Ernzerhof, *Hybrid functionals based on a screened Coulomb potential.* The Journal of Chemical Physics, 2003. **118**(18): p. 8207-8215.

32. Heyd, J., G.E. Scuseria, and M. Ernzerhof, *Erratum: "Hybrid functionals based on a screened Coulomb potential" [J. Chem. Phys. 118, 8207 (2003)].* The Journal of Chemical Physics, 2006. **124**(21): p. 219906.

33. Zecca, L., et al., *Local density functional for the short-range part of the electron-electron interaction.* Physical Review B, 2004. **70**(20): p. 205127.

34. Monkhorst, H.J., *Hartree-Fock density of states for extended systems.* Physical Review B, 1979. **20**(4): p. 1504-1513.

35. Delhalle, J. and J.-L. Calais, *Direct-space analysis of the Hartree-Fock energy bands and density of states for metallic extended systems.* Physical Review B, 1987. **35**(18): p. 9460-9466.

36. Gell-Mann, M. and K.A. Brueckner, *Correlation Energy of an Electron Gas at High Density.* Physical Review, 1957. **106**(2): p. 364-368.

37. Ernzerhof, M. and G.E. Scuseria, *Assessment of the Perdew–Burke–Ernzerhof exchange-correlation functional.* The Journal of Chemical Physics, 1999. **110**(11): p. 5029-5036.

38. Perdew, J.P., M. Ernzerhof, and K. Burke, *Rationale for mixing exact exchange with density functional approximations.* The Journal of Chemical Physics, 1996. **105**(22): p. 9982-9985.

39. Krukau, A.V., et al., *Influence of the exchange screening parameter on the performance of screened hybrid functionals.* The Journal of Chemical Physics, 2006. **125**(22): p. 224106.

40. Seidl, A., et al., *Generalized Kohn-Sham schemes and the band-gap problem.* Physical Review B, 1996. **53**(7): p. 3764-3774.

41. Gill, P.M.W. and R.D. Adamson, *A family of attenuated Coulomb operators.* Chemical Physics Letters, 1996. **261**(1): p. 105-110.

42. Adamson, R.D., J.P. Dombroski, and P.M.W. Gill, *Chemistry without Coulomb tails.* Chemical Physics Letters, 1996. **254**(5): p. 329-336.

43. Gill, P.M.W., R.D. Adamson, and J.A. Pople, *Coulomb-attenuated exchange energy density functionals.* Molecular Physics, 1996. **88**(4): p. 1005-1009.

44. Cohen, A.J., P. Mori-Sánchez, and W. Yang, *Fractional charge perspective on the band gap in density-functional theory.* Physical Review B, 2008. **77**(11): p. 115123.

45. Neumann, R., R.H. Nobes, and N.C. Handy, *Exchange functionals and potentials.* Molecular Physics, 1996. **87**(1): p. 1-36.

46. Son, Y.-W., M.L. Cohen, and S.G. Louie, *Half-metallic graphene nanoribbons.* Nature, 2006. **444**: p. 347.

47. Kan, E.-j., et al., *Half-Metallicity in Edge-Modified Zigzag Graphene Nanoribbons.* Journal of the American Chemical Society, 2008. **130**(13): p. 4224-4225.

48. Ezawa, M., *Peculiar width dependence of the electronic properties of carbon nanoribbons.* Physical Review B, 2006. **73**(4): p. 045432.

49. Barone, V., O. Hod, and G.E. Scuseria, *Electronic Structure and Stability of Semiconducting Graphene Nanoribbons.* Nano Letters, 2006. **6**(12): p. 2748-2754.

50. Han, M.Y., et al., *Energy Band-Gap Engineering of Graphene Nanoribbons.* Physical Review Letters, 2007. **98**(20): p. 206805.

51. Chen, Z., et al., *Graphene nano-ribbon electronics.* Physica E: Low-dimensional Systems and Nanostructures, 2007. **40**(2): p. 228-232.

52. Hod, O., et al., *Enhanced Half-Metallicity in Edge-Oxidized Zigzag Graphene Nanoribbons.* Nano Letters, 2007. **7**(8): p. 2295-2299.

53. Hod, O., J.E. Peralta, and G.E. Scuseria, *Edge effects in finite elongated graphene nanoribbons.* Physical Review B, 2007. **76**(23): p. 233401.

54. Hod, O., V. Barone, and G.E. Scuseria, *Half-metallic graphene nanodots: A comprehensive first-principles theoretical study.* Physical Review B, 2008. **77**(3): p. 035411.

55. Dion, M., et al., *Van der Waals Density Functional for General Geometries.* Physical Review Letters, 2004. **92**(24): p. 246401.

56. Berland, K., et al., *van der Waals forces in density functional theory: a review of the vdW-DF method.* Reports on Progress in Physics, 2015. **78**(6): p. 066501.

57. Grimme, S., *Density functional theory with London dispersion corrections.* WIREs Computational Molecular Science, 2011. **1**(2): p. 211-228.

58. Grimme, S., et al., *Dispersion-Corrected Mean-Field Electronic Structure Methods.* Chemical Reviews, 2016. **116**(9): p. 5105-5154.

59. Grimme, S., *Semiempirical GGA-type density functional constructed with a long-range dispersion correction.* Journal of Computational Chemistry, 2006. **27**(15): p. 1787-1799.

60. Grimme, S., et al., *A consistent and accurate ab initio parametrization of density functional dispersion correction (DFT-D) for the 94 elements H-Pu.* The Journal of Chemical Physics, 2010. **132**(15): p. 154104.

61. Mahan, G.D., *Van der Waals Forces in Solids.* The Journal of Chemical Physics, 1965. **43**(5): p. 1569-1574.

62. Rydberg, H., et al., *Van der Waals Density Functional for Layered Structures.* Physical Review Letters, 2003. **91**(12): p. 126402.

63. Rydberg, H., et al., *Hard numbers on soft matter.* Surface Science, 2003. **532-535**: p. 606-610.

64. Lundqvist, B.I., et al., *Density-functional bridge between surfaces and interfaces.* Surface Science, 2001. **493**(1): p. 253-270.

65. Benedict, L.X., et al., *Microscopic determination of the interlayer binding energy in graphite.* Chemical Physics Letters, 1998. **286**(5): p. 490-496.

66. Liu, Z., et al., *Interlayer binding energy of graphite: A mesoscopic determination from deformation.* Physical Review B, 2012. **85**(20): p. 205418.

67. Yin, M.T. and M.L. Cohen, *Structural theory of graphite and graphitic silicon.* Physical Review B, 1984. **29**(12): p. 6996-6998.

68. Schabel, M.C. and J.L. Martins, *Energetics of interplanar binding in graphite.* Physical Review B, 1992. **46**(11): p. 7185-7188.

69. Furthmüller, J., J. Hafner, and G. Kresse, *Ab initio calculation of the structural and electronic properties of carbon and boron nitride using ultrasoft pseudopotentials.* Physical Review B, 1994. **50**(21): p. 15606-15622.

70. Charlier, J.C., X. Gonze, and J.P. Michenaud, *Graphite Interplanar Bonding: Electronic Delocalization and van der Waals Interaction.* Europhysics Letters (EPL), 1994. **28**(6): p. 403-408.

71. Charlier, J.C., X. Gonze, and J.P. Michenaud, *First-Principles Study of Carbon Nanotube Solid-State Packings.* Europhysics Letters (EPL), 1995. **29**(1): p. 43-48.

72. Zhu, G., et al., *Porphyrin-based porous sheet: Optoelectronic properties and hydrogen storage.* International Journal of Hydrogen Energy, 2015. **40**(9): p. 3689-3696.

73. Girifalco, L.A. and M. Hodak, *Van der Waals binding energies in graphitic structures.* Physical Review B, 2002. **65**(12): p. 125404.

74. Klimeš, J., D.R. Bowler, and A. Michaelides, *Chemical accuracy for the van der Waals density functional.* Journal of Physics: Condensed Matter, 2009. **22**(2): p. 022201.

75. Klimeš, J., D.R. Bowler, and A. Michaelides, *Van der Waals density functionals applied to solids.* Physical Review B, 2011. **83**(19): p. 195131.

76. Ontaneda, J., et al., *Origin of the monolayer Raman signature in hexagonal boron nitride: a first-principles analysis.* Journal of Physics: Condensed Matter, 2018. **30**(18): p. 185701.

77. Pykal, M., et al., *Modelling of graphene functionalization.* Physical Chemistry Chemical Physics, 2016. **18**(9): p. 6351-6372.

78. Wu, X., et al., *Towards extending the applicability of density functional theory to weakly bound systems.* The Journal of Chemical Physics, 2001. **115**(19): p. 8748-8757.

79. Klimeš, J. and A. Michaelides, *Perspective: Advances and challenges in treating van der Waals dispersion forces in density functional theory.* The Journal of Chemical Physics, 2012. **137**(12): p. 120901.

3 Elastic and van der Waals effects in carbon-based and porphyrin nanostructures

This Chapter presents an initial comparison of carbon-based and porphyrin-based nanomaterials, in particular in terms of their interlayer interactions and bending stiffness. It will allow us to understand fundamental differences between the two types of nanostructures, and also to compare our theoretical results with available experimental binding energies and bending moduli reported for carbon nanostructures, as a way of validating some of the methods (PBE, PBE-D3 and optPBE-vdW functionals) we will employ in the rest of the thesis.

3.1 Computational details

Calculations of the graphitic and porphyrinic models were performed using DFT as implemented in the VASP program [1, 2]. Vacuum regions separating the nanostructures are always of at least 20 Å to minimise the interaction. Within the carbon-based systems, nanosheets and nanotubes were contained in a hexagonal cell to conserve the symmetry of graphitic structures. On the other hand, the simulation cell of porphyrin nanosheets was orthorhombic which consists of one Zn^{2+} centred porphyrin unit, whereas the porphyrin nanotubes were contained in a hexagonal cell to conserve the 6-fold rotation symmetry along the nanotube axis.

For geometry optimisations, the exchange and correlation potential was treated within the generalised gradient approximation (GGA) with Perdew-Burke-Ernzerhof (PBE) [3, 4] and also a dispersion-corrected PBE (PBE-D3) [5] exchange-correlation functionals.

It is well established that GGA is inadequate for the description of long-range dispersion interactions [6]. For this reason, we therefore also employ here a functional with non-local correlation (optPBE-vdW) [7, 8] which has been successfully used in modelling graphite and other layered materials [9-12]. In contrast with functionals with empirical corrections already described in previous chapters (PBE-D3), non-local correlation functionals allow for the charge density to respond to the dispersion interactions, providing a more robust description of interlayer interactions.

For both carbon- and porphyrin-based nanostructures, the projector augmented wave (PAW) method [13, 14] was used to describe the interaction between the frozen core electrons (*i.e.* up to 1*s* for C, N and 3*p* for Zn) and its valence electrons and the kinetic energy cutoff of the plane-wave basis set expansion was set at 520 eV. Equilibrium structures were found by energy minimisation until the forces on all atoms were less than 1 meV $Å^{-1}$. A Γ-centred grid of *k*-points was used for integrations in the reciprocal space, with points separated by no more than ~0.02 $Å^{-1}$ in periodic directions.

3.2 Interlayer interactions in graphite

The nature and strength of the interlayer binding in graphitic materials is poorly understood, despite the binding strength of graphite/graphene being directly relevant to some applications such as, graphene electronic devices fabricated upon various substrates, graphite intercalation compounds in Li batteries, carbon-based systems for hydrogen storage or graphene-based supercapacitors, among others [15-20].

The ability to model the binding energy (BE) for graphite is still under scrutiny due to the weak van der Waals (vdW) interlayer binding, which remains notoriously difficult to describe within standard DFT [21, 22]. In this section, I will compare the interlayer distance and the BE calculated with three functionals: PBE and PBE-D3, which belong to the standard DFT (GGA), and optPBE-vdW (developed to account for the long-range interaction component by using an explicit nonlocal functional of the density) and compare them with experimental measurements.

In **Table 3.1**, equilibrium interlayer distances obtained with these three methods exhibit that the PBE method cannot accurately describe long-distance interactions such as that of the vdW force compared with the experimental value (3.34±0.01 Å) reported in the literature [20, 23, 24]. However, it is evident that the PBE-D3 method, which takes into account empirical corrections to describe dispersion, have the same effect on the interlayer distance compared with the optPBE-vdW functional. In both, we have a difference of about ~0.02 Å which is in good agreement with the experiment.

Table 3.1. Equilibrium interlayer distances (*d*) and binding energies (BE) of graphite obtained from experiments and calculated energies using PBE, PBE-D3 and optPBE-vdW functionals.

	Exp.	PBE	PBE-D3	optPBE-vdW
***d* (Å)**	3.34±0.01 [20, 23, 24]	3.45	3.36	3.36
BE (meV/atom)	-31±2 [20, 25]	3.63	-21.5	-29.8

Nevertheless, beyond the structural properties, it is also important to compare the binding energy with reported experimental value (-31±2 meV/atom) [20, 25] to understand the behaviour of vdW interactions in graphite when they are calculated with the same three functionals. It is demonstrated that PBE functional is not capable to simulate correctly the structural properties of graphite (see **Table 3.1**) since the BE value obtained with this method shows a repulsion between layers. On the other hand, PBE-D3

and optPBE-vdW functionals exhibit attraction between graphite layers, especially the latter method (-29.8 meV/atom) is in very good agreement with the experimental value.

It is worth-mentioning that optPBE-vdW calculations may be computationally very expensive, depending on the size of the systems. For this reason, in order to have a good approach to experimental values, PBE-D3 can be used to save computing time. If we compare the energy as a function of interlayer distance (see **Figure 3.1**) it is clear that the difference between the binding energies obtained with PBE-D3 and optPBE-vdW functionals is acceptably small (~8 meV/atom).

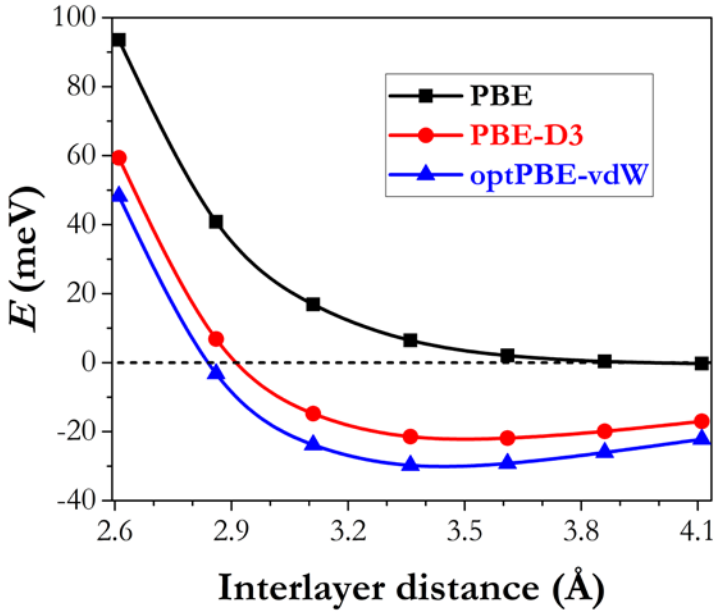

Figure 3.1. Interlayer interaction energy as a function of interlayer distance in graphite obtained from PBE, PBE-D3 and optPBE-vdW functionals.

It is already known that in graphitic-based devices, mechanical stress is almost unavoidable. For some applications, this fact cannot be ignored: strain has indeed direct effects on the electronic properties of graphene [26, 27], so it is important to understand and measure the deformation and elasticity of graphene. In the next sections, I will explain how bending stiffness can give us an overview of how graphitic and porphyrin nanostructures can be folded towards a nanotube including a comparison between the values obtained with the same three functionals used here.

3.3 Introduction to bending stiffness

Through literature, the term 'bending stiffness' will be found in several applications, such as in food packaging, shoes, tires or even textiles [28-37] to study the resistance of a structure against bending deformation. Bending stiffness should not be confused with tensile stiffness or modulus (also known as the elastic, flexural rigidity or Young's modulus) [24, 29].

Nanotubes, due to their constant curvature, are ideal model systems for calculating their bending stiffness of two-dimensional (2D) material. Rolling up a sheet of a 2D material for making a nanotube of radius R costs an elastic energy given by Eq. 3.1 [38-40]:

$$E(R) - E(\infty) = \frac{Ds}{2R^2} \tag{3.1}$$

where $E(R)$ is the energy (per atom) of the nanotubes with radius R, $E(\infty)$ is the energy (also per atom) in the zero-curvature (flat) limit, s is the surface area per atom in the material, and D is the bending stiffness or bending modulus, which has energy units.

We present then an investigation of how different functionals (PBE, PBE-D3 and optPBE-vdW) describe the bending stiffness of both carbon- and porphyrin-based nanotubes.

3.4 Bending stiffness of graphitic nanostructures

In order to compare the structural results between these functionals, the radius R has been measured after geometry optimisation of four zigzag nanotubes (n,0) of different sizes, with chiral indices (14,0), (16,0) and (18,0). **Table 3.2** shows that the optimised radii are very similar for the three functionals, with optPBE-vdW leading to the largest radius. This means that the dispersion forces are well described because comparing with experimental results [41-47], all the radii exhibited are approximately in the same proportion with

neglecting differences. However, comparing these results with the radii obtained using PBE or PBE-D3 it is clear that both, the GGA and the correction method of Grimme *et al.* [5], simulate in a proper way these graphitic materials.

Table 3.2. Carbon nanotubes radii (*R*) and bending modulus (*D*) of graphene obtained from experiments and DFT energies of nanotubes of different sizes.

	Exp.	PBE	PBE-D3	optPBE-vdW
$R_{(14,0)}$ (Å)	5.50 [45]	5.53	5.52	5.54
$R_{(16,0)}$ (Å)	6.25 [46]	6.31	6.30	6.33
$R_{(18,0)}$ (Å)	7.07 [47]	7.09	7.09	7.12
D (eV)	1.70 [48]	1.55	1.55	1.57

It is evident that both the obtained geometrical properties and the bending moduli are close to the experimental values for the three methods. The values of *D* predicted by the three functionals are almost identical, which is expected given that the main difference between them is in the treatment of long-range dispersion, whereas bending stiffness is more related to the short-range chemical bonds. The calculated *D* values agree, within the uncertainty bars, with the experimental value presented by Torres-Diaz *et al.* [48] (1.7±0.2 eV). The bending moduli can be extracted from the plots shown in **Figure 3.2**.

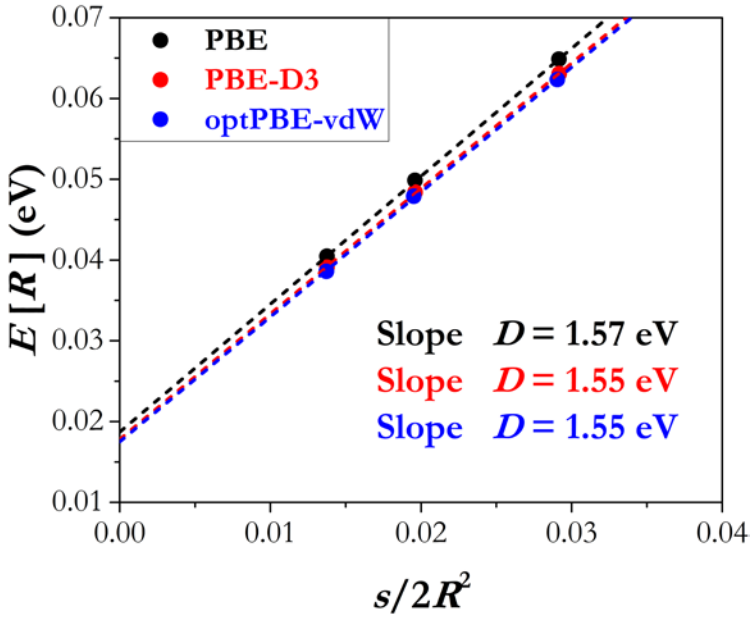

Figure 3.2. Calculation of the bending modulus of graphene from the DFT energies (*E*(*R*) from Eq. 3.1) of nanotubes of different sizes.

As explained above, optPBE-vdW is the recommended functional to be used for carbon-based structures, however this analysis of the radii and bending stiffness calculations demonstrates that our suggestion to use the less computationally demanding PBE-D3 functional to have a good approximation to experiments is valid.

3.5 Bending modulus of porphyrin-based nanostructures

The same procedure has been applied for the porphyrin-based structures, where each nanotube is formed by six porphyrin units. This cyclic array (nanoring) was selected since it has been obtained by template-directed synthesis [49] and it was observed that is possible a covalently stacking two or more of these nanorings, which forms a tube [50]. In the limit of many stacked nanorings, such structures can be seen as one-dimensional nanotubes.

The linkers between the porphyrin units were changed in order to have different radii of the porphyrin nanotubes. In this Chapter, Zn-centred porphyrins are considered which are linked via butadiyne (C4), ethyne (C2) and completely fused (C0) (see **Figure 3.3**).

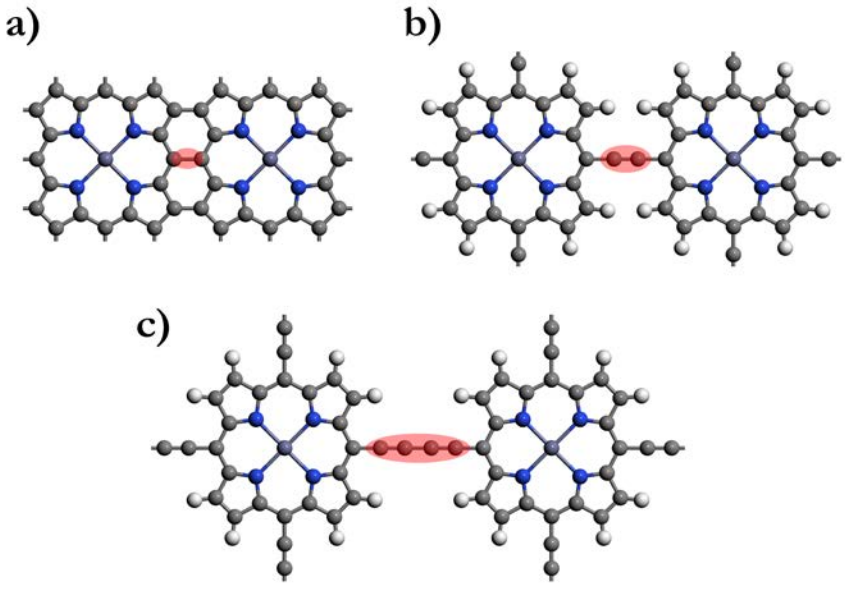

Figure 3.3. Porphyrin units a) fused (C0) and linked by b) ethyne (C2) or c) butadiyne (C4). Colour code: grey = carbon, white = hydrogen, blue = nitrogen, purple = zinc.

This type of linkage is well studied due to their interesting optical and charge transport properties [51-56]. This feature will be useful to analyse also the effect of the number of carbons (C0/C2/C4) along and around the nanotube, linking the porphyrin units (see **Figure 3.4**).

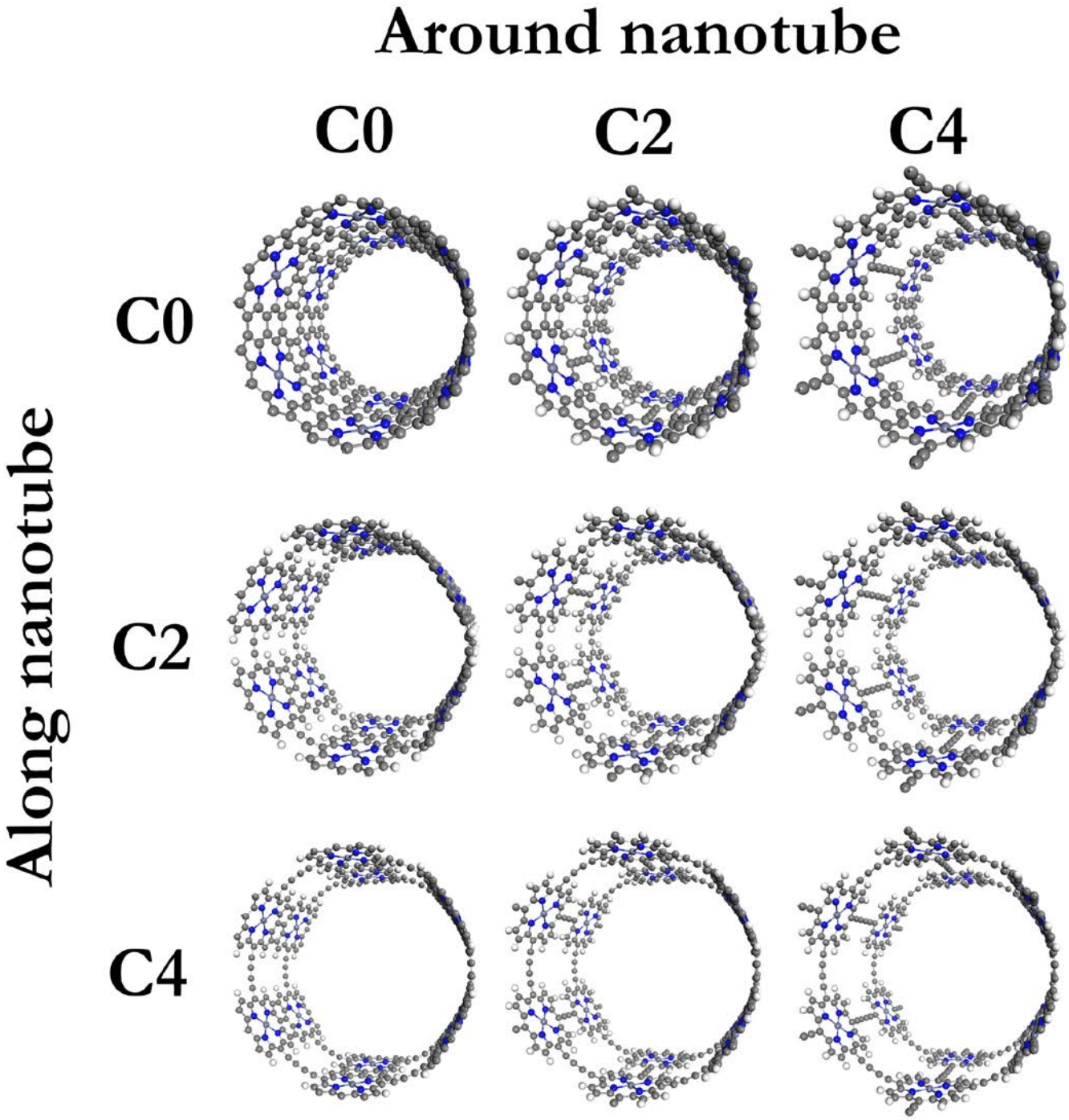

Figure 3.4. Porphyrin nanotubes with different linkers. Colour code: grey = carbon, white = hydrogen, blue = nitrogen, purple = zinc.

In **Table 3.3**, we can see the effect of the functional used on the geometry of these porphyrin-based nanotubes. It is evident that the effect of the nonlocal functional on the geometry of the porphyrin nanotubes with C0 linkers around the tube, is similar to the one observed for carbon nanotubes: the radii size increases slightly when optPBE-vdW is used. When C2- or C4-linkers are around the nanotube the resulting radii on these nanotubes are practically the same when changing the functionals. The linkage used along the nanotubes does not show any significant effect on the equilibrium radii.

Table 3.3. Porphyrin nanotubes radii measured after geometry optimisation using different functionals.

Linker around nanotube	Linker along nanotube	R_{PBE} (Å)	$R_{PBE\text{-}D3}$ (Å)	$R_{optPBE\text{-}vdW}$ (Å)
C0	C0	8.04	8.03	8.06
	C2	8.04	8.04	8.06
	C4	8.04	8.04	8.06
C2	C0	10.30	10.30	10.31
	C2	10.26	10.26	10.26
	C4	10.27	10.26	10.26
C4	C0	12.74	12.74	12.76
	C2	12.74	12.74	12.74
	C4	12.74	12.74	12.74

Regarding the bending stiffness for the porphyrin nanotubes, porphyrin nanosheets were constructed with the different possible combinations of linkers considered for the nanotubes. Instead of folding these sheets with different tube radii, which would be too computationally expensive, we extract the approximate bending modulus in each case from one single *R* value using Equation 3.1. The results are shown in **Table 3.4**.

Table 3.4. Bending moduli of porphyrin nanosheets considering DFT energies of nanotubes of different sizes.

Linker around nanotube	Linker along nanotube	D_{PBE} (eV)	$D_{PBE\text{-}D3}$ (eV)	$D_{optPBE\text{-}vdW}$ (eV)
C0	C0	1.06	1.03	0.99
	C2	0.84	0.82	0.79
	C4	0.68	0.65	0.65
C2	C0	0.36	0.35	0.31
	C2	0.23	0.22	0.20
	C4	0.20	0.19	0.17
C4	C0	0.45	0.43	0.42
	C2	0.32	0.31	0.31
	C4	0.26	0.25	0.25

As in the case of the carbon nanotubes, the functional chosen has little influence on the calculated bending moduli. For all combinations, the *D* values are lower than those found for carbon nanotubes, which indicates that the strain in these porphyrin tubes are generally lower than in their carbon analogues. Interestingly, and in contrast with the calculated radii, the *D* values depend on both the nature of the linker around and along the nanotube. The highest bending modulus is found for the C0-C0 nanotubes. Increasing the length of the linker from C0 to C4 along the nanotube always reduces the *D* value, because that reduces the density of bonds to be bent. The trend with the length of the linker along the nanotube is, however, not monotonous; *e.g.* D[C0-C0] > D[C0-C2] < D[C0-C4], where the first linker inside the brackets refers to the ones along the nanotube and the second to the ones around the nanotubes. This might be due to the fact that the nanotubes with C4 linkers have a longer radius than the C2. The bending stiffness characterises the energy required to create a given curvature. Although it should take more energy to bend the system along C2 linkers than along the C4 linkers to create the *same curvature*, the curvatures are different, which might be leading to non-monotonous trend. In any case, the calculations presented here are only approximate, so these small variations in *D* could be affected by the approximations made. A more rigorous analysis would involve considering different radii (as we did for graphene) for each type of connectivity,

rather than extracting the *D* values for a single point. The computational cost of such study would be very large, so this analysis is left for future work.

3.6 Conclusion

We have presented an investigation of intralayer and interlayer interactions in graphene- and porphyrin-based nanostructures, using three different functionals: PBE, PBE-D3 and optPBE-vdW.

PBE is unable to describe the interlayer attraction that results from dispersion forces, due the absence of nonlocal correlations. The interlayer distances in graphite obtained from either PBE-D3 (which incorporates an empirical dispersion correction) or optPBE-vdW (which implements nonlocal correlation) exhibit good agreement with experiment. The binding energy of layers in graphite is also reasonably described by both of these functionals.

The intralayer interactions are characterised in terms of the bending stiffness, in particular the bending modulus *D*. The bending modulus of graphene, calculated using nanotubes of different radii, is almost independent of the functional used, and in good agreement with experiment.

The bending modulus of porphyrin-based nanostructures depends strongly on the nature of linker units used both along the nanotube and around the direction of folding. As expected, the bending stiffness is highest for the C0 nanotubes, because in the absence of linkers the porphyrin units have to accommodate the strain by distorting their planar structure. Also, it seems that PBE or PBE-D3 methods are enough to properly simulate geometries and bending modulus of porphyrin-based structures. The differences obtained between the results of the three functionals are negligible.

Overall, PBE-D3 seems like a good compromise in terms of adequate description of intralayer and interlayer interactions, and we will use this functional in most of the work

reported in this thesis. One exception is when we need to obtain accurate band structures, *e.g.* in **Chapter 6** for which we will use HSE06. The other exception is in the investigation of the effect of electric field on graphitic edges, reported in **Chapter 4**, where the effect of the field on the polarisation of the electric charge responsible for dispersion corrections could be significant. In that latter case, we use optPBE-vdW, which gives a charge density that is consistent with the dispersion interaction.

3.7 References

1. Kresse, G., Furthmüller, J., *Efficient iterative schemes for ab initio total-energy calculations using a plane-wave basis set.* Phys. Rev. B: Condens. Matter Mater. Phys., 1996. **54**(16): p. 11169 - 11186.
2. Kresse, G., Furthmüller, J., *Efficiency of ab-initio total energy calculations for metals and semiconductors using a plane-wave basis set.* Comput. Mater. Sci., 1996. **6**: p. 15 - 50.
3. Perdew, J.P., K. Burke, and M. Ernzerhof, *Generalized Gradient Approximation Made Simple.* Physical Review Letters, 1996. **77**(18): p. 3865-3868.
4. Perdew, J.P., K. Burke, and M. Ernzerhof, *Generalized Gradient Approximation Made Simple [Phys. Rev. Lett. 77, 3865 (1996)].* Physical Review Letters, 1997. **78**(7): p. 1396-1396.
5. Grimme, S., et al., *A consistent and accurate ab initio parametrization of density functional dispersion correction (DFT-D) for the 94 elements H-Pu.* The Journal of Chemical Physics, 2010. **132**(15): p. 154104.
6. Berland, K., et al., *van der Waals forces in density functional theory: a review of the vdW-DF method.* Reports on Progress in Physics, 2015. **78**(6): p. 066501.
7. Klimeš, J., D.R. Bowler, and A. Michaelides, *Chemical accuracy for the van der Waals density functional.* J. Phys. Condens. Matter., 2010. **22**(2): p. 022201.

8. Klimeš, J., D.R. Bowler, and A. Michaelides, *Van der Waals density functionals applied to solids.* Physical Review B, 2011. **83**(19): p. 195131.

9. Ontaneda, J., et al., *Origin of the monolayer Raman signature in hexagonal boron nitride: a first-principles analysis.* Journal of Physics: Condensed Matter, 2018. **30**(18): p. 185701.

10. Pykal, M., et al., *Modelling of graphene functionalization.* Phys. Chem. Chem. Phys., 2016. **18**(9): p. 6351-6372.

11. Wu, X., et al., *Towards extending the applicability of density functional theory to weakly bound systems.* The Journal of Chemical Physics, 2001. **115**(19): p. 8748-8757.

12. Klimeš, J. and A. Michaelides, *Perspective: Advances and challenges in treating van der Waals dispersion forces in density functional theory.* The Journal of Chemical Physics, 2012. **137**(12): p. 120901.

13. Blöchl, P.E., *Projector augmented-wave method.* Phys. Rev. B, 1994. **50**(24): p. 17953-17979.

14. Kresse, G. and D. Joubert, *From ultrasoft pseudopotentials to the projector augmented-wave method.* Phys. Rev. B, 1999. **59**(3): p. 1758-1775.

15. Geim, A.K., *Graphene: Status and Prospects.* Science, 2009. **324**(5934): p. 1530.

16. Geim, A.K. and K.S. Novoselov, *The rise of graphene.* Nature Materials, 2007. **6**: p. 183.

17. Stoller, M.D., et al., *Graphene-Based Ultracapacitors.* Nano Letters, 2008. **8**(10): p. 3498-3502.

18. Mohanty, N. and V. Berry, *Graphene-Based Single-Bacterium Resolution Biodevice and DNA Transistor: Interfacing Graphene Derivatives with Nanoscale and Microscale Biocomponents.* Nano Letters, 2008. **8**(12): p. 4469-4476.

19. Du, X., et al., *Approaching ballistic transport in suspended graphene.* Nature Nanotechnology, 2008. **3**(8): p. 491-495.

20. Liu, Z., et al., *Interlayer binding energy of graphite: A mesoscopic determination from deformation.* Physical Review B, 2012. **85**(20): p. 205418.

21. Spanu, L., S. Sorella, and G. Galli, *Nature and Strength of Interlayer Binding in Graphite.* Physical Review Letters, 2009. **103**(19): p. 196401.

22. Lebègue, S., et al., *Cohesive Properties and Asymptotics of the Dispersion Interaction in Graphite by the Random Phase Approximation.* Physical Review Letters, 2010. **105**(19): p. 196401.

23. Çakmak, G. and T. Öztürk, *Continuous synthesis of graphite with tunable interlayer distance.* Diamond and Related Materials, 2019. **96**: p. 134-139.

24. Lambin, P., *Elastic Properties and Stability of Physisorbed Graphene.* Applied Sciences, 2014. **4**(2): p. 282-304.

25. Benedict, L.X., et al., *Microscopic determination of the interlayer binding energy in graphite.* Chemical Physics Letters, 1998. **286**(5): p. 490-496.

26. Farjam, M. and H. Rafii-Tabar, *Comment on ``Band structure engineering of graphene by strain: First-principles calculations''.* Physical Review B, 2009. **80**(16): p. 167401.

27. Li, Y., et al., *Strain effects in graphene and graphene nanoribbons: The underlying mechanism.* Nano Research, 2010. **3**(8): p. 545-556.

28. Fahy, F., *7 - Sound Absorption and Sound Absorbers*, in *Foundations of Engineering Acoustics*, F. Fahy, Editor. 2001, Academic Press: London. p. 140-180.

29. Morris, B.A., *9 - Strength, Stiffness, and Abuse Resistance*, in *The Science and Technology of Flexible Packaging*, B.A. Morris, Editor. 2017, William Andrew Publishing: Oxford. p. 309-350.

30. Hunter, L. and J. Fan, *Chapter 28 - Adding Functionality to Garments*, in *Textiles and Fashion*, R. Sinclair, Editor. 2015, Woodhead Publishing. p. 705-737.

31. Mills, N.J., *Chapter 13 - Running shoe case study*, in *Polymer Foams Handbook*, N.J. Mills, Editor. 2007, Butterworth-Heinemann: Oxford. p. 307-327.

32. François, R., S. Laurens, and F. Deby, *6 - Prediction of Bearing Capacity and Behavior in Service of Corroded Structures*, in *Corrosion and its Consequences for Reinforced Concrete Structures*, R. François, S. Laurens, and F. Deby, Editors. 2018, Elsevier. p. 135-173.

33. Skinner, L., *Chapter 4 - Snubbing Theory and Calculations*, in *Hydraulic Rig Technology and Operations*, L. Skinner, Editor. 2019, Gulf Professional Publishing. p. 189-275.

34. Bai, Q. and Y. Bai, *25 - Cross-Sectional and Dynamic Analyses of Flexible Pipes*, in *Subsea Pipeline Design, Analysis, and Installation*, Q. Bai and Y. Bai, Editors. 2014, Gulf Professional Publishing: Boston. p. 579-598.

35. Farkas, J. and K. Jármai, *5 - Large-span Suspended Roof Members*, in *Design and Optimization of Metal Structures*, J. Farkas and K. Jármai, Editors. 2008, Woodhead Publishing. p. 47-56.

36. Abe, M. and W. Manning, *Chapter 2 - Tire Mechanics*, in *Vehicle Handling Dynamics*, M. Abe and W. Manning, Editors. 2009, Butterworth-Heinemann: Oxford. p. 5-46.

37. Wang, Z. and S. Hirai. *A Soft Gripper with Adjustable Stiffness and Variable Working Length for Handling Food Material.* in *2018 IEEE International Conference on Real-time Computing and Robotics (RCAR)*. 2018.

38. Robertson, D.H., D.W. Brenner, and J.W. Mintmire, *Energetics of nanoscale graphitic tubules.* Physical Review B, 1992. **45**(21): p. 12592-12595.

39. Adams, G.B., et al., *Energetics of Large Fullerenes: Balls, Tubes, and Capsules.* Science, 1992. **256**(5065): p. 1792.

40. Posligua, V., et al., *The closed-edge structure of graphite and the effect of electrostatic charging.* RSC Advances, 2020. **10**(13): p. 7994-8001.

41. Jiang, H., et al., *The effect of nanotube radius on the constitutive model for carbon nanotubes.* Computational Materials Science, 2003. **28**(3): p. 429-442.

42. Chen, G., et al., *Diameter control of single-walled carbon nanotube forests from 1.3–3.0 nm by arc plasma deposition.* Scientific Reports, 2014. **4**(1): p. 3804.

43. Goze, C., et al., *Elastic and mechanical properties of carbon nanotubes.* Synthetic Metals, 1999. **103**(1): p. 2500-2501.

44. Gao, G., T. Çagin, and W.A. Goddard, *Energetics, structure, mechanical and vibrational properties of single-walled carbon nanotubes.* Nanotechnology, 1998. **9**(3): p. 184-191.

45. Avramov, P.V., B.I. Yakobson, and G.E. Scuseria, *Effect of carbon network defects on the electronic structure of semiconductor single-wall carbon nanotubes.* Physics of the Solid State, 2004. **46**(6): p. 1168-1172.

46. Yang, F., et al., *Growing Zigzag (16,0) Carbon Nanotubes with Structure-Defined Catalysts.* Journal of the American Chemical Society, 2015. **137**(27): p. 8688-8691.

47. Hedman, D., et al., *On the Stability and Abundance of Single Walled Carbon Nanotubes.* Scientific Reports, 2015. **5**(1): p. 16850.

48. Torres-Dias, A.C., et al., *From mesoscale to nanoscale mechanics in single-wall carbon nanotubes.* Carbon, 2017. **123**: p. 145-150.

49. Hoffmann, M., et al., *Enhanced π Conjugation around a Porphyrin[6] Nanoring.* Angewandte Chemie International Edition, 2008. **47**(27): p. 4993-4996.

50. Neuhaus, P., et al., *A Molecular Nanotube with Three-Dimensional π-Conjugation.* Angewandte Chemie International Edition, 2015. **54**(25): p. 7344-7348.

51. Lin, V.S., S.G. DiMagno, and M.J. Therien, *Highly conjugated, acetylenyl bridged porphyrins: new models for light-harvesting antenna systems.* Science, 1994. **264**(5162): p. 1105.

52. Susumu, K., et al., *Conjugated Chromophore Arrays with Unusually Large Hole Polaron Delocalization Lengths.* Journal of the American Chemical Society, 2006. **128**(26): p. 8380-8381.

53. Sedghi, G., et al., *Comparison of the Conductance of Three Types of Porphyrin-Based Molecular Wires: β,meso,β-Fused Tapes, meso-Butadiyne-Linked and Twisted meso-meso Linked Oligomers.* Advanced Materials, 2012. **24**(5): p. 653-657.

54. Tsuda, A. and A. Osuka, *Fully Conjugated Porphyrin Tapes with Electronic Absorption Bands That Reach into Infrared.* Science, 2001. **293**(5527): p. 79.

55. Anderson, H.L., *Conjugated Porphyrin Ladders.* Inorganic Chemistry, 1994. **33**(5): p. 972-981.

56. Taylor, P.N., et al., *Conjugated porphyrin oligomers from monomer to hexamer.* Chemical Communications, 1998(8): p. 909-910.

4 Closed edges in graphitic nanostructures: thermodynamics and effect of electric fields

This Chapter is about the edges of graphite (or few-layer graphene). There is still much that it is not clear about the geometry and stability of these edges. I will present a theoretical study of the so-called "closed" edges of graphite, and of the effect of an electric field on their structure. Experimental results of high-resolution transmission electron microscopy, carried out by our collaborator Dr Peter Harris, are included in this Chapter for comparison with our simulations. We show the behaviour of the edge structure of graphite that has been exposed to an electric field, which experiences a separation of the graphene layers. Computer simulations based on density functional density (DFT) are used to rationalise and quantify the preference for the formation of multiple concentric loops at the edges. A model is also presented to explain how the application of an electric field leads to the separation of the folded edges.

This section has been published in the journal *RCS Advances* (*RSC Adv.*, 2020, 10, 7994).

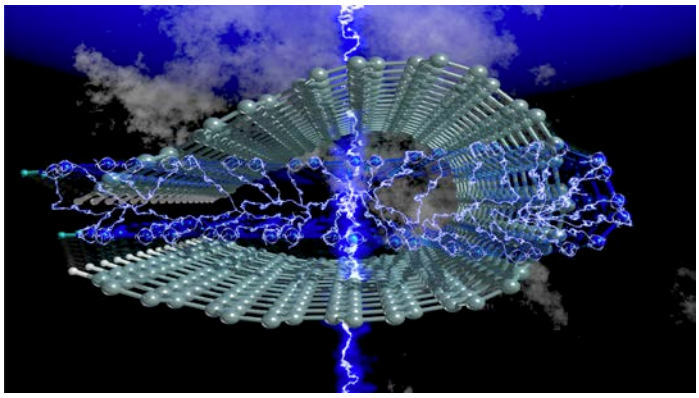

Image caption: Electric field in a folded nanoribbon. Net forces on the atoms tend to pull the oppositely charged layers apart.

4.1 Introduction

Much of what we know about the microstructure of carbon materials has come from studies using transmission electron microscopy (TEM) [1]. Often, such studies have shown that the simple textbook pictures that we have of graphite, diamond and other forms of carbon need to be modified. For example, graphite is traditionally portrayed as consisting of individual, unconnected graphene layers stacked one above the other, but TEM has shown that in reality the graphene sheets are frequently joined at the edges by arched structures which encompass two or more adjacent layers, forming "closed" edges [2-4].

The formation of closed edges in graphitic structures has important consequences, which makes them the subject of research interest. First, the edge structure can influence the optical, magnetic, electrical, and electronic properties of graphite and of few-layer graphene [5, 6]. A theoretical study by Yan *et al.* [7] has recently shown that AB-stacked closed-edge bilayer graphene exhibits band gap opening and charge separation, which suggests potential applications in electronic devices, such as solar cells. In some cases, closed edges in graphite may be undesirable, *e.g.* their presence can prevent the production of graphene by exfoliation of highly oriented pyrolytic graphite (HOPG). The experimental results presented in this paper were obtained using commercial graphite, produced by the high temperature treatment of coke, leading to a less perfect structure that of HOPG. However, closed edges, as well as structural transformations due to electric charging, have also been reported for HOPG [8]. Finally, another motivation to investigate the properties of closed edges is that they are structurally similar to collapsed nanotube structures [9], which have increasing technological relevance [10]. It is known that multi-walled carbon nanostructures above a certain critical diameter (which depends on the number of walls [11]) tend to collapse and form nearly-flat structures with concentric loops at the edges. However, the analogy between graphitic closed edges and collapsed nanotubes is not exact,

because in the former case the packing of the loops at the edges introduces a constraint in their diameters, which must match an integer number of interlayer distances, whereas in collapsed nanotubes "dog-bone" cross-sections are typically formed.

In this Chapter, I will present the combined theoretical and experimental investigation of the closed edges of graphite. They are best presented together to understand the study, but my work was only the theoretical part. The experimental part was carried out by Dr Peter Harris at Reading. His TEM studies of the edge structure of graphite will be described, showing the formation of concentric loops. The images of graphite samples that have been exposed to an electric field are reported. It is now well established that electric fields can transform the structure of carbon materials [8, 12-21] but the mechanism of transformation is poorly understood. An earlier study suggested that the mechanism involved, in part, a separation of the closed graphite edges. Here, the separation process is studied in detail and use high-tilt imaging to determine the overall shapes of the transformed structures. My theoretical analysis, based on DFT simulations, of the thermodynamics of closed edges and the effect of an electric field, helps to interpret the observed TEM images. Previous theoretical work [22] has focused on the geometry and electronic structure of closed-edge graphitic nanoribbons, without consideration of their relative stabilities. Here, it has been calculated the variation of surface energy of the edge as a function of the number of concentric folds, demonstrating that the formation of multiple folds is thermodynamically favoured. It is also elucidated the mechanism by which an electric field expands the closed edges, explaining the structural transformations observed in experiment.

4.2 Methods

4.2.1 Experimental

The graphite used in the experiments consisted of commercial synthetic graphite rods obtained from Quorum Technologies Ltd, UK. Samples of the fresh rods were prepared for TEM by grinding in an agate mortar under isopropanol, mixing in an ultrasonic bath and depositing onto lacey carbon TEM grids. Edges of the graphite crystals were then imaged using a JEOL 2010 microscope, with a point resolution of 0.19 nm, operated at 200 kV. At this accelerating voltage there is a danger of irradiation damage [23], since the threshold for knock-on damage is well below 200 kV. Experiments carried out with the samples studied here showed that visible damage occurred only after about 2 min exposure to a beam with a current density of 15 pA cm^{-2}. Care was taken not to expose the carbon to an electron for longer than this time.

In order to pass a current through the graphite, a commercial arc-evaporator, which is normally used for carbon-coating specimens for electron microscopy, was employed. In this unit, the electrodes are graphite rods, one of which is thinned to a diameter of approximately 1.4 mm at the point of contact. The chamber is evacuated by a turbomolecular pump to a pressure of approximately 3×10^{-4} mbar. Before carrying out the "evaporation", the rods are out-gassed by passing a current of about 30 A for 1 min. Some samples of graphite which had just been exposed to the out-gassing step were examined by TEM and no obvious structural changes were observed. For evaporation, a current of 75 A is passed for 3 s. Following evaporation, the thinned carbon rod was found to have slightly shortened, and a small deposit was formed in the area where the two rods made contact. This was collected and imaged in the TEM as described above.

4.2.2 Theory

We use the Vienna *Ab Initio* Simulation Package (VASP) [24, 25] to carry out the quantum mechanical calculations within the Kohn-Sham implementation of the density functional theory (DFT). It is well established that the generalised gradient approximation (GGA), which is widely used in DFT simulations, is inadequate for the description of long-range dispersion interactions [26], which play an important role in graphitic structures. Although the local density approximation (LDA) of DFT does lead to interlayer binding and is sometimes used to investigate graphitic and other layered structures, including in previous work on closed-edged structures [22], this approximation is also unable to provide an adequate description of long-range dispersion interactions [18]. Therefore, a functional with nonlocal correlation is employed (optPBE-vdW) [27, 28] which has been successfully used in modelling graphite and other layered materials [29-32]. In contrast with functional with an empirical correction added to describe dispersion, like those proposed by Grimme *et al.* [33, 34], nonlocal correlation functionals allow for the charge density to respond to the dispersion interactions, providing a more robust description of interlayer interactions. This functional also gives a good description of the bending stiffness of graphene layers, which is necessary for investigating the thermodynamics of closed edges.

Following the same procedure detailed in **Section 3.4**, we have calculated the bending modulus D of graphene from DFT energies (using the optPBE-vdW functional) of three zigzag nanotubes of different sizes. By plotting their energy vs. the square of their radii (see **Figure 4.1**), we obtain a bending modulus D = 1.57 eV, in agreement with the experimental value of 1.7±0.2 eV [35].

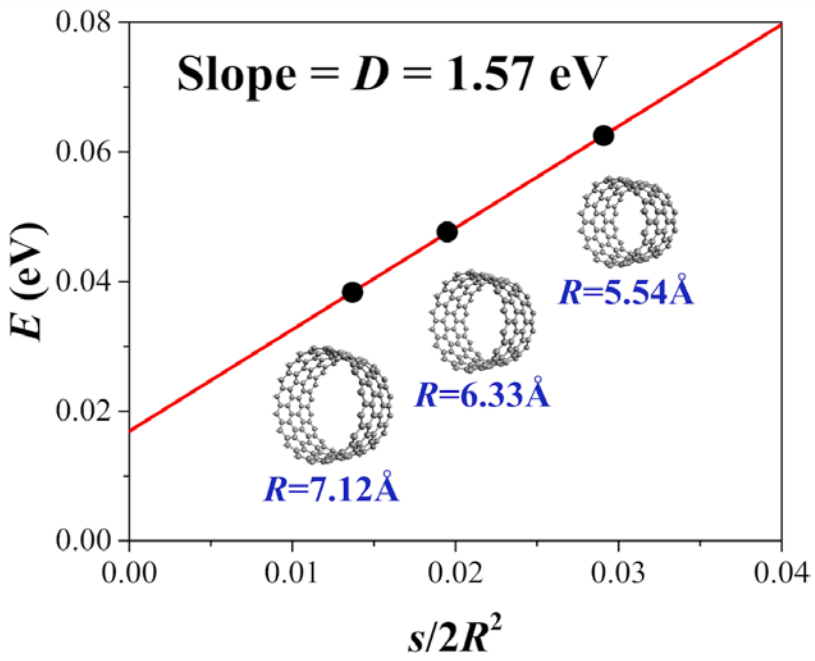

Figure 4.1. Calculation of the bending modulus of graphene from optPBE-vdW energies of nanotubes of different sizes.

Valence wavefunctions are expanded in terms of planewaves with kinetic energies up to 520 eV. The interaction of the valence electrons with the ionic cores is modelled using the projector augmented wave (PAW) method [36, 37], with C 1*s* levels frozen at the atomic reference state. Equilibrium structures were found by energy minimisation until the forces on all atoms were less than 1 meV Å^{-1}. A Γ-centred grid of *k*-points was used for integrations in the reciprocal space, with points separated by no more than ~0.02 Å^{-1} in periodic directions.

The surface energy (γ), which characterises the stability of a particular surface termination (for the edges in this case), was calculated as:

$$\gamma = \frac{E_{\text{slab}} - NE_{\text{bulk}}}{2A} \tag{4.1}$$

where E_{slab} is the energy per unit cell of a periodic slab with N carbon atoms and the graphitic edges pointing towards the vacuum gap, E_{bulk} is the energy per atom of bulk graphite, and A is the area per unit cell at each side of the slab. As VASP employs 3D periodic boundary conditions, all our models include vacuum regions of ~10 Å separating

the slabs, which were proved to be large enough not to affect the equilibrium geometries and surface energies.

In the simulations involving an electric field, we applied a periodic sawtooth-like potential perpendicular to the layers, as done by other authors (*e.g.* Ref. [38]). The induced charge redistribution is visualised as the difference in charge density with and without electric field.

4.3 Results and discussion

4.3.1 TEM of graphite edges

A typical image of material from the fresh graphite is shown in **Figure 4.2**. As expected, this consists mainly of flat crystallites, ranging from a few 100 nm to about 5 μm in size, containing up to 100 layers. The crystallites were often folded and buckled and were covered with small amounts of finely-divided material. No nanotubes or other fullerene-related structures were seen in the fresh graphite.

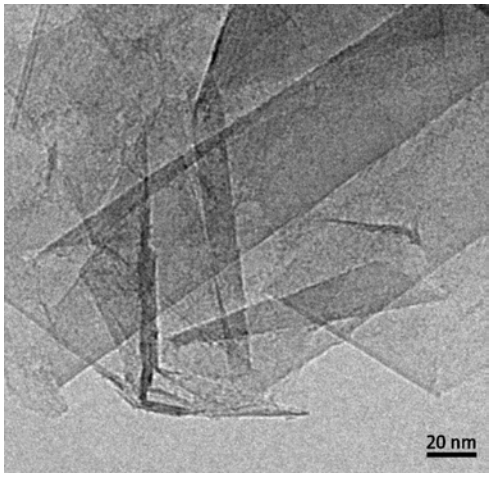

Figure 4.2. Transmission electron micrograph of carbon from fresh graphite rod.

The graphite sheets tended to lie flat on the carbon support films, with the *c*-axis parallel to the electron beam. However, it was possible to find crystals oriented with the graphene planes parallel to the electron beam, and a number of images were recorded of

the edges of such crystals. In some cases, the edges were completely open, with no connections between adjacent layers, but in other cases the layers were clearly joined by arched structures.

Different edge structures were observed, as shown in **Figure 4.3**. Single loops (see **Figure 4.3a**) were sometimes seen, but multiple loops, as in the other images, were more common. **Figure 4.3c** appears to show some loops in the process of being formed.

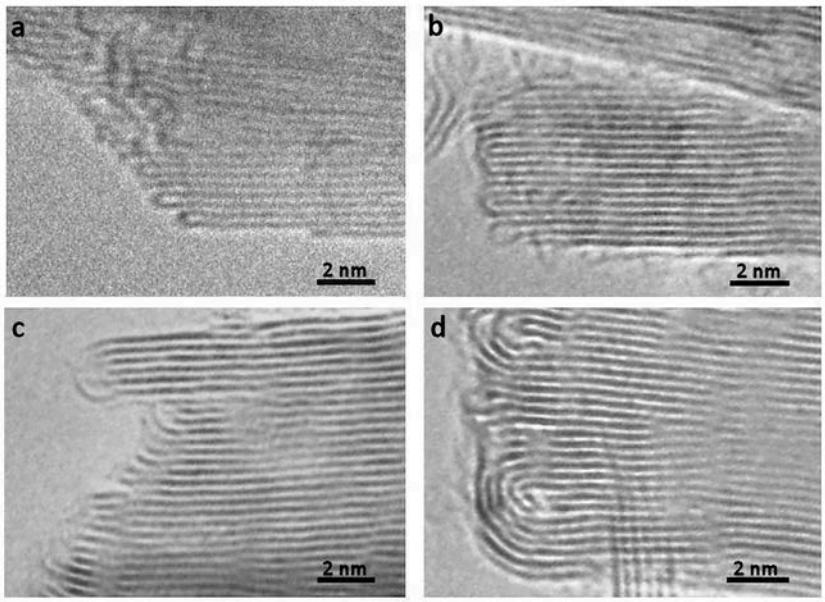

Figure 4.3. TEM images of looped edges in fresh graphite. a) Edge with single loops, b) edge with single and multiple loops, c) loops apparently in the process of being formed and d) multiple loops.

4.3.2 Thermodynamics of closed edges from DFT calculations

In order to understand the thermodynamics of edge folding in graphitic structures, and in particular the formation of multiple concentric loops or folds, we resort to DFT simulations. We focus our simulations on the zigzag edge of graphite, because the geometry of the armchair edge is incompatible with the formation of a closed edge for AB stacking, as noted before by Zhan *et al.* [39]. Using the case of a single fold (n_f = 1), we first checked that our model, consisting of a continuously folded graphene sheet (**Figure 4.4**), is long enough to represent both the closed edge and the graphite bulk, leading to

converged surface energies. We consider models with 48, 56 and 64 atoms per unit cell, and found that the surface energy is indeed well converged, to γ_1 = 2.99 J m^{-2}, with differences between models below 0.01 J m^{-2}. We are therefore confident that there is negligible interaction between the two sides of the slabs.

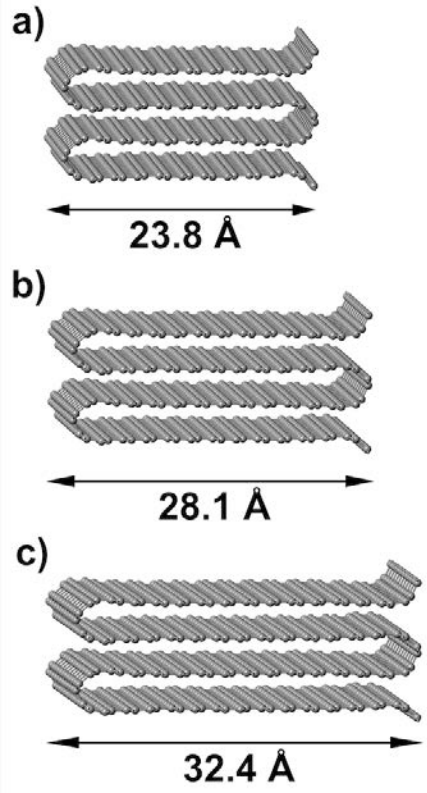

Figure 4.4. Slab models for the folded edges, including a) 48 C atoms, b) 56 C atoms, and c) 64 C atoms per simulation cell. The model is periodic in the two directions parallel to the edge plane, where a vacuum gap separates the slabs in the direction perpendicular to the edge plane.

We now consider the formation of edges with two (**Figure 4.5b**) or three (**Figure 4.5c**) concentric folds (n_f = 2, 3). Like the single-fold edge model, these models exhibit AB stacking in the bulk region at the centre of the slabs, which remained largely unchanged upon geometry optimisation. The corresponding surface energies are γ_2 = 2.13 J m^{-2} and γ_3 = 1.78 J m^{-2} (for n_f = 2 and 3, respectively). It is clear that the formation of concentric loops lowers the surface energy, stabilising the edge termination. This effect results from the smaller bending stress in the external folds, which have less curvature.

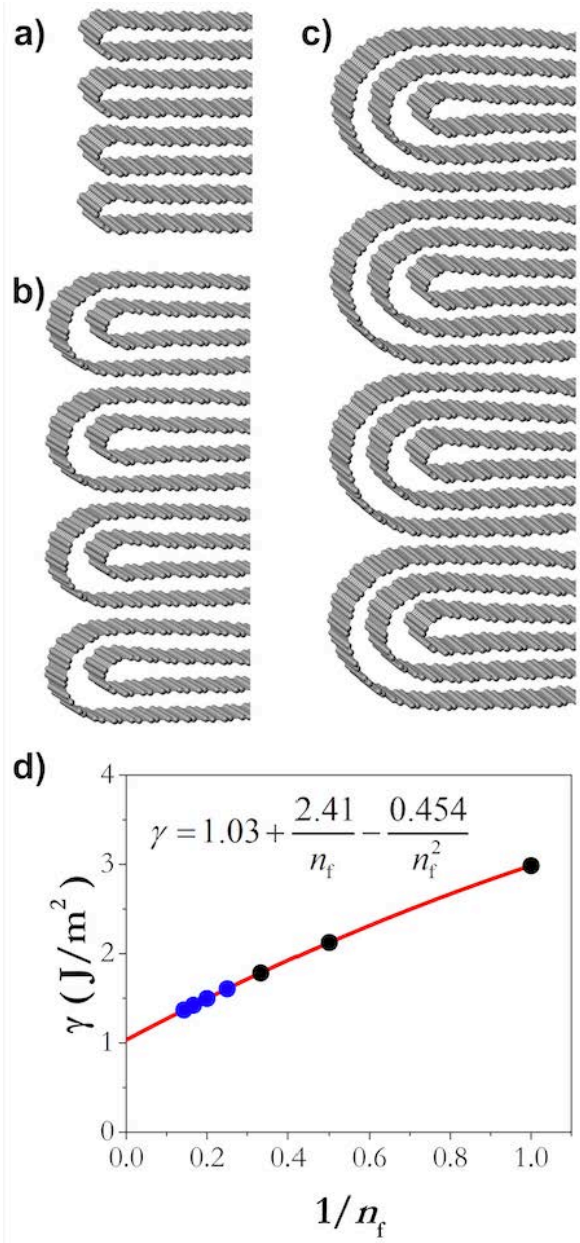

Figure 4.5. Graphitic edges with repetitions of a) a single fold (n_f = 1), b) two concentric folds (n_f = 2), and c) three concentric folds (n_f = 3). d) Variation of the surface energy γ with the number of concentric folds (n_f). Black dots represent the values calculated directly from DFT results using Eq. 4.1 and the blue dots and red line represent the extrapolation described in the text.

In fact, it is possible to calculate the effective strain energies ε_n (per unit of edge length) introduced by folds of different curvature (connecting layers which are separated by a distance $(2n-1)d$, where d is the interlayer distance in graphite). Assuming that such strain is the dominant contribution to the surface energies, and therefore ignoring

dispersion and other effects, the above calculated surface energies can be expressed in an additive way, as:

$$\gamma_1 = \frac{\varepsilon_1}{2d} \tag{4.2}$$

$$\gamma_2 = \frac{\varepsilon_1 + \varepsilon_2}{4d} \tag{4.3}$$

$$\gamma_3 = \frac{\varepsilon_1 + \varepsilon_2 + \varepsilon_3}{6d} \tag{4.4}$$

In the numerators of Eqs. 4.2 – 4.4, we account for the different folded edges contributing to each surface (*e.g.* $\varepsilon_1 a$ is the extra energy due to the presence of a single fold), whereas in the denominator we account for the different surface areas, which are $2da$, $4da$ and $6da$, for n_f = 1, 2 and 3, respectively (a is the edge length, which cancels out from the numerator and denominator). From these expressions, we can determine the effective strain energies: ε_1 = 1.25 eV Å^{-1}, ε_2 = 0.53 eV Å^{-1} and ε_3 = 0.46 eV Å^{-1}. They deviate from the pure strain values, which can be obtained from the calculated bending modulus D of graphene (assuming the folds are semi-cylindrical) as: $\pi D/d$ = 1.48 eV Å^{-1}, $\pi D/3d$ = 0.49 eV Å^{-1} and $\pi D/5d$ = 0.30 eV Å^{-1}, respectively, because there are other contributions to the edge energy not included in the approximate model given by Eqs. 4.2 – 4.4 (*e.g.* dispersion interactions between the loops). Nevertheless, it is clear from the above analysis that the bending strain, which decreases with loop diameter, is the main factor driving the formation of concentric folds structures.

We can now extrapolate our results to obtain surface energies for edges consisting of arbitrary numbers of concentric folds (experimentally, it is common to find edge structures with more than three concentric folds, as shown in **Figure 4.3**). Based on theoretical results for carbon nanotubes [40, 41], the strain energy ε_n can be expected to vary linearly with the inverse of the square of the loop diameter in each fold, which

corresponds to "opening distance" $d_n = (2n-1)d$ of the fold. This is indeed the case for the three values (ε_1, ε_2, ε_3) calculated directly from DFT simulations, as shown in **Figure 4.6**, and is consistent with the observed variation of strain energy in carbon nanotubes as a function of size.

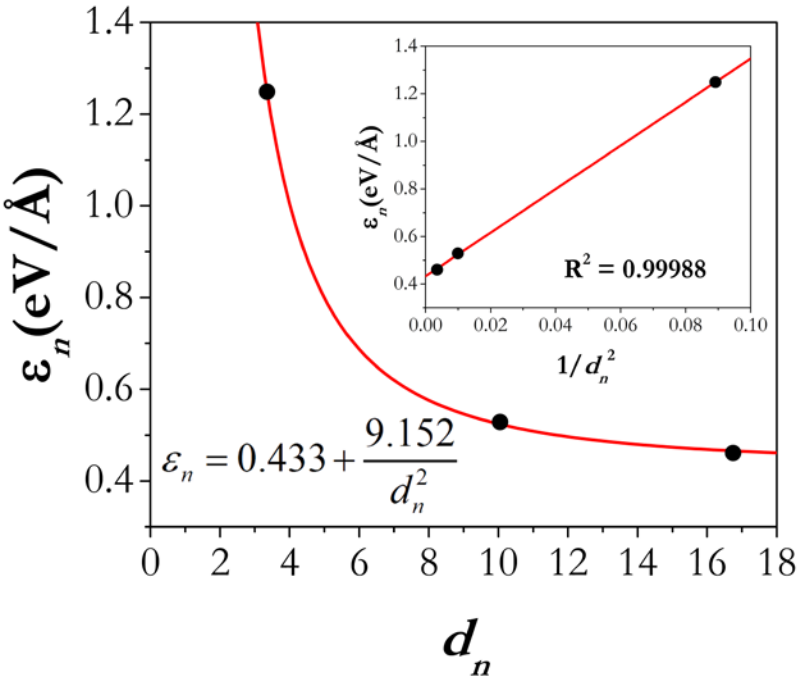

Figure 4.6. Variation of the strain energy with the loop diameter ("opening distance" d_n).

We now write this dependence as:

$$\varepsilon_n = \alpha + \frac{\beta}{d_n^2} \tag{4.5}$$

where α = 0.433 and β = 9.152 from the fitting of the DFT data (**Figure 4.6**). The surface energy of the edge consisting of a periodic repetition of n_f concentric folds can be calculated as:

$$\begin{aligned}\gamma_{n_f} &= \frac{1}{2n_f d}\sum_{n=1}^{n_f}\left(\alpha + \frac{\beta}{(2n-1)^2 d^2}\right) \\ &= \frac{1}{2n_f d}\left(\alpha n_f + \frac{\beta}{d^2}\sum_{n=1}^{n_f}\frac{1}{(2n-1)^2}\right) \\ &= \frac{\alpha}{2d} + \frac{\beta}{2d^3 n_f} f(n_f)\end{aligned} \tag{4.6}$$

where:

$$f(n_f) = \sum_{n=1}^{n_f}\frac{1}{(2n-1)^2} \approx \frac{\pi^2}{8} - \frac{\zeta}{n_f} \tag{4.7}$$

and $\zeta \approx 0.2384$. The validity of the approximate expression above is clear from **Figure 4.7**.

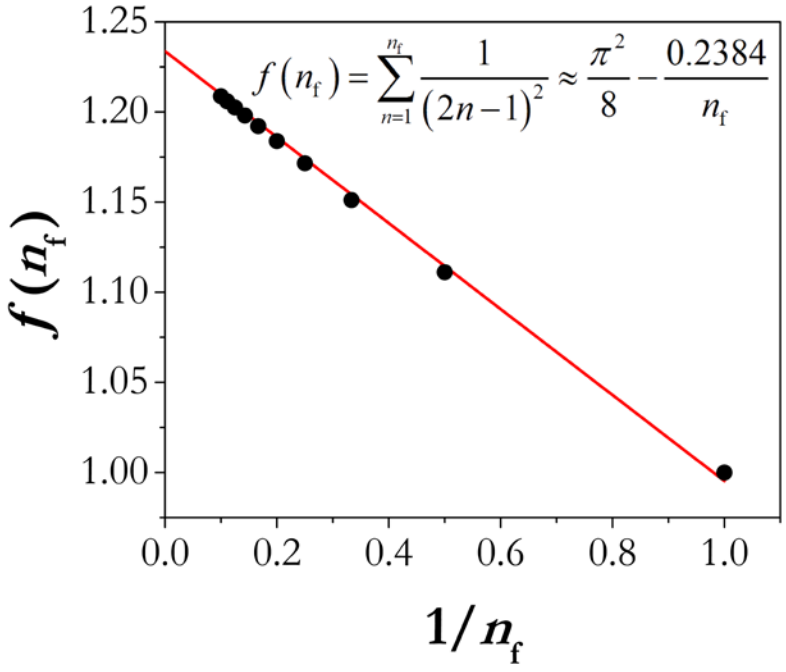

Figure 4.7. Quasi-linear variation of function $f(n_f)$ with $1/n_f$.

Using these approximations, the expression for the surface energy is:

$$\gamma_{n_f} = \frac{\alpha}{2d} + \frac{\pi^2\beta}{16d^3 n_f} - \frac{\beta\zeta}{2d^3 n_f^2} \tag{4.8}$$

which represents a second-order polynomial on $1/n_f$. We use Eq. 4.8 to extrapolate the DFT-calculated surface energies to edges with higher numbers of concentric folds. **Figure 4.5d** shows the extrapolation of the surface energies, which range between ~3 J m^{-2} in the case of single-fold termination and ~1 J m^{-2} in the limit of infinite concentric folds.

Whereas our analysis indicates that there is a thermodynamic preference for multiple concentric folds, in practice there will be kinetic limitations preventing the formation of such complex structures. Our analysis here is consistent with the observation by Campos-Delgado *et al.*, that when the temperature of the heat treatment of graphene nanoribbons was increased, more multiple folds formed on the edges [42]. High temperatures are needed to provide the thermal energy to overcome the activation barriers for atomic reorganisation at the edges.

Finally, although the calculations above assume perfect graphitic structures without defects, it can be expected that the folded edges are more favourable regions for defect formation than the graphitic bulk. While it is computationally too expensive to evaluate defect formation energies in large supercells including defects at the quantum-mechanical level of calculation employed above, we have performed preliminary calculations of the segregation energies of Stone-Wales defects towards the folded edges, using the Dreiding force field [43] as implemented in the GULP code [44, 45]. We found that Stone-Wales defects at the folded edges are much more stable than at the bulk, by up to 3.4 eV in the highest-curvature folded edge (*i.e.* the one joining two consecutive layers, and diameter *a*) and by up to 1.4 eV in the folded edge with diameter 3*a*. These energy values are only approximate due to the inaccuracies involved in the force field, but they do illustrate that there will be a considerable driving force for defects to accumulate at the folded edges of graphite, which can be expected to be more reactive than the graphite basal planes.

4.3.3 Transformed graphite after the application of an electric field

Now I will discuss the structures formed by the application of an electric field to the closed-edge graphitic structures. The carbon collected from the graphite rods following passage of current contained some 'normal' graphite, but this was accompanied by many regions with a very different appearance. Typical transformed areas are shown in **Figure 4.8**. As can be seen, the outline of the structure in this area of the material is more irregular than in the fresh graphite, with many curved and unusually-shaped features. The carbon is frequently found to be decorated with short nanotubes or nanoparticles, and in some cases, nanotube-like structures are seamlessly connected to the larger regions. These nanotube-graphene junctions have been analysed in detail in Ref. [46].

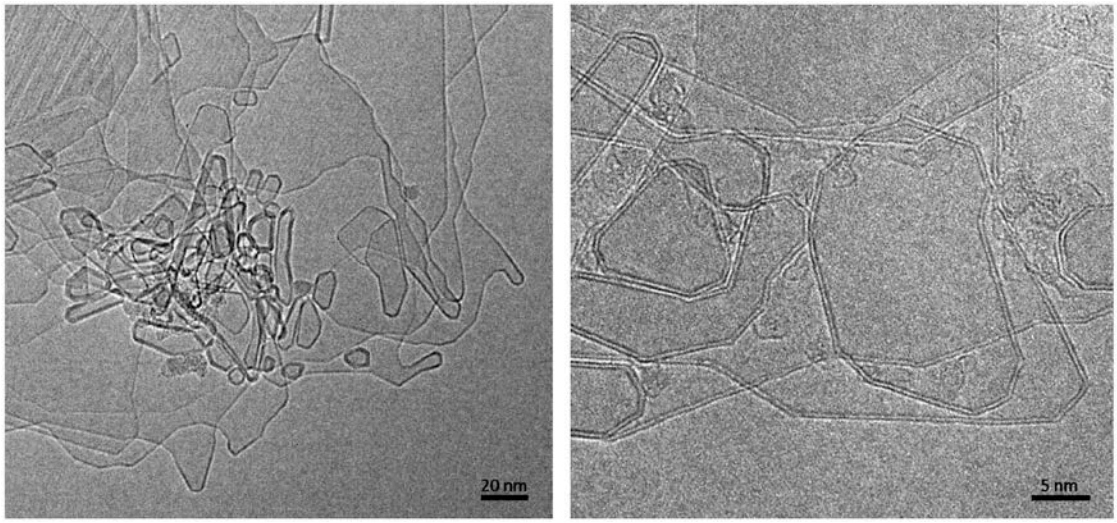

Figure 4.8. Micrographs showing transformed structures following passage of current through graphite.

In previous studies (*e.g.* Refs. [13] and [14]) it has been suggested that these structures are largely three-dimensional and hollow, but more recent studies using high-tilt TEM imaging have shown that many of the larger structures are flat, with a separation of the graphene layers along the edges of the crystals. **Figure 4.9** shows a tilt series of some typical structures. In **Figure 4.9a**, one of the structures can be seen edge-on, with a

separated region clearly visible at the tip, whereas in **Figure 4.9b** and **c**, the expanded regions can be seen along the margins of the particles.

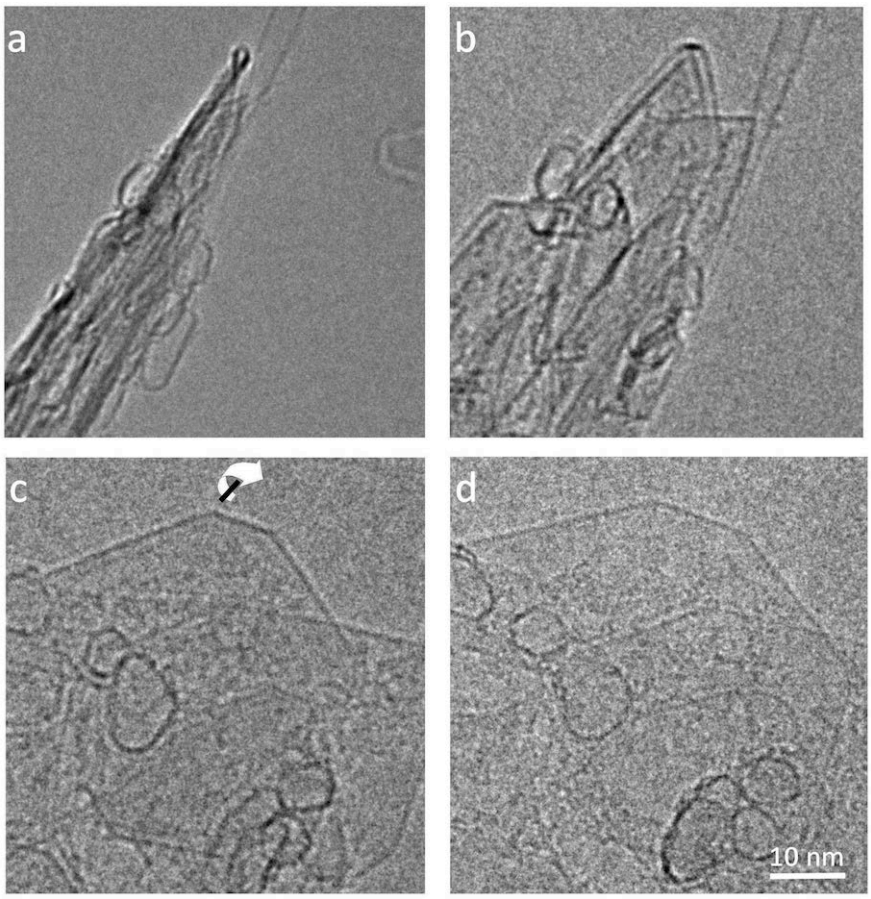

Figure 4.9. TEM images of transformed graphite at tilt values of a) -70º, b) -60º, c) -30º and d) +40º. Arrow in c) shows directions of tilt.

Another tilted region, with the expanded region along the edge indicated by arrows, is shown in **Figure 4.10**. Some higher magnification TEM images of the separated edges are shown in **Figure 4.11**. In the high-resolution images in **Figure 4.11b** and **c**, it can be seen that the separated structures are bilayer loops attached to four layers of graphene.

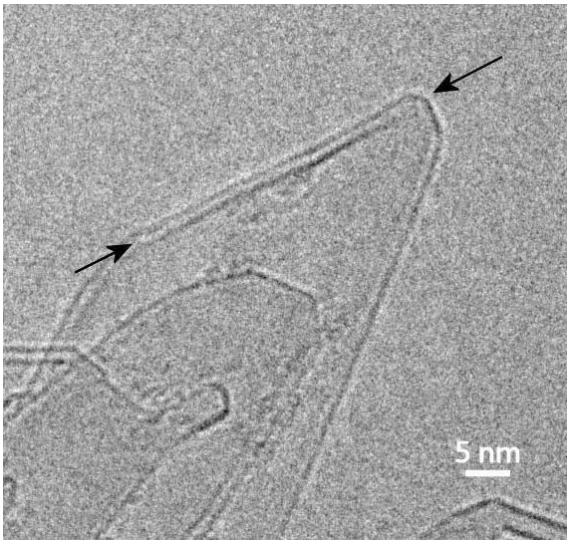

Figure 4.10. TEM image of tilted region in transformed graphite with arrows indicating expanded region along the edge.

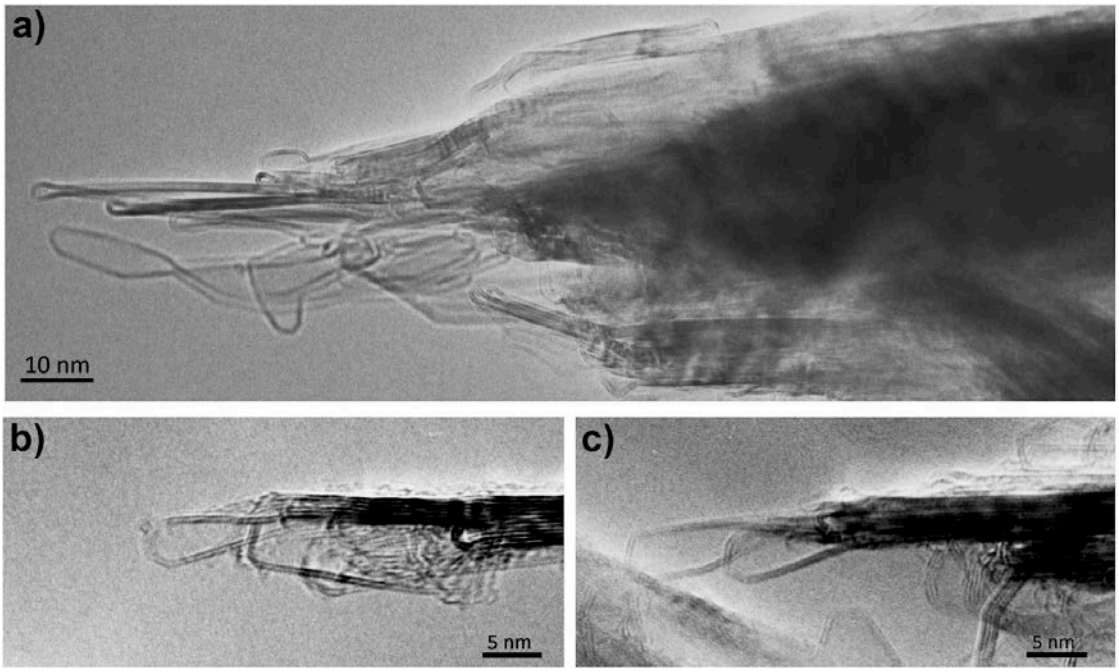

Figure 4.11. a) Intermediate magnification image, b) and c) higher-magnification images of separated layers, showing bilayer structure.

It should be noted that work by Campos-Delgado *et al.* [42] has shown that furnace annealing of graphite results in very different edge behaviour to annealing by Joule heating, *i.e.* heating by passage of a current. Furnace annealing produces edge closure, while Joule heating results in much more extensive structural transformations. The passage of a

current, or the presence of an electrostatic charge, clearly has a greater effect on the structure than that produced by simple heating.

In order to understand the effect of the electric field on folded graphitic edges, we have performed DFT calculations on a single folded graphene nanoribbon, applying an electric field either parallel or perpendicular to the graphene layers. Whereas in the experiment, the graphitic layers will have random orientations with respect to the electric field, in the simulations we are considering only two limit cases for the sake of simplicity. Single-point calculations, *i.e.* without geometry relaxation, show that electronic charge redistribution takes place upon the application of the field. When the field is applied parallel to the layers, charge accumulates at the edge. However, the resulting electrostatic repulsion is not enough to separate the folded edge. In fact, geometry relaxation under the parallel field leads to minimal structural change, even when a very strong field of 3 V $Å^{-1}$ is applied.

In contrast, when the electric field is applied perpendicular to the layer, a different behaviour is observed, than can explain the separation of the folded edge. In this case, the charge redistribution consists of electrons moving from one layer to the other, in the opposite direction to the electric field. For example, if we assume that the electric field is pointing upward, as in **Figure 4.12**, negative charge will accumulate in the bottom layer, while the top layer will have a net positive charge. The charge transfer will be opposed by same-charge repulsion within a layer, and by the fact that electrons need to occupy quantum states of higher energy. The induced charges of the carbon atoms, according to a Bader charge density partition analysis [47], increase with the magnitude of the electric field, and are in the range of 0.01 – 0.04 eV per atom (see **Figure 4.12a**). The net forces on the atoms (represented by the brown arrows in **Figure 4.12b**) tend to pull the oppositely charged layers apart.

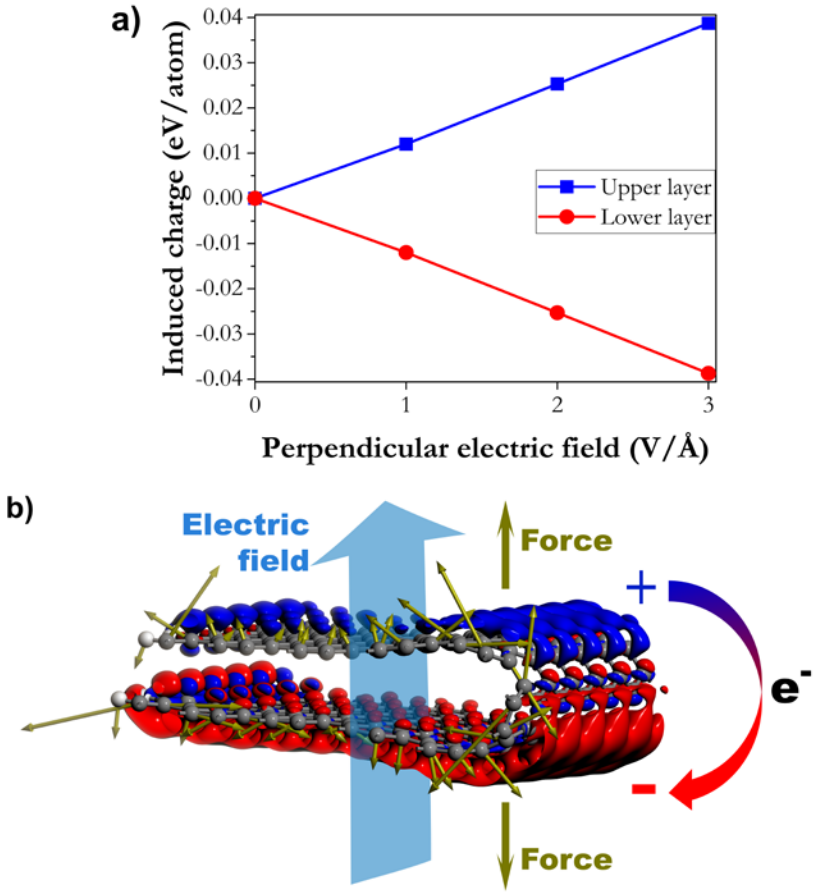

Figure 4.12. a) Average induced charges of atoms at the upper and lower layers as function of the magnitude of the electric field applied perpendicularly and b) charge density difference and atomic forces induced by a strong electric field in a folded nanoribbon (red and blue colours denote electron charge accumulation and depletion, respectively. The brown arrows represent the atomic forces. The example shown corresponds to an electric field of 3 V Å^{-1}).

Whether the folded edge expands completely or not depends on a delicate balance between the field-induced forces, the attractive dispersion forces, and the strain forces at the edge (which also tend to separate the loop). In our model nanoribbons, only the application of very strong fields (~3 V Å^{-1}) leads to loop separation upon geometry relaxation (**Figure 4.13**).

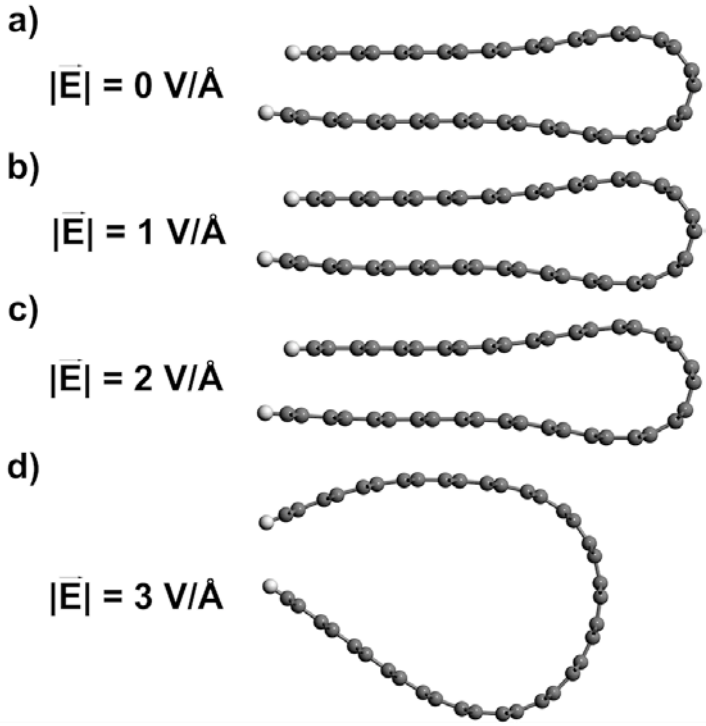

Figure 4.13. Relaxed geometries of the folded graphene ribbons in the presence of electric fields of different intensities.

However, the field strength required to separate the folded edges in real graphitic systems can be expected to be very different, since other factors, like temperature or the presence of defects, might play a role not accounted for in our nanoribbon model. For example, in the experiments described above in this section, the graphitic system is heated above 2000 K, so kinetic barriers preventing the expansion of the loop edge can be easily overcome. In contrast, our model is static and essentially represents the system at 0 K; therefore it is not surprising that an unphysically large electric field is required to reproduce an effect observed at much larger temperatures. Our calculations provide only qualitative insight into the behaviour of the closed edges in the presence of an electric field, but the proposed picture is physically reasonable and in good agreement with the experimental observation.

4.4 Conclusion

In this Chapter, I have presented a theoretical investigation of the folded edge structure of graphite, including an analysis of the thermodynamics of edge folding and the effect of an electric field. Because this work was carried out in collaboration with an experimentalist (Dr Peter Harris), the related experiments were also presented for clarity. My density functional theory calculations explain the preference for multiple concentric loops at the edges observed by transmission electron microscopy, and quantify the stability of different edge terminations as a function of the number of concentric loops.

Transmission electron microscopy images of the transformed structures obtained by the application of an electric field show that this could lead to the separation of the closed edges. A model is then proposed to explain this behaviour based on density functional theory calculations. The electric field leads to a charge redistribution resulting in layers with opposite charge, which are pulled apart by the electric field. Geometry relaxation of folded graphene nanoribbons in the presence of an electric field confirms the tendency to loop expansion.

This study contributes important insights into the properties of graphite closed edges, and their response to electric fields. The results will help to explain the effect of electric fields on the structure of graphitic carbons, and may have implications for understanding the growth of carbon nanotubes by arc-discharge.

4.5 References

1. Harris, P.J.F., *Transmission Electron Microscopy of Carbon: A Brief History*. C, 2018. **4**(1).
2. Buseck, P.R., H. Bo-Jun, and L.P. Keller, *Electron Microscope Investigation of the Structures of Annealed Carbons*. Energ. Fuel., 1987. **1**(1): p. 105-110.

3. Rotkin, S. and Y. Gogotsi, *Analysis of non-planar graphitic structures: from arched edge planes of graphite crystals to nanotubes.* Mater. Res. Innov., 2002. **5**(5): p. 191-200.

4. Liu, Z., Suenega, K., Harris, P. J. F., Iijima, S., *Open and Closed Edges of Graphene Layers.* Phys. Rev. Lett., 2009. **102**: p. 015501.

5. Acik, M. and Y.J. Chabal, *Nature of Graphene Edges: A Review.* Jpn. J. Appl. Phys., 2011. **50**(7R): p. 070101.

6. Zhang, X., J. Xin, and F. Ding, *The edges of graphene.* Nanoscale, 2013. **5**(7): p. 2556-2569.

7. Yan, J., et al., *Graphene homojunction: closed-edge bilayer graphene by pseudospin interaction.* Nanoscale, 2016. **8**(17): p. 9102-9106.

8. Huang, J.Y., et al., *In situ observation of graphene sublimation and multi-layer edge reconstructions.* Proceedings of the National Academy of Sciences, 2009. **106**(25): p. 10103.

9. Chopra, N.G., et al., *Fully collapsed carbon nanotubes.* Nature, 1995. **377**(6545): p. 135-138.

10. Machon, D., et al., *Perspective: High pressure transformations in nanomaterials and opportunities in material design.* Journal of Applied Physics, 2018. **124**(16): p. 160902.

11. Balima, F., et al., *Radial collapse of carbon nanotubes for conductivity optimized polymer composites.* Carbon, 2016. **106**: p. 64-73.

12. Harris, P.J.F., *Ultrathin graphitic structures and carbon nanotubes in a purified synthetic graphite.* J. Phys. Condens. Matter., 2009. **21**(35): p. 355009.

13. Harris, P.J.F., *Hollow structures with bilayer graphene walls.* Carbon, 2012. **50**(9): p. 3195-3199.

14. Harris, P.J.F., et al., *Bilayer graphene formed by passage of current through graphite: evidence for a three-dimensional structure.* Nanotechnology, 2014. **25**(46): p. 465601.

15. Harris, P.J.F., I. Suarez-Martinez, and N.A. Marks, *The structure of junctions between carbon nanotubes and graphene shells.* Nanoscale, 2016. **8**(45): p. 18849-18854.

16. Jia, X., et al., *Controlled Formation of Sharp Zigzag and Armchair Edges in Graphitic Nanoribbons.* Science, 2009. **323**(5922): p. 1701-1705.

17. Qi, L., et al., *In situ observations of the nucleation and growth of atomically sharp graphene bilayer edges.* Carbon, 2010. **48**(8): p. 2354-2360.

18. Girifalco, L.A. and M. Hodak, *Van der Waals binding energies in graphitic structures.* Physical Review B, 2002. **65**(12): p. 125404.

19. Barreiro, A., et al., *Graphene at High Bias: Cracking, Layer by Layer Sublimation, and Fusing.* Nano Letters, 2012. **12**(4): p. 1873-1878.

20. Harris, P.J.F., *Engineering carbon materials with electricity.* Carbon, 2017. **122**: p. 504-513.

21. Alyobi, M.M.M., et al., *Modifying the electrical properties of graphene by reversible point-ripple formation.* Carbon, 2019. **143**: p. 762-768.

22. Lopez-Bezanilla, A., et al., *Geometric and Electronic Structure of Closed Graphene Edges.* J. Phys. Chem. Lett., 2012. **3**(15): p. 2097-2102.

23. Ugarte, D., *Curling and closure of graphitic networks under electron-beam irradiation.* Nature, 1992. **359**(6397): p. 707-709.

24. Kresse, G., Furthmüller, J., *Efficiency of ab-initio total energy calculations for metals and semiconductors using a plane-wave basis set.* Comput. Mater. Sci., 1996. **6**: p. 15 - 50.

25. Kresse, G., Furthmüller, J., *Efficient iterative schemes for ab initio total-energy calculations using a plane-wave basis set.* Phys. Rev. B: Condens. Matter Mater. Phys., 1996. **54**(16): p. 11169 - 11186.

26. Berland, K., et al., *van der Waals forces in density functional theory: a review of the vdW-DF method.* Reports on Progress in Physics, 2015. **78**(6): p. 066501.

27. Klimeš, J., D.R. Bowler, and A. Michaelides, *Chemical accuracy for the van der Waals density functional.* J. Phys. Condens. Matter., 2010. **22**(2): p. 022201.

28. Klimeš, J., D.R. Bowler, and A. Michaelides, *Van der Waals density functionals applied to solids.* Physical Review B, 2011. **83**(19): p. 195131.

29. Ontaneda, J., et al., *Origin of the monolayer Raman signature in hexagonal boron nitride: a first-principles analysis.* Journal of Physics: Condensed Matter, 2018. **30**(18): p. 185701.

30. Pykal, M., et al., *Modelling of graphene functionalization.* Phys. Chem. Chem. Phys., 2016. **18**(9): p. 6351-6372.

31. Wu, X., et al., *Towards extending the applicability of density functional theory to weakly bound systems.* The Journal of Chemical Physics, 2001. **115**(19): p. 8748-8757.

32. Klimeš, J. and A. Michaelides, *Perspective: Advances and challenges in treating van der Waals dispersion forces in density functional theory.* The Journal of Chemical Physics, 2012. **137**(12): p. 120901.

33. Grimme, S., *Semiempirical GGA-type density functional constructed with a long-range dispersion correction.* Journal of Computational Chemistry, 2006. **27**(15): p. 1787-1799.

34. Grimme, S., et al., *A consistent and accurate ab initio parametrization of density functional dispersion correction (DFT-D) for the 94 elements H-Pu.* The Journal of Chemical Physics, 2010. **132**(15): p. 154104.

35. Torres-Dias, A.C., et al., *From mesoscale to nanoscale mechanics in single-wall carbon nanotubes.* Carbon, 2017. **123**: p. 145-150.

36. Blöchl, P.E., *Projector augmented-wave method.* Phys. Rev. B, 1994. **50**(24): p. 17953-17979.

37. Kresse, G. and D. Joubert, *From ultrasoft pseudopotentials to the projector augmented-wave method.* Phys. Rev. B, 1999. **59**(3): p. 1758-1775.

38. Santos, E.J.G. and E. Kaxiras, *Electric-Field Dependence of the Effective Dielectric Constant in Graphene.* Nano Lett., 2013. **13**(3): p. 898-902.

39. Zhan, D., Liu, L., Xu, Y. N., Ni, Z. H., Yan, J. X., Zhao, C., Shen, Z. X., *Low temperature edge dynamics of AB-stacked bilayer graphene: Naturally favored closed zigzag edges.* Sci. Rep., 2011. **1**(12): p. 1-5.

40. Xin, Z., Z. Jianjun, and O.-Y. Zhong-can, *Strain energy and Young's modulus of single-wall carbon nanotubes calculated from electronic energy-band theory.* Phys. Rev. B, 2000. **62**(20): p. 13692-13696.

41. Robertson, D.H., D.W. Brenner, and J.W. Mintmire, *Energetics of nanoscale graphitic tubules.* Physical Review B, 1992. **45**(21): p. 12592-12595.

42. Campos-Delgado, J., et al., *Thermal stability studies of CVD-grown graphene nanoribbons: Defect annealing and loop formation.* Chem. Phys. Lett., 2009. **469**(1): p. 177-182.

43. Mayo, S.L., Olafson, B. D., Goddard III, W. A., *DREIDING: A Generic Force Field for Molecular Simulations.* J. Phys. Chem., 1990. **94**: p. 8897 - 8909.

44. Gale, J.D., *GULP: A computer program for the symmetry-adapted simulation of solids.* J. Chem. Soc., Faraday Trans., 1997. **93**(4): p. 629 - 637.

45. Gale, J.D., Rohl, A. L., *The General Utility Lattice Program (GULP).* Mol. Simul., 2003. **29**(5): p. 291 - 341.

46. Harris, P.J.F., *Structural transformation of natural graphite by passage of an electric current.* Carbon, 2016. **107**: p. 132-137.

47. Bader, R.F.W., *Atoms in Molecules: A Quantum Theory*. 1994: Oxford University Press.

5 Iron species on nitrogen-doped graphitic nanostructures

In this Chapter, I will investigate graphitic nanostructures doped with nitrogen and in contact with iron species, which are of interest for their carbon dioxide reduction activity. First, we will consider iron oxyhydroxide nanostructures (ferrihydrite-like structures) in interaction with nitrogen-doped graphitic edges. By means of operando Q-EXAFS (quick-scanning extended X-ray absorption fine structure) carried out by experimental collaborators at the core X-ray absorption spectroscopy beamline of Diamond Light Source, it was possible to reveal the reversible redox chemistry of iron oxyhydroxide nanostructures on nitrogen-doped carbon in low concentration bicarbonate solution. Some experimental results (not obtained by me) will be discussed here in order to understand the theoretical contribution to corroborate the role of pyridinic N dopants in stabilising the interface between graphite and the iron oxo-hydroxide particles. This study has been published already (*Nat. Commun.*, 2018, 9, 935) and my featured image was selected by the Nature Research Chemistry Community and published in a 'Behind the Paper' post: http://go.nature.com/2oNe4jP.

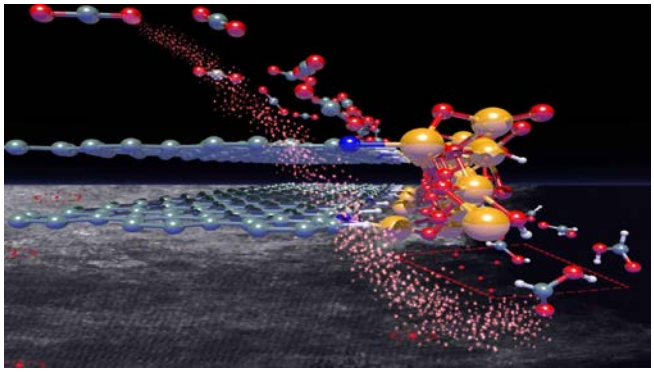

Image caption: scanning transmission electron micrograph (ePSIC facility) and model of the ferrihydrite decorating the graphite edges. Colour code: Fe = orange, C = grey, O = red and N = blue.

Second, we will investigate the structural and electronic properties of Fe, N co-doped graphene, where Fe species could act as "single-atom" catalysts. It is known that the electrocatalytic function of Fe species supported on N-doped graphitic C has been correlated to many structural features characterising these materials, including the functionalised edge terminations of graphene layers, Fe-N_4 ensembles and other structural point defects. With particular concern to coordinated single metal atomic species, little is known about how these species are formed during the synthesis as well as their stability in their application as a catalyst. This study is part of an ongoing collaboration (still unpublished) with the experimental group of Dr Rosa Arrigo, where we will attempt to explain from a theoretical view, the nature of defects (active sites) on N-doped graphene can act as potential anchoring sites for Fe single atom.

5.1 Introduction

One of the current grand challenges in chemical science is the conversion of recycled CO_2 to chemicals using renewable energy [1, 2]. As a consequence, the electrochemical CO_2 reduction reaction (CO_2RR) over different electrodes [3] is increasingly investigated, with the main hurdle being the formation of products with more than one carbon atom. Copper has shown an incomparable efficiency to form hydrocarbons [4, 5], but despite this, a poor stability, selectivity and high overpotentials are limiting factors. The opportunity to facilitate one selective path amongst the others relies on the possibility to kinetically control the energetics of adsorbed reaction intermediates [6], on a specific surface structure. This demands new ideas in catalyst design attainable through a molecular level understanding of the reaction mechanism [5, 6].

With respect to the selectivity issue, molecular catalysis can be product-specific and highly efficient, however redox processes are limited to the transfer of only a few electrons, thereby leading to products of lower technological interest such as CO.

Recently, it was shown that the immobilisation of molecular species such as Co porphyrins on graphite and graphene opens up opportunities for multistep reduction products [6]. Also, it has been demonstrated the synthesis of acetic acid via CO_2RR over Cu on carbon nanotubes (Cu/CNTs) electrodes [7].

Nitrogen species in carbon have been also reported to convert CO_2 to C1 products, such as CO [8, 9]. Compared to metal-free nanocarbons, C supported metal nanoparticles allow improving performances and lowering CO_2RR overpotentials [10], but the competing hydrogen evolution reaction (HER) is also favoured.

In the first part of this chapter, we investigate Fe oxyhydroxide nanostructures supported on N-doped graphitic structures, which have been shown by our experimental collaborators to display CO_2RR activity. It has been evidenced outstanding performance of ferrihydrite-like clusters on N-doped carbon (N-C) with a total CO_2RR Faraday efficiency above 97% and high selectivity to acetic acid at very low potential. This study reveals the reversible redox chemistry of ferrihydrite nanostructures on N-C in low concentration bicarbonate solution, characterised by the formation of Fe(II) species at potentials relevant for CO_2RR, whereas at more negative potentials those species turn into Fe^0. In contrast, there is no significant formation of Fe(II) species in the ferrihydrite supported on O-containing carbon in this voltage range, and the only structural modification observed is the reduction of some of the ferrihydrite cluster to Fe^0.

The H_2 reduction is indeed correlated to the transformation of Fe(III) into Fe^0. Via a combination of ambient pressure soft X-ray photoelectron spectroscopy (XPS) done by our experimental collaborators and our density functional theory (DFT) simulations, we prove that a chemical interaction occurs between Fe sites of ferrihydrite and the pyridine N species on the carbon surface. As a consequence of the favourable Fe-N interaction, Fe species, initially present as single atoms or clusters decorating the N-functionalised edges of the graphitic planes, are stabilised as Fe(II) species at a potential

consistent with the carbonation of ferrihydrite and the formation of a Fe(II)Fe(III) mixed compound [11]. This potential range coincides with the highest Faraday efficiency to CO_2RR products.

On the other hand, the nature of defects in graphitic materials has been extensively described, including a recent comprehensive review [12] on the influence of the carbon defects chemistry characterising various forms of carbon materials in tailoring the reactivity and selectivity of metal nanoparticles. In order to have a wider perspective of the effects of Fe species in graphitic systems in this Chapter, the second part of this section will focus on the structural analysis and adsorption of Fe on pristine graphene as adatom and on free- and N-doped defective graphene. These results will enable us to understand the nature of the active sites within graphitic structures when Fe atoms are adsorbed.

5.2 Computational Methods

The Vienna *Ab Initio* Simulation Package (VASP) [13, 14] was used to carry out quantum mechanical calculations within the Kohn-Sham implementation of the DFT. The Perdew-Burke-Ernzerhof (PBE) [15, 16] version of the generalised gradient approximation (GGA) was employed as the exchange-correlation potential. A Hubbard-type correction was applied to Fe 3*d* orbitals following the GGA+U formulation by Dudarev *et al.* [17], where a single parameter U_{eff} determines the strength of the correction.

The GGA+U approach penalises the *d* orbital hybridisation with the ligands, thus opposing the GGA tendency to over-delocalise orbitals. Previous work has shown that U_{eff} = 4.0 eV leads to optimal results in the description of the electronic structures of iron oxides [18-20]. The interaction of the valence electrons with the core was modelled using projector augmented wave (PAW) potentials, where levels up to 1 *s* in C, N and O atoms and up to 3*d* in Fe atoms were kept frozen at the atomic reference states.

The number of planewaves in the basis set is controlled by the cutoff energy, which in calculations was E_{cut} = 520 eV, 30% above the standard value for the set of PAW potentials. Integrations in the reciprocal space were performed using a fine grid of Γ-centred *k*-points with a maximum separation of 0.01 $Å^{-1}$ in the reciprocal space. All precision parameters were tested for convergence of the total energy to within 1 meV $atom^{-1}$. Spin polarisation was allowed in the simulations of iron-based systems, and the magnetic moments were calculated in ferromagnetic configurations for simplicity.

5.3 Results

5.3.1 Fe oxyhydroxide nanostructures supported on N-doped graphitic

In order to investigate the interaction between the graphitic edge (with and without N dopants) and the ferrihydrite-like nanostructure, an idealised structural model was created to perform DFT simulations (**Figure 5.1**). In the absence of detailed experimental information on the structure, a significant effort was put into creating a plausible structural model, based on the following criteria.

First, the iron oxyhydroxide nanostructure is assumed to have the stoichiometry and local structure of bulk ferrihydrite (Fe_5O_8H).

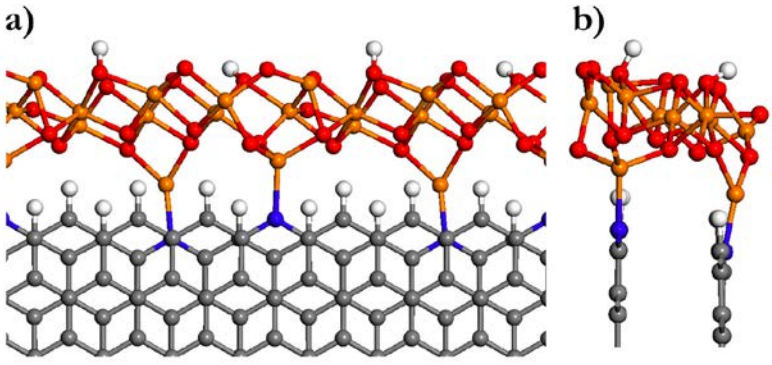

Figure 5.1. Model of the F*h*-FeOOH/N-C interfase. a) Top and b) lateral views of the DFT+U-relaxed geometry of ferrihydrite nanostructures decorating the N-doped graphitic zigzag edges. Colour code: C = grey, H = white, N = blue, Fe = orange and O = red.

The model is cut out from the bulk crystal structure reported by Pinney *et al.* [21] and is made periodic in one dimension to interface with the graphitic edge. The ferrihydrite nanostructure is assumed to be in close contact with graphite, decorating its zigzag edge, which is represented in our model by a hydrogen-terminated one-dimensional nanoribbon with two AB-stacked layers. The edge decoration feature is consistent with the high-angle annular dark field scanning transmission electron micrograph (HAADF-STEM) images for the Fe/N-C presented in **Figure 5.2**.

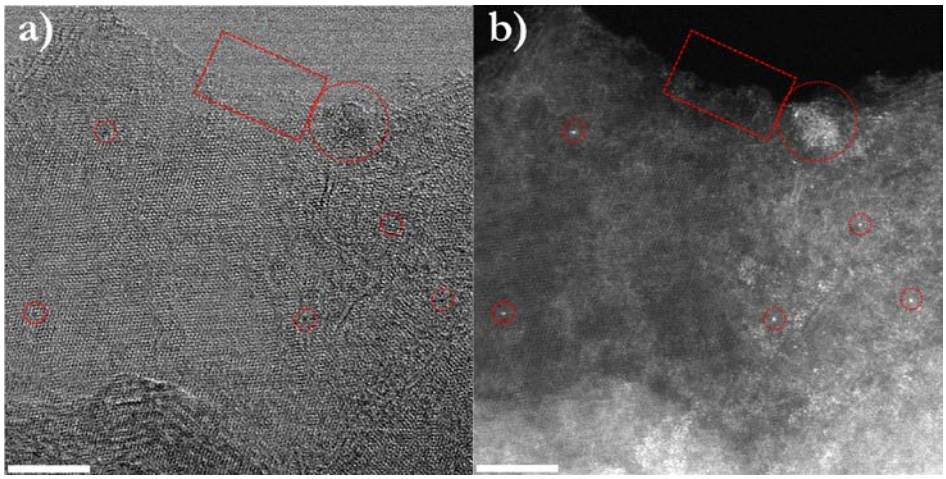

Figure 5.2. Nanostructure of Fe/N-C sample. a) Representative bright field and b) HAADF-STEM micrographs of sample Fe/N-C (scale bar 5 nm). The brightest spots in the HAADF-STEM image are Fe atoms. Several morphologies are identified: nanoparticles (circle); polyatomic species (rectangle) and single atoms (small circle).

Second, along the [001] direction of the crystal, the ferrihydrite nanostructure is terminated by hydroxyl groups on one side (facing the vacuum gap) and by Fe cations on the other side, in such a way that they interact directly with the graphitic edge, as suggested by the experimental results. Along the periodic direction, we chose a supercell with eight C atoms at the edge, which minimises the strain of the ferrihydrite layer with respect to its bulk cell parameters (because highly-strained structures would be thermodynamically forbidden). Therefore, although our model does not come from direct structural determination, it is based on the available experimental information and thermodynamic considerations.

We now discuss the strength of the interactions at the interface. In the absence of N dopants, the interaction energy between the graphitic edge and the ferrihydrite nanostructure is calculated to be -1.1 eV for the supercell (with respect to the free edge and the unstrained ferrihydrite 1D nanostructure). However, when terminal C-H species at the edge are substituted by pyridinic N species, the interaction energy becomes significantly more negative (-1.9 eV) as the result of the formation of two N-Fe bonds per supercell. Energy minimisation leads to N-Fe bond lengths of 2.0 Å and 2.1 Å, which are similar to Fe-N (pyridine) bond distances reported in the literature. It is clear then that the presence of pyridinic nitrogen at the carbon edge stabilises the C/ferrihydrite interface, by ~0.4 eV per N-Fe bond formed. The formation of the chemical bond is accompanied by charge transfer from the N atom to the Fe ion, whose Bader charge [22] decreases from 1.62 a.u. to 1.26 a.u. indicating a partial reduction. This is consistent with the Fe L near edge X-ray absorption fine structure (NEXAFS) spectrum of the Fe/N-C sample in **Figure 5.3**, which clearly indicates the presence of reduced Fe(II) sites as compared with the N-free Fe/O-C sample.

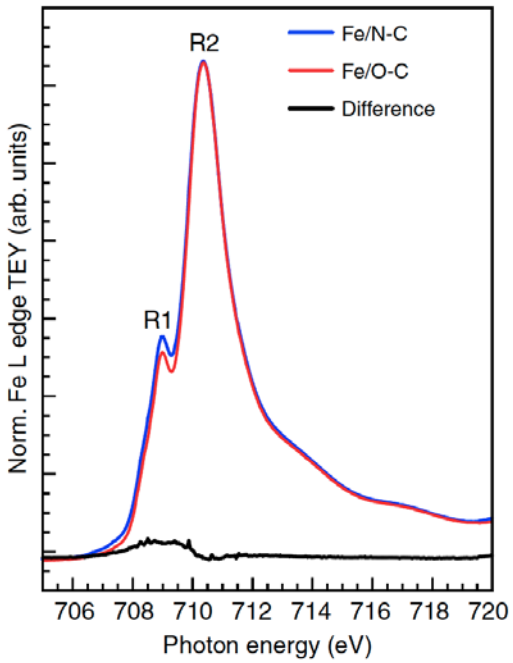

Figure 5.3. Fe L edge NEXAFS spectrum of Fe/O-C (red line), Fe/N-C (blue line) and residual of the difference between the two spectra (black line).

We also tested the possibility of the formation of C-Fe bonds at the interface, via the removal of terminating hydrogen from the edge to the gas phase (on the form of H_2 molecules). However, this is not a favourable process as the formation of such interface, including the gas phases species, requires a large positive (5.4 eV) energy.

The main result of this work, from the theoretical part, was the creation of a model than can account for available experimental information from microscopy and NEXAFS. We hope that this model leads to further studies of the reaction mechanism using this promising electrocatalyst.

5.3.2 Single-atom Fe sites in graphitic catalysts: interaction with N dopants and defects

Moving on now to the single Fe atom, we have considered three possible scenarios where Fe atoms could be adsorbed on graphitic structures: Fe atoms (adatoms) on pristine graphene, pure graphene with vacancies and N-doped defective graphene. Analysis of absorption energy (E_{ads}) between Fe atom and those carbon systems will provide us a preliminary step on our ongoing collaboration with experimentalists, showing us a perspective of the effect of Fe atoms and their stability among the graphitic structures described above.

For the interaction between Fe atoms and graphene (adatom), three different positions of Fe atom were considered as starting point which are standing on top of the centre of a C_6-ring, a C-C bond and a C atom (see **Figure 5.4**). Calculated E_{ads} of these positions showed values in order of magnitude of 10^{-2} eV, which means that the interaction is poor between Fe and graphene surface. However, it was found that an Fe atom standing on top of the centre a C_6-ring is the most stable position having an E_{ads} of -62.13 meV and also the calculated distance between them is the smallest one among all positions (1.99 Å).

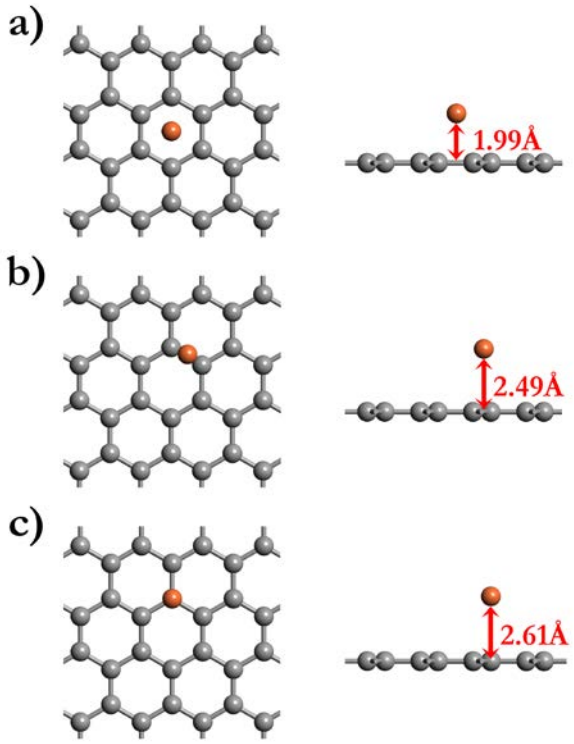

Figure 5.4. Positions and distances calculated between Fe atoms and pristine graphene: a) centre of the graphene rings, b) between a C-C bond and on top of a C atom. Colour code: C = grey and Fe = orange.

Regarding the adsorption of Fe on defective graphene, Fe atoms were embedded in graphene mono- and divacancies. In **Figure 5.5**, we can see that a single Fe atom substitutes missing carbon atom(s) and passivates the undercoordinated atoms of the native mono- and divacancy defects. After the calculation of E_{ads} for both defects, divacancy defect offer a more stable environment for the Fe atom compared with the monovacancy by ~1.53 eV. These results suggest that a four-coordinated setting should be suitable for Fe embedded atoms.

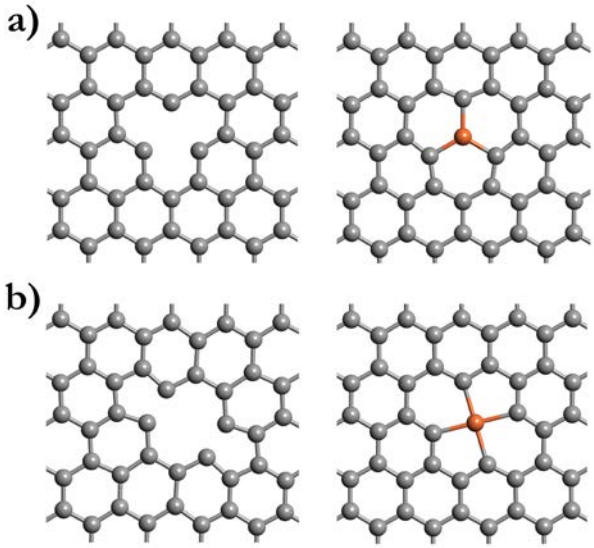

Figure 5.5. Geometries of a) mono- and b) divacancy defects in graphene with (right) and without (left) Fe embedded. Colour code: C = grey and Fe = orange.

Structural results obtained for the N-doped defective graphene after embedding the Fe atoms are similar as the ones obtained in pure defective graphene (**Figure 5.5**). In **Figure 5.6**, we can see that C atoms involved in the three- and four-coordination in both mono- and divacancy defects, respectively, are substituted with N atoms. Now, Fe atoms are anchored to the in-plane defects forming Fe-N_3 and Fe-N_4 ensembles. We found that absorption energy calculated for Fe-N_3 species do not show any enhancement compared with the one calculated for the analogous system in pure defective graphene, which adsorption is weaker (-1.15 eV). However, Fe-N_4 showed the strongest adsorption among all of the configurations explained above (-6.07 eV). This means that the stability is highly improved if a Fe atom is anchored in a four-coordinated N-doped vacancy in graphene. When the Fe atom is embedded in this ensemble, it is evident that we are dealing with a porphyrin-like structure (see **Figure 5.6b**) so that could be the reason of the great stability of this kind of structure.

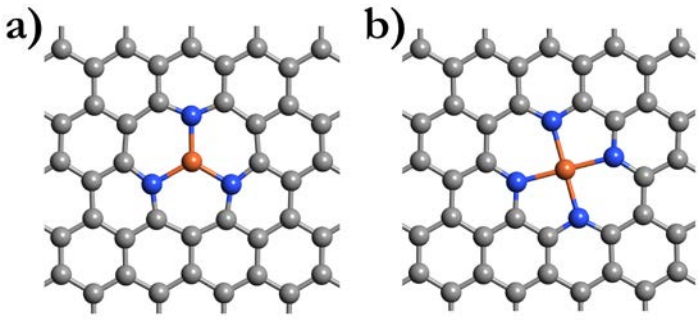

Figure 5.6. Geometries of a) Fe-N_3 and b) Fe-N_4 ensembles in graphene. Colour code: C = grey, N = blue and Fe = orange.

Table 5.1 shows a summary of the E_{ads} values for the three scenarios for Fe atoms: adatoms on pristine graphene, graphene with vacancies and N-doped defective graphene.

Table 5.1. Adsorption energies (E_{ads}) calculated for single-atom Fe sites in graphitic catalysts.

	Fe site	E_{ads} (eV)
Adatom	C_6-ring	-0.062
	C atom	-0.056
	C-C bond	0.082
Defective graphene	Divacancy	-3.772
	Monovacancy	-2.236
N-doped defective graphene	Fe-N_4	-6.074
	Fe-N_3	-1.148

5.4 Conclusion

Few relevant species for C-C coupling are an ensemble of chemically interacting (bi)carbonate-bearing Fe(II) species and N atoms, the latter one also capable of chemisorbing CO_2-related species. These results clearly indicate that the carbon surface chemistry influences significantly the Fe redox chemistry with strong impact on the catalytic performance. N dopants on carbon have a double effect: not only they coordinate CO_2-related species, but they also stabilise these Fe(II) species hindering their further reduction, thus inhibiting HER.

Our theoretical investigation, based on DFT+U method, of the interaction energy between the graphitic edge and the ferrihydrite nanostructure indicates that the presence of pyridinic nitrogen at the carbon edge stabilises the C/ferrihydrite interface. Also, the charge transfer obtained from the N atom to the Fe ion, which indicates a partial reduction, demonstrates the presence of reduced Fe(II) sites. This analysis corroborates the role of pyridinic N dopants in stabilising the interface between graphite and the iron oxo-hydroxide particles.

Also, our investigation of the adsorption of Fe single atoms through a vast set of graphitic models, showed us that when N dopants are present the stability is enhanced in some cases, such as in Fe-N_4 ensembles (porphyrin-like structures).

The models presented in this chapter will be useful in further investigation of the catalytic mechanisms of CO_2 reduction using Fe,N-doped graphitic nanostructure electrocatalysts.

5.5 References

1. Beller, M., G. Centi, and L. Sun, *Chemistry Future: Priorities and Opportunities from the Sustainability Perspective.* ChemSusChem, 2017. **10**(1): p. 6-13.
2. Perathoner, S. and G. Centi, *CO_2 Recycling: A Key Strategy to Introduce Green Energy in the Chemical Production Chain.* ChemSusChem, 2014. **7**(5): p. 1274-1282.
3. Lu, Q. and F. Jiao, *Electrochemical CO_2 reduction: Electrocatalyst, reaction mechanism, and process engineering.* Nano Energy, 2016. **29**: p. 439-456.
4. Hori, Y., K. Kikuchi, and S. Suzuki, *Production of CO and CH_4 in electrochemical reduction of CO_2 at metal electrodes in aqueous hydrogencarbonate solution.* Chemistry Letters, 1985. **14**(11): p. 1695-1698.
5. Mistry, H., et al., *Highly selective plasma-activated copper catalysts for carbon dioxide reduction to ethylene.* Nature Communications, 2016. **7**(1): p. 12123.

6. Shen, J., et al., *DFT Study on the Mechanism of the Electrochemical Reduction of CO_2 Catalyzed by Cobalt Porphyrins.* The Journal of Physical Chemistry C, 2016. **120**(29): p. 15714-15721.

7. Genovese, C., et al., *Mechanism of C–C bond formation in the electrocatalytic reduction of CO_2 to acetic acid. A challenging reaction to use renewable energy with chemistry.* Green Chemistry, 2017. **19**(10): p. 2406-2415.

8. Zhang, S., et al., *Polyethylenimine-Enhanced Electrocatalytic Reduction of CO_2 to Formate at Nitrogen-Doped Carbon Nanomaterials.* Journal of the American Chemical Society, 2014. **136**(22): p. 7845-7848.

9. Wu, J., et al., *Achieving Highly Efficient, Selective, and Stable CO_2 Reduction on Nitrogen-Doped Carbon Nanotubes.* ACS Nano, 2015. **9**(5): p. 5364-5371.

10. Su, D.S., S. Perathoner, and G. Centi, *Nanocarbons for the Development of Advanced Catalysts.* Chemical Reviews, 2013. **113**(8): p. 5782-5816.

11. Grivé, M., L. Duro, and J. Bruno, *Fe(III) mobilisation by carbonate in low temperature environments: Study of the solubility of ferrihydrite in carbonate media and the formation of Fe(III) carbonate complexes.* Applied Geochemistry, 2014. **49**: p. 57-67.

12. Machado, B.F. and P. Serp, *Graphene-based materials for catalysis.* Catalysis Science & Technology, 2012. **2**(1): p. 54-75.

13. Kresse, G., Furthmüller, J., *Efficiency of ab-initio total energy calculations for metals and semiconductors using a plane-wave basis set.* Comput. Mater. Sci., 1996. **6**: p. 15 - 50.

14. Kresse, G., Furthmüller, J., *Efficient iterative schemes for ab initio total-energy calculations using a plane-wave basis set.* Phys. Rev. B: Condens. Matter Mater. Phys., 1996. **54**(16): p. 11169 - 11186.

15. Perdew, J.P., K. Burke, and M. Ernzerhof, *Generalized Gradient Approximation Made Simple.* Physical Review Letters, 1996. **77**(18): p. 3865-3868.

16. Perdew, J.P., K. Burke, and M. Ernzerhof, *Generalized Gradient Approximation Made Simple [Phys. Rev. Lett. 77, 3865 (1996)]*. Physical Review Letters, 1997. **78**(7): p. 1396-1396.

17. Dudarev, S.L., et al., *Electron-energy-loss spectra and the structural stability of nickel oxide: An LSDA+U study*. Physical Review B, 1998. **57**(3): p. 1505-1509.

18. Grau-Crespo, R., et al., *Electronic structure and magnetic coupling in $FeSbO_4$: A DFT study using hybrid functionals and GGA+U methods*. Physical Review B, 2006. **73**(3): p. 035116.

19. Santos-Carballal, D., et al., *A DFT study of the structures, stabilities and redox behaviour of the major surfaces of magnetite Fe_3O_4*. Physical Chemistry Chemical Physics, 2014. **16**(39): p. 21082-21097.

20. Wang, L., T. Maxisch, and G. Ceder, *Oxidation energies of transition metal oxides within the GGA+U framework*. Physical Review B, 2006. **73**(19): p. 195107.

21. Pinney, N., et al., *Density Functional Theory Study of Ferrihydrite and Related Fe-Oxyhydroxides*. Chemistry of Materials, 2009. **21**(24): p. 5727-5742.

22. Tang, W., E. Sanville, and G. Henkelman, *A grid-based Bader analysis algorithm without lattice bias*. Journal of Physics: Condensed Matter, 2009. **21**(8): p. 084204.

6 Band structures of periodic porphyrin nanostructures

Recent progress in the synthesis of π-conjugated porphyrin arrays of different shapes and dimensionalities is the motivation to examine the band structures of infinite (periodic) porphyrin nanostructures. In this Chapter, screened hybrid density functional theory simulations and Wannier function interpolation were used to obtain accurate band structures of linear chains, 2D nanosheets and nanotubes made of zinc porphyrins. Porphyrin units are connected by butadiyne (C4) or ethyne (C2) linkers or "fused" (C0), *i.e.* with no linker. The electronic properties exhibit strong variations with the number of linking carbon atoms (C0/C2/C4). For example, all C0 nanostructures exhibit gapless or metallic band structures, whereas band gaps open for the C2 or C4 structures. The reciprocal space point at which the gaps are observed also show fluctuations with the length of the linkers. Here I will discuss the evolution of the electronic structure of finite porphyrin tubes made of a few stacked six-porphyrin rings toward the behaviour of the infinite nanotube. Our results suggest approaches for engineering porphyrin-based nanostructures to achieve target electronic properties. This section has been published (*J. Phys. Chem. C*, 2018, 122, 23790-23798).

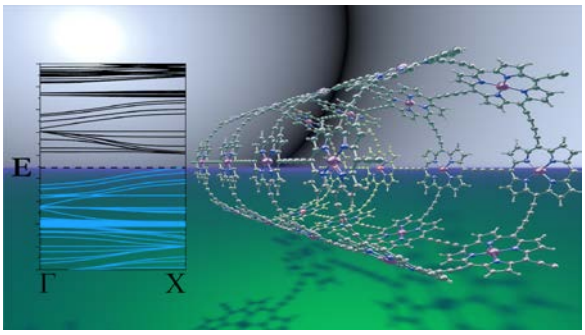

6.1 Introduction

Many natural light-harvesting systems are made of cyclic arrays of chlorophyll units [1]. One approach to study the energy and electron transfer processes in natural photosynthesis is based on the use of artificial model systems consisting of porphyrin arrays, which mimic the natural systems [2]. The geometry and dimensionality of such arrays strongly affect the efficiency and rate of photophysical processes. The investigation of porphyrin arrays is also interesting for potential technological applications. For example, large porphyrins arrays attached to semiconductors such as TiO_2 can lead to highly efficient dye-sensitised solar cells [3], and porphyrin-based molecular wires are being explored in the context of single-molecule electronics [4-8].

A wide range of porphyrin arrays with different dimensionalities have been synthesised and characterised. Linear chains where porphyrin units are linked via butadiyne (C4) or ethyne (C2) or completely fused (C0) are well studied due to their interesting optical and charge transport properties [9-14]. In particular, C0-linked porphyrin chains are known to exhibit very low optical excitation gaps which rapidly decrease as the chains become longer, leading to their very high conductance between metal electrodes [11]. Fused (C0) tetrameric porphyrin "sheets" have been synthesised [15], and the corresponding limit of a 2D crystal, with vanadium at the porphyrin centres, has been studied theoretically in terms of electronic and magnetic behaviour [16]. Cyclic arrays (nanorings) of 6 [17], 8 [18] or 12 [19] C4-linked porphyrin units (labelled *c*-**P6**, *c*-**P8** and *c*-**P12**, respectively) have been obtained by template-directed synthesis. It was observed that cyclic nanorings had lower optical excitation energies than the corresponding linear polymers. Recently, C2-linked nanorings have been synthesised, which exhibit stronger electronic coupling between the porphyrin units [20]. Covalently stacking two *c*-**P6** nanorings results in a "tube" (*t*-**P12**), whose optical absorption spectrum is red shifted with respect to the individual *c*-**P6**

nanorings, reflecting increased conjugation [21]. In the limit of many stacked nanorings, such structures can be seen as one-dimensional nanotubes with continuous electronic bands. Allec *et al.* theoretically considered the band structure of C4-linked infinite nanotubes, predicting large oscillations in their band gaps as a function of radius (or number of porphyrin units in the circumference) [22].

In this section, I theoretically investigate a range of periodic porphyrin nanostructures in order to predict their structural and electronic properties. Linear chains, 2D nanosheets and nanotubes made of Zn-centred porphyrins were considered and show that their properties exhibit strong variations with the number of carbon atoms (C0/C2/C4) linking the porphyrin units.

6.2 Methods

Simulations were carried out using the Vienna *ab initio* simulation package (VASP) code [23, 24], which solves the Schrödinger equation using three-dimensional periodic boundary conditions. Thus, the models are periodic even in the directions in which the nanostructures themselves are nonperiodic (**Figure 6.1**). Vacuum regions separating the nanostructures are always of at least 12 Å to minimise the interaction. The linear chains and the nanosheets were contained in an orthorhombic cell, whereas the periodic nanotubes were contained in a hexagonal cell to conserve the 6-fold rotation symmetry along the nanotube axis.

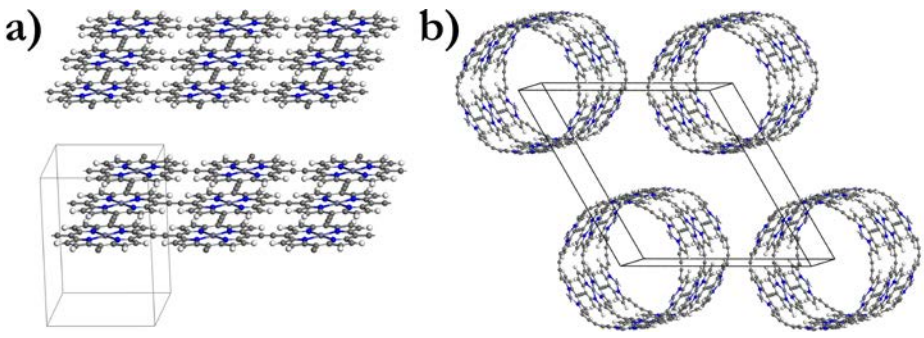

Figure 6.1. Periodic boundary conditions and unit cells employed in DFT simulations for a) nanosheets and b) nanotubes.

For geometry optimisations, the exchange and correlation potential was treated within the generalised gradient approximation (GGA) using a dispersion-corrected Perdew-Burke-Ernzerhof functional (PBE-D2) [25, 26]. In order to obtain accurate electronic structures, single-point calculations were carried out using the screened hybrid functional developed by Heyd, Scuseria and Ernzerhof (HSE06) [27, 28], since GGA functionals are known to underestimate the band gap (E_g) [29]. HSE06 calculations give E_g values in much closer agreement with experiment than GGA functionals [30, 31]. Although the HSE06 calculations were single-point only (no geometry optimisation), it has been tested (for simpler nanostructures) that the final electronic structures, based on the PBE-D2-optimised structures, were unaffected if the optimisation was also conducted at the HSE06 level. This is consistent with our previous work modelling the electronic structure of porphyrin-based metal-organic frameworks [32, 33]. Γ-centred grids of *k*-points were used for integrations in the reciprocal space. For the nanosheets a 6×6×1 mesh was used, while for the linear chains and the nanotubes a 1×1×6 mesh was considered. In order to obtain good-quality band structures and density of state curves, an interpolation procedure was used based on maximally localised Wannier functions as implemented in the Wannier90 code [34]. This is important because of the significant band dispersion in the investigated nanostructures and the huge computational cost of increasing the density of *k*-point grids in hybrid functional calculations.

The interaction of valence electrons with the atomic cores was modelled using project augmented wave (PAW) potentials, with core levels up to C 1*s*, N 1*s* and Zn 3*p* kept frozen in the atomic reference configurations. For the HSE06 band structure calculations, the kinetic energy cutoff of the plane-wave basis set expansion was set at 400 eV, the recommended value for the chosen PAW potentials. For the PBE-D2 geometry optimisations the cutoff energy was increased by 30% to avoid Pulay errors in the optimised cell parameters.

All of the electron energies have been reported with respect to the vacuum reference. As in other periodic DFT codes, the band energies in VASP are given with respect to an internal energy reference. Therefore, to obtain absolute energy levels it was necessary to evaluate the electrostatic potential in a pseudovacuum region given by an empty space within the simulation cell. This was chosen as a planar average in the vacuum gap between nanosheets and as a spherical average around a point of zero-potential gradient along the nanotube axis. The MacroDensity code was employed for this purpose [35].

6.3 Results and discussions

6.3.1 Porphyrin linear chains

Linear chains are the simplest case of porphyrin arrays. Flat models were built (**Figure 6.2**, left) consisting of periodic arrays of fused (C0), ethyne-linked (C2) or butadiyne-linked (C4) porphyrin units and optimised their geometric degrees of freedom. Resulting cell parameters and some relevant bond distances are listed in **Table 6.1**.

Table 6.1. Optimised geometric parameters of the porphyrin linear chains*.

	C0	**C2**	**C4**
d[C_{meso}–C_{meso}] (Å)	1.46	4.04	6.61
d[C_{β}–C_{β}] (Å)	1.43	4.04	6.59
d[Zn–N] (Å)	2.04	2.05	2.05
cell length a (Å)	8.42	11.00	13.57

* The parameter a is the lattice constant in the periodic dimension

The band structures of these 1D nanostructures are shown in **Figure 6.2** (right). In all cases, both the conduction and the valence bands of the polymers exhibit significant dispersion. Whereas the C2 and C4 chains exhibit band gaps of 1.0 eV and 1.1 eV, respectively, the C0 chain has a gap that is very close to zero. The top of the valence band

and the bottom of the conduction band are nearly degenerate at the X point of the Brillouin zone (energy difference between the bands of only ~9 meV, which is too small to be reliable given the precision of the calculations). Both bands are approximately linear when approaching the X point, resembling the behaviour of the valence and conduction bands of graphene near the Dirac point and suggesting that electrons and holes in this polymer will be nearly massless. These observations call for further theoretical and experimental investigation of electronic transport in this system. It has been experimentally observed that the HOMO-LUMO gap of fused (C0) porphyrin chains rapidly decreases with the number of porphyrins in the chain, and applications as molecular wires have been suggested [11, 12].

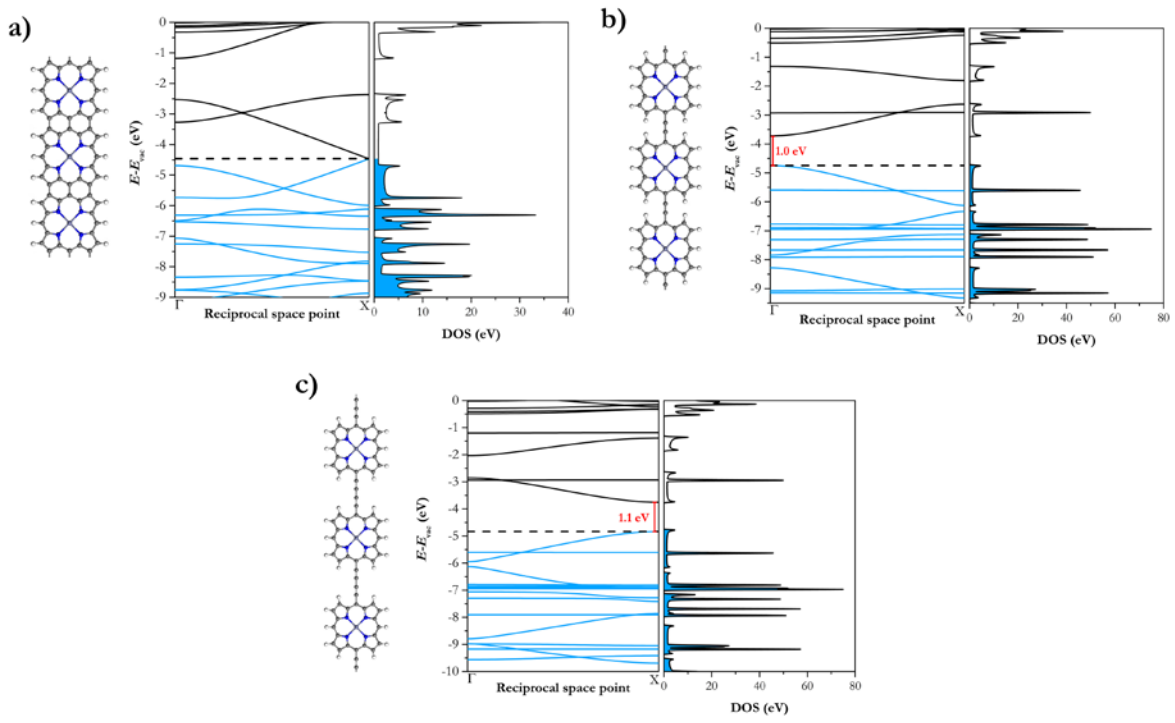

Figure 6.2. Band structures and density of states of the a) C0-, b) C2- and c) C4-linked porphyrin linear chains using the HSE06 functional. Energies are given with respect to the vacuum level (E_{vac}). Dashed lines represent the Fermi level; occupied levels are shown in blue.

The reciprocal space point at which the narrowest gap is obtained changes from the zone border (X) for the C0 chain, to the zone centre (Γ) for the C2 chain, and back to

the zone border (X) for the C4 chain. A similar behaviour (oscillation of the point of narrowest gap between the zone centre and the boundary) will be reported for other porphyrin arrays below, so it is useful to explain this behaviour in more detail.

Figure 6.3 shows contour plots of the highest occupied and lowest unoccupied crystal orbitals (HOCO and LUCO) in the linear chains. The reciprocal space point of these crystal orbitals is related to the relative sign of the wavefunctions at neighbouring porphyrin units. In the C0 and C4 linear chains, consecutive porphyrin units have frontier orbitals in antiphase, whereas in the C2 linear chain, they are in phase. This is related to the number of triple bonds in the linker. All of the HOCO states have alternating signs on consecutive triple bonds in the linker, while all of the LUCO states have alternating signs on consecutive single bonds. Generalising this result, porphyrin chains with alkyne C_n linkers can be expected to have in-phase (Γ point) HOCO and LUCO states if the number of triple bonds ($n/2$) is odd and to have antiphase (zone-boundary) HOCO and LUCO states if $n/2$ is even or zero. This prediction has been tested using linear chains with longer linkers (C6 – C10), and the expected result if confirmed. This behaviour is not unique to porphyrin chains; the test calculations lead to the same alternation for linear chains of C_n-linked benzene units, although in that case the C2 system has HOCO/LUCO at the X point, C4 at the Γ point, etc. (the band structure for the C2 case, the linear phenylacetylene chain, is reported in Ref. [36]). In comparison with the linear benzene chains, the linear porphyrin chains tend to exhibit much narrower gaps.

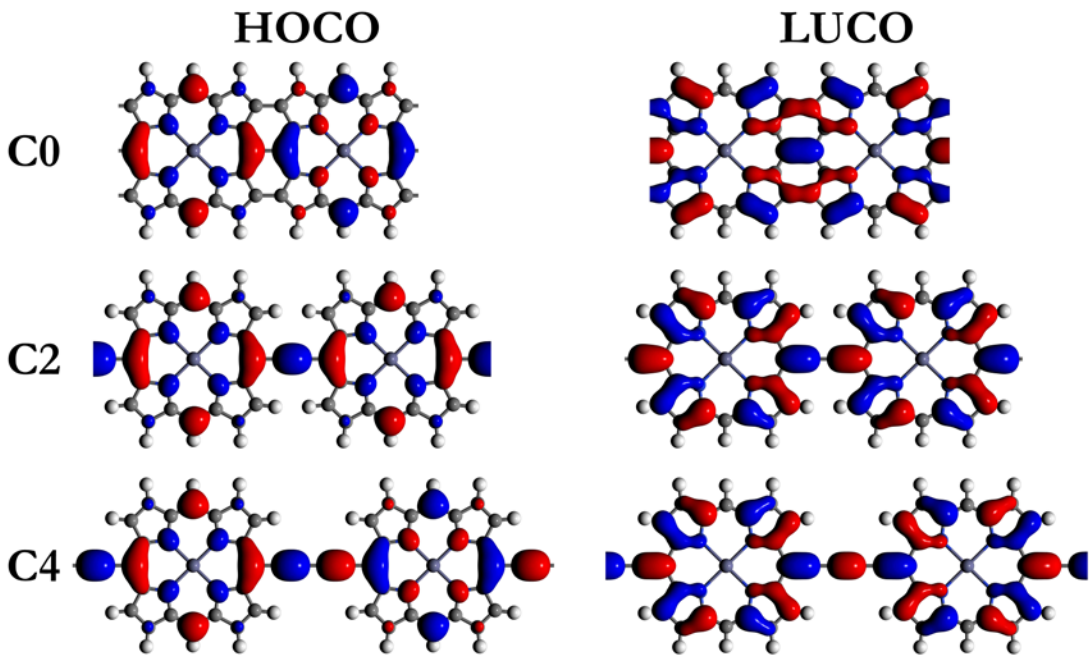

Figure 6.3. HOCO and LUCO isosurfaces at the Γ (C2 linkage) and X (C0 and C4 linkage) points for porphyrin linear chains. Blue and red represent opposite signs of the wavefunctions.

I now discuss the calculated electronic structure of the porphyrin linear chains in the context of previous theoretical work. Yamaguchi [37] studied this Zn-porphyrin fused tape (C0) using a GGA functional and obtained a zero-gap band structure similar to one reported in this section. In contrast, the DFT-based tight-binding (DFTB) calculations of Pedersen *et al.* [38] predicted a band gap of 0.63 eV. Both set of calculations involve severe approximations, and in particular, the GGA is well known to underestimate band gaps, so the prediction of Yamaguchi required confirmation from a more advanced method. Calculations for this study using a screened hybrid functional indeed confirm that the Zn-porphyrin C0 linear chain has a zero or near-zero gap. On the other hand, Ohmori *et al.* [39] also performed hybrid functional (B3LYP) calculations of a similar polymer but with free-base porphyrins (*i.e.*, 2 H atoms instead of Zn at the porphyrin centre). These calculations led to a small band gap (~0.5 eV) which is related to the symmetry breaking by the free-base porphyrins. I have tested that HSE06 calculations indeed lead to a small band gap opening if the Zn is replaced by two H atoms at the porphyrin centres. A

previous theoretical investigation of the C2-linked infinite linear chain was reported by Susumu *et al.* [40]. Despite the simple theoretical model employed in that work (tight-binding model under the Hückel approximation), their band structure (with a band gap of 1.15 eV) agrees very well with that reported here at a higher level of calculation.

6.3.2 Porphyrin nanosheets

The optimised geometric parameters of 2D Zn-porphyrin nanosheets with C0, C2 and C4 linkers are shown in **Table 6.2**. The results are very similar to those listed in **Table 6.1** for the linear chains.

Table 6.2. Optimised geometric parameters of the porphyrin nanosheets*.

	C0	**C2**	**C4**
d[C_{meso}–C_{meso}] (Å)	1.46	4.07	6.62
d[C_{β}–C_{β}] (Å)	1.41	4.05	6.56
d[Zn–N] (Å)	2.04	2.06	2.06
cell length a (Å)	8.42	11.03	13.55

* The parameter a is the lattice constant in the periodic dimension

Figure 6.4 shows the electronic band structures of the porphyrin nanosheets along the irreducible Brillouin zone defined by the high-symmetry points M, Γ and X in reciprocal space. In the C0-linked nanosheet, the highest occupied band crosses the Fermi level, implying metallic behaviour. On the other hand, both the C2-linked and C4-linked nanosheets (**Figure 6.4b** and **c**) exhibit a small band gap. For the C2-linked nanosheet, the narrowest gap is E_g = 0.55 eV at the Γ point, whereas for the C4-linked nanosheet (**Figure 6.4c**), the narrowest gap is E_g = 0.31 eV at the M point.

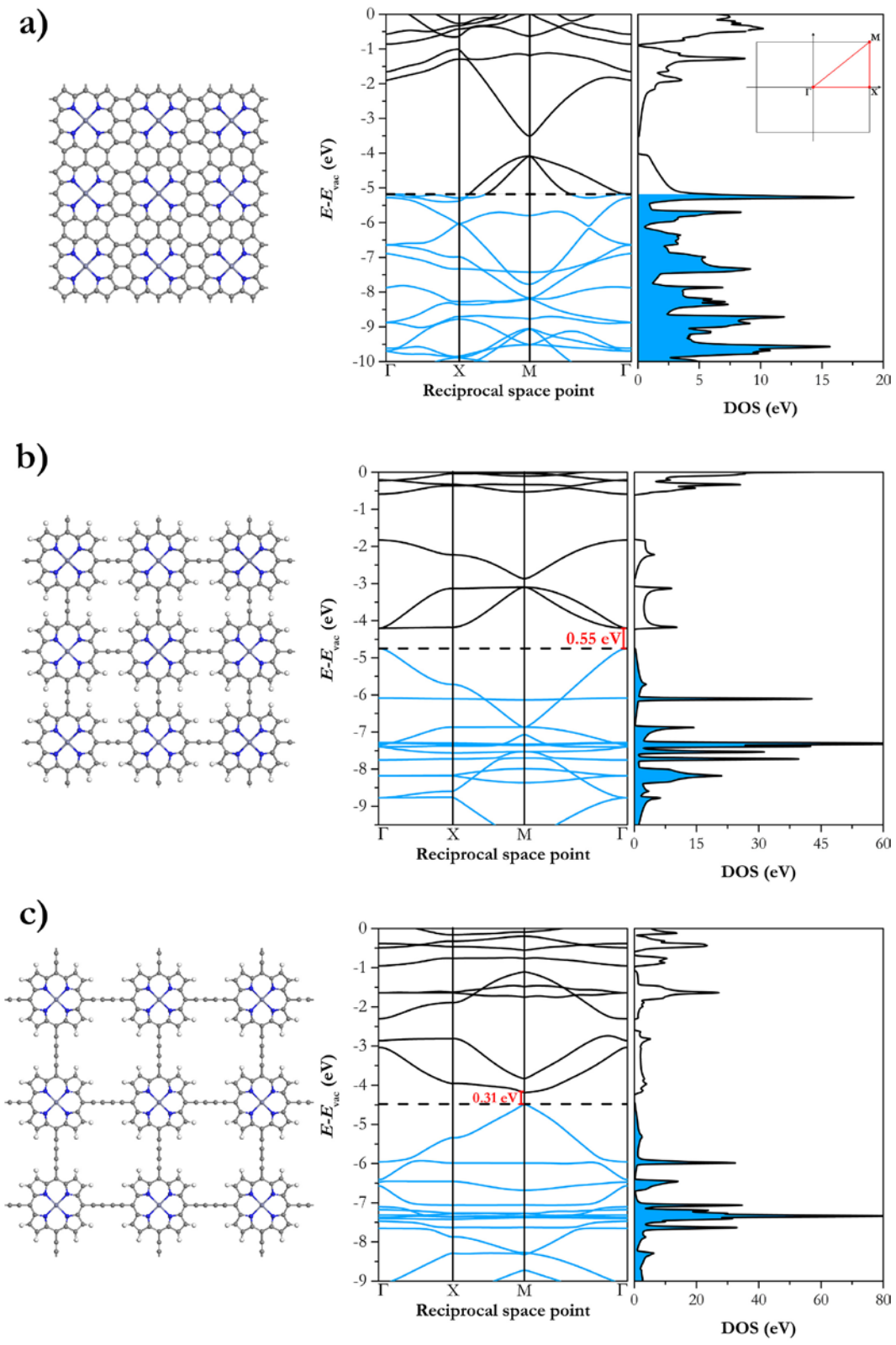

Figure 6.4. Band structures of the a) C0-, b) C2- and c) C4-linked porphyrin nanosheets using the HSE06 functional. Energies are given with respect to the vacuum level (E_{vac}). Dashed lines represent the Fermi level; occupied levels are shown in blue.

The C0 Zn-porphyrin nanosheets have been theoretically investigated before by Tan *et al.* [41] and by Yamaguchi [42] using GGA functionals. Their results agree with ours in predicting a non-spin-polarised ground state with metallic band structure. My work therefore confirms the absence of a band gap to this system, showing that this is not a result of using a GGA functional (which can erroneously predict gapless electronic structures in semiconducting materials). The band structures of the C2 porphyrin nanosheet was calculated by Susumu *et al.* using tight-binding calculations [40]. Their results are similar to the ones presented in this section, except that they report a wider band gap (0.79 eV) than this work (0.55 eV). Finally, the band structure of the C4 nanosheet has been recently reported by Allec *et al.* [22] using the HSE06 functional and localised basis sets. The band structure obtained is qualitatively similar to theirs, with a gap opening at the M point, but the band gap obtained here (0.31 eV) is much narrower than in their work (0.81 eV). Since the same functional is used in both studies, the discrepancy might be due to the different type of basis sets, which requires further investigation.

6.3.3 Porphyrin nanotubes

Porphyrin-based nanotubes are very interesting hypothetical nanostructures which can be seen as the limit of many stacked porphyrin nanorings [17-22]. I consider here the properties of nanotubes formed by the stacking of nanorings with six porphyrin units and three types of linkage (C0, C2, C4; **Figure 6.5a**-**c**). A nanotube with different types of linker was also considered: C4 around the ring and C2 along the tube (**Figure 6.5d**).

The optimised geometric parameters for all of the nanotubes as well as the strain energies (difference in energy with respect to the corresponding 2D nanosheet) are shown in **Table 6.3**.

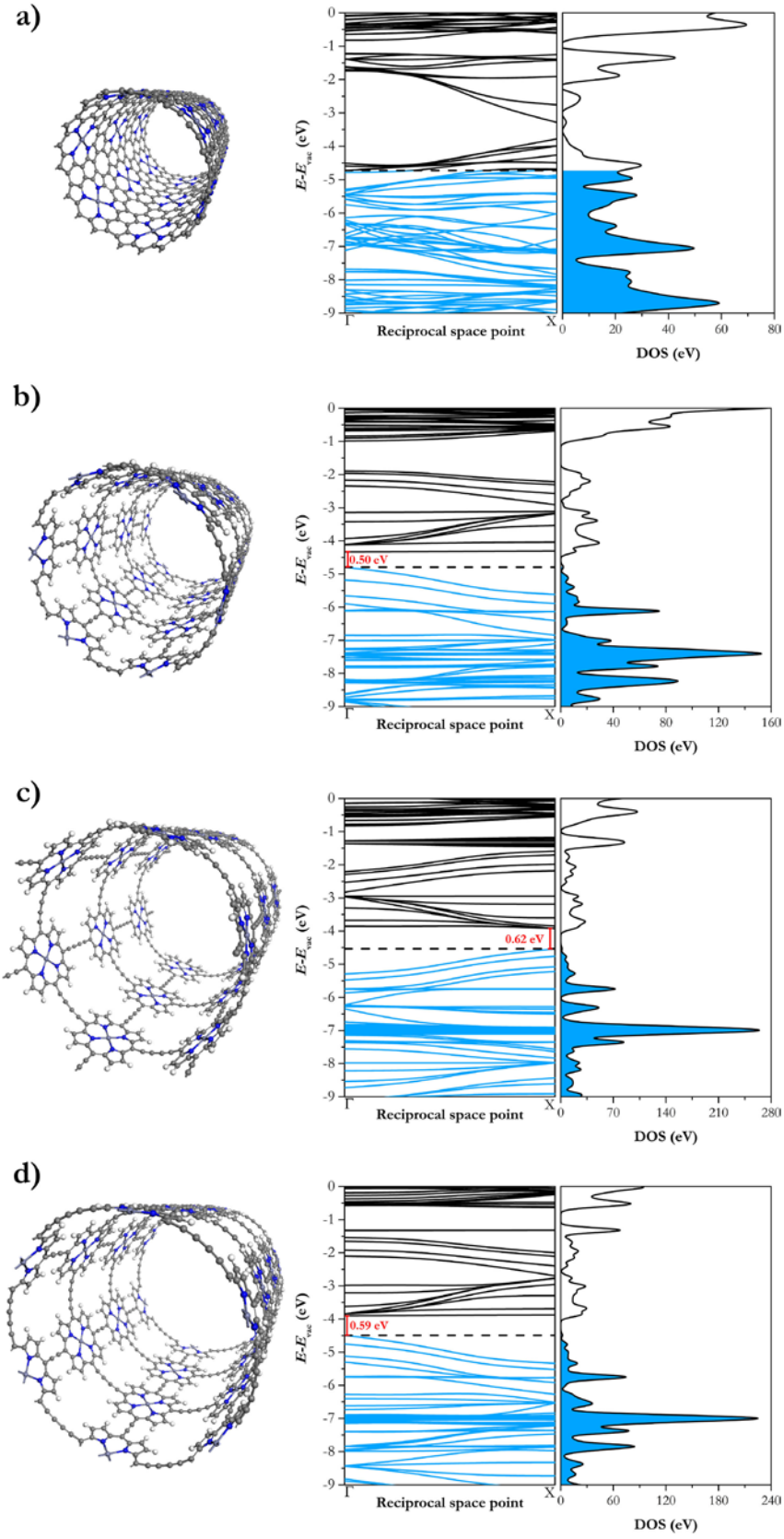

Figure 6.5. Band structures of the a) C0-, b) C2-, c) C4- and d) C2/C4-linked porphyrin nanotubes using the HSE06 functional. Electron energies are given with respect to the vacuum level (E_{vac}). Dashed lines represent the Fermi level; occupied levels are shown in blue.

Table 6.3. Optimised geometric parameters and strain energies for the porphyrin nanotubes*.

	C0	C2	C4	C2/C4
d[C_{meso}–C_{meso} ⊥] (Å)	1.45	4.03	6.55	6.61
d[C_{meso}–C_{meso} ∥] (Å)	1.44	4.10	6.59	4.06
d[C_{β}–C_{β} ⊥] (Å)	1.37	4.07	6.50	6.57
d[C_{β}–C_{β} ∥] (Å)	1.40	4.07	6.55	4.05
d[Zn–N] (Å)	2.06	2.04	2.05	2.05
cell length a (Å)	8.49	11.04	13.54	11.03
diameter (Å)	15.96	21.04	24.03	25.98
E_{strain} (eV/porphyrin)	0.58	0.29	0.11	0.10

* The parameter a is the lattice constant in the periodic dimension. Symbols ∥ and ⊥ denote the directions parallel and perpendicular to the tube axis, respectively. The strain energies are obtained using the PBE-D2 functional.

As expected, the strain is highest for the C0 nanotubes, as in the absence of linkers the porphyrin units have to accommodate the strain by distorting their planar structure, and becomes lower with longer chains linking the porphyrin units. The strain is lowest when C4 linkers are connecting the porphyrins along the circumference (C4 or C2/C4 nanotubes), whereas the nature of the linker connecting porphyrins along the direction parallel to the nanotube axis is less relevant, as seen in **Section 3.5**. In order to put the calculated strain energies in context, the strain energies were also calculated for (6,6) carbon and boron nitride nanotubes at the same level of theory employed here, giving 0.12 and 0.07 eV/atom, respectively. The values in **Table 6.3** for the porphyrin nanotubes correspond to 0.09, 0.04 and 0.02 eV per heavy atom (C or N, *i.e.* excluding H atoms as they are monocoordinated and do not contribute to strain) for C0, C2 and C4, respectively. Therefore, porphyrin nanotubes reported here are as or even less strained than typical carbon or boron nitride nanotubes. In terms of geometry, internal bond distances and cell parameters are very similar to those reported for the porphyrin linear chains and nanosheets, with deviations of less than 1.5% in the cell parameter.

The band structures obtained for the porphyrin nanotubes (**Figure 6.5**) follow the same pattern as the porphyrin nanosheets: whereas the C0 system is metallic, the presence to the C_n linkers leads to small band gap openings. The band gaps are 0.50 eV for the C2 nanotube (at the Γ point) and 0.62 eV for the C4 nanotube (at the X point). The C2/C4 system has a band gap (0.59 eV) closer to that of the C4 system but at the Γ point like in the C2 system. This indicates that the reciprocal space position of the narrowest gap is determined by the nature of the linkers along the nanotube axis, which is not surprising given that this is the periodic direction, whereas the magnitude of the gap is mostly determined by the nature of the linkers across the nanotube circumference.

In the semiconducting C_n-linked nanotubes we can observe flat conduction bands whereas the valence bands exhibit significant dispersion, suggesting much lower effective masses for holes than for conducting electrons. This is in agreement with the work by Allec *et al.* [22], who calculated the effective hole masses for a series of C4-linked nanotubes with a different number of porphyrin units along the tube circumference. Their calculated band gap for the six-porphyrin C4-linked nanotube was 0.77 eV, somewhat wider than the value reported here of 0.62 eV. The same trend was observed above when comparing the band gaps of the C4 nanosheets. Since these authors also employed the HSE06 functional, the different result is probably due to basis set effects (they employed localised basis sets, which are more difficult to converge than planewave basis sets).

6.3.4 Evolution of electronic structure of nanorings toward the infinite nanotube limit

Whereas actual porphyrin nanotubes have not been synthesised yet, recent progress in stacking porphyrin rings (only two rings so far) [21] suggests that the synthesis of such nanotubes might be feasible. I discuss now how the electronic properties of stacked porphyrin rings vary with the number of rings and converge to the behaviour of the infinite

1D nanotube. Nonperiodic structures have been considered consisting of *n* stacked rings (*n* = 1, 2, 3 or 4) of porphyrins connected by C4 linkers. These systems are labelled following the notation in Ref. [21]: *c*-**P6** for the cyclic porphyrin hexamer, *t*-**P12** for the "tubular" system consisting of *n* = 2 stacked rings (12 porphyrins in total), *t*-**P18** for *n* = 3, and so on.

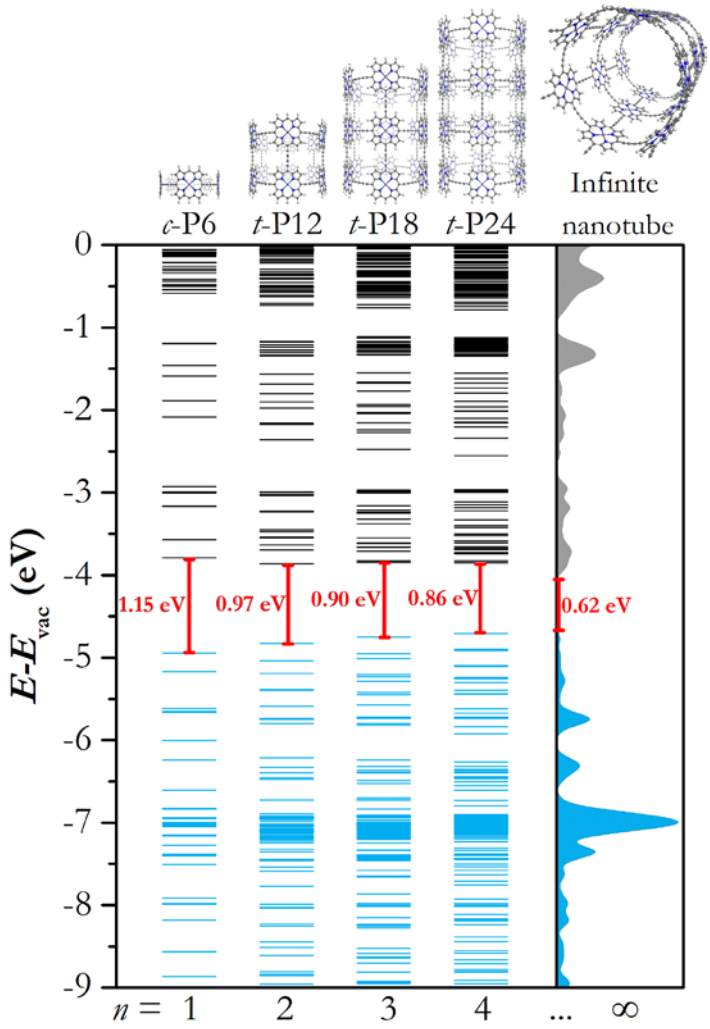

Figure 6.6. Calculated energy levels of nanorings as a function of the number (*n*) of stacked rings in comparison with the density of states of the C4-linked nanotube using the HSE06 functional. Numbers in red are the HOMO-LUMO gap (band gap for the periodic nanostructure). Occupied levels are shown in blue.

The energies of the electronic levels are plotted in **Figure 6.6**, showing how the electronic structure tends toward that of the infinite nanotube when *n* increases. The HOMO-LUMO gaps of the finite nanorings are wider than the band gap of the infinite

nanotube, but when the number of stacked rings increases, the gap decreases and tends toward the nanotube band gap. An empirical equation was found for the band gap variation in the form:

$$E_g(n) = E_g(\infty) + \frac{0.53\ \text{eV}}{n^{0.57}} \tag{6.1}$$

where $E_g(\infty)$ = 0.62 eV is the band gap for the periodic nanotube (**Figure 6.7**). More points would be needed to confirm this trend, but these calculations are very demanding computationally. The current fitting curve suggests than even for a "large" tube of 10 stacked rings the HOMO-LUMO gap will still be ~0.14 eV above the infinite nanotube limit.

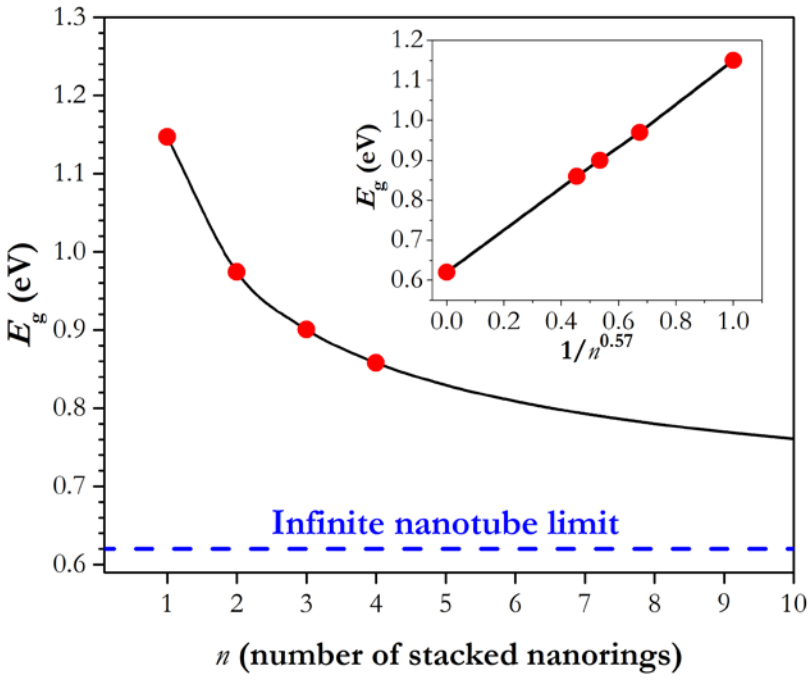

Figure 6.7. Variation of the HOMO-LUMO gaps of nanorings toward the infinite porphyrin nanotube. *n* is the number of stacked nanorings.

6.4 Conclusion

Systematic investigation of the electronic structure of Zn-porphyrin nanostructures has been performed, including linear chains, 2D nanosheets, and both finite and infinite nanotubes. In particular, the effect of the nature of the linker connecting the porphyrin

units was investigated and we have observed some strong variations in electronic structure with linker length.

It is evident that when the porphyrin units are "fused" (C0 case) there is no band gap in the electronic structure for any of the nanostructures considered here. The C0 nanosheets and nanotubes have metallic band structures, whereas the C0 linear chain (fused porphyrin tape) exhibits a zero-gap band structure with a Dirac-like point at the Brillouin zone boundary.

Narrow band gaps (of ~1 eV or less) open in all nanostructures where the porphyrin units are connected by ethyne (C2) or butadiyne (C4) linkers. The widest opening is observed for the linear chains (1.0 and 1.1 eV for C2 and C4 linkers, respectively), whereas for the nanosheets and nanotubes the band gaps are significantly narrower (0.3-0.6 eV). Finite porphyrin tubes, made of a few stacked rings, have wider excitation gaps than the infinite (periodic) nanotubes, and it has been described the variation of their electronic structures with the number of stacked rings.

The investigated nanostructures exhibit significant band dispersion, suggesting high carrier mobilities. The exception is the conduction bands of the nanotubes, which appear to be remarkably flat. The reciprocal space point at which the band gap is observed is shown to oscillate between the zone centre and the zone boundary, depending on the length of the linkers. Neighbouring porphyrin units can be expected to be in phase in the HOCO and LUCO states if the number of triple bonds ($n/2$) in the linker C_n between them is odd and in antiphase if $n/2$ is even or zero. The narrowest gap in the band structure is observed at the zone centre in the former case and at the zone boundary in the latter case.

This work theoretically demonstrates that it is possible to design porphyrin nanostructures with tailored electronic properties such as specific band gap values and band structures by varying the type of the linkage used between each porphyrin unit and

the type of self-assemble formations (linear chains, nanosheets, nanotubes and nanorings). These tunable electronic properties represent promising opportunities for light-harvesting or photocatalytic applications.

6.5 References

1. Cogdell, R.J., A. Gall, and J. Köhler, *The architecture and function of the light-harvesting apparatus of purple bacteria: from single molecules to in vivo membranes.* Quarterly Reviews of Biophysics, 2006. **39**(3): p. 227-324.
2. Nakamura, Y., N. Aratani, and A. Osuka, *Cyclic porphyrin arrays as artificial photosynthetic antenna: synthesis and excitation energy transfer.* Chemical Society Reviews, 2007. **36**(6): p. 831-845.
3. Campbell, W.M., et al., *Porphyrins as light harvesters in the dye-sensitised TiO2 solar cell.* Coordination Chemistry Reviews, 2004. **248**(13): p. 1363-1379.
4. Crossley, M.J. and P.L. Burn, *An approach to porphyrin-based molecular wires: synthesis of a bis(porphyrin)tetraone and its conversion to a linearly conjugated tetrakisporphyrin system.* Journal of the Chemical Society, Chemical Communications, 1991(21): p. 1569-1571.
5. Sedghi, G., et al., *Long-range electron tunnelling in oligo-porphyrin molecular wires.* Nature Nanotechnology, 2011. **6**(8): p. 517-523.
6. Li, Z., et al., *Quasi-Ohmic Single Molecule Charge Transport through Highly Conjugated meso-to-meso Ethyne-Bridged Porphyrin Wires.* Nano Letters, 2012. **12**(6): p. 2722-2727.
7. Kuang, G., et al., *Resonant Charge Transport in Conjugated Molecular Wires beyond 10 nm Range.* Journal of the American Chemical Society, 2016. **138**(35): p. 11140-11143.
8. Ferreira, Q., et al., *Conductance of Well-Defined Porphyrin Self-Assembled Molecular Wires up to 14 nm in Length.* The Journal of Physical Chemistry C, 2014. **118**(13): p. 7229-7234.

9. Lin, V.S., S.G. DiMagno, and M.J. Therien, *Highly conjugated, acetylenyl bridged porphyrins: new models for light-harvesting antenna systems.* Science, 1994. **264**(5162): p. 1105.

10. Susumu, K., et al., *Conjugated Chromophore Arrays with Unusually Large Hole Polaron Delocalization Lengths.* Journal of the American Chemical Society, 2006. **128**(26): p. 8380-8381.

11. Sedghi, G., et al., *Comparison of the Conductance of Three Types of Porphyrin-Based Molecular Wires: β,meso,β-Fused Tapes, meso-Butadiyne-Linked and Twisted meso-meso Linked Oligomers.* Advanced Materials, 2012. **24**(5): p. 653-657.

12. Tsuda, A. and A. Osuka, *Fully Conjugated Porphyrin Tapes with Electronic Absorption Bands That Reach into Infrared.* Science, 2001. **293**(5527): p. 79.

13. Anderson, H.L., *Conjugated Porphyrin Ladders.* Inorganic Chemistry, 1994. **33**(5): p. 972-981.

14. Taylor, P.N., et al., *Conjugated porphyrin oligomers from monomer to hexamer.* Chemical Communications, 1998(8): p. 909-910.

15. Nakamura, Y., et al., *A Directly Fused Tetrameric Porphyrin Sheet and Its Anomalous Electronic Properties That Arise from the Planar Cyclooctatetraene Core.* Journal of the American Chemical Society, 2006. **128**(12): p. 4119-4127.

16. Singh, H.K., P. Kumar, and U.V. Waghmare, *Theoretical Prediction of a Stable 2D Crystal of Vanadium Porphyrin: A Half-Metallic Ferromagnet.* The Journal of Physical Chemistry C, 2015. **119**(45): p. 25657-25662.

17. Hoffmann, M., et al., *Enhanced π Conjugation around a Porphyrin[6] Nanoring.* Angewandte Chemie International Edition, 2008. **47**(27): p. 4993-4996.

18. Hoffmann, M., et al., *Template-Directed Synthesis of a π-Conjugated Porphyrin Nanoring.* Angewandte Chemie International Edition, 2007. **46**(17): p. 3122-3125.

19. O'Sullivan, M.C., et al., *Vernier templating and synthesis of a 12-porphyrin nano-ring.* Nature, 2011. **469**: p. 72.

20. Rickhaus, M., et al., *Single-Acetylene Linked Porphyrin Nanorings.* Journal of the American Chemical Society, 2017. **139**(46): p. 16502-16505.

21. Neuhaus, P., et al., *A Molecular Nanotube with Three-Dimensional π-Conjugation.* Angewandte Chemie International Edition, 2015. **54**(25): p. 7344-7348.

22. Allec, S.I., N.V. Ilawe, and B.M. Wong, *Unusual Bandgap Oscillations in Template-Directed π-Conjugated Porphyrin Nanotubes.* The Journal of Physical Chemistry Letters, 2016. **7**(13): p. 2362-2367.

23. Kresse, G., Furthmüller, J., *Efficiency of ab-initio total energy calculations for metals and semiconductors using a plane-wave basis set.* Comput. Mater. Sci., 1996. **6**: p. 15 - 50.

24. Kresse, G., Furthmüller, J., *Efficient iterative schemes for ab initio total-energy calculations using a plane-wave basis set.* Phys. Rev. B: Condens. Matter Mater. Phys., 1996. **54**(16): p. 11169 - 11186.

25. Perdew, J.P., K. Burke, and M. Ernzerhof, *Generalized Gradient Approximation Made Simple.* Physical Review Letters, 1996. **77**(18): p. 3865-3868.

26. Perdew, J.P., K. Burke, and M. Ernzerhof, *Generalized Gradient Approximation Made Simple [Phys. Rev. Lett. 77, 3865 (1996)].* Physical Review Letters, 1997. **78**(7): p. 1396-1396.

27. Heyd, J., G.E. Scuseria, and M. Ernzerhof, *Hybrid functionals based on a screened Coulomb potential.* The Journal of Chemical Physics, 2003. **118**(18): p. 8207-8215.

28. Heyd, J., G.E. Scuseria, and M. Ernzerhof, *Erratum: "Hybrid functionals based on a screened Coulomb potential" [J. Chem. Phys. 118, 8207 (2003)].* The Journal of Chemical Physics, 2006. **124**(21): p. 219906.

29. Zhu, G., et al., *Porphyrin-based porous sheet: Optoelectronic properties and hydrogen storage.* International Journal of Hydrogen Energy, 2015. **40**(9): p. 3689-3696.

30. Henderson, T.M., J. Paier, and G.E. Scuseria, *Accurate treatment of solids with the HSE screened hybrid.* physica status solidi (b), 2011. **248**(4): p. 767-774.

31. Garza, A.J. and G.E. Scuseria, *Predicting Band Gaps with Hybrid Density Functionals.* The Journal of Physical Chemistry Letters, 2016. **7**(20): p. 4165-4170.

32. Aziz, A., et al., *Porphyrin-based metal-organic frameworks for solar fuel synthesis photocatalysis: band gap tuning via iron substitutions.* Journal of Materials Chemistry A, 2017. **5**(23): p. 11894-11904.

33. Hamad, S., et al., *Electronic structure of porphyrin-based metal–organic frameworks and their suitability for solar fuel production photocatalysis.* Journal of Materials Chemistry A, 2015. **3**(46): p. 23458-23465.

34. Souza, I., N. Marzari, and D. Vanderbilt, *Maximally localized Wannier functions for entangled energy bands.* Physical Review B, 2001. **65**(3): p. 035109.

35. Butler, K.T., C.H. Hendon, and A. Walsh, *Electronic Chemical Potentials of Porous Metal–Organic Frameworks.* Journal of the American Chemical Society, 2014. **136**(7): p. 2703-2706.

36. Kondo, M., et al., *Electronic structures and band gaps of chains and sheets based on phenylacetylene units.* Chemical Physics, 2005. **312**(1): p. 289-297.

37. Yamaguchi, Y., *Time-dependent density functional calculations of fully π-conjugated zinc oligoporphyrins.* The Journal of Chemical Physics, 2002. **117**(21): p. 9688-9694.

38. Pedersen, T.G., et al., *Theoretical study of conjugated porphyrin polymers.* Thin Solid Films, 2005. **477**(1): p. 182-186.

39. Ohmori, S., et al., *Molecular design of high performance fused porphyrin one-dimensional wire: A DFT study.* Thin Solid Films, 2009. **518**(2): p. 901-905.

40. Susumu, K., et al., *Theoretical approach to the design of supramolecular conjugated porphyrin polymers.* Journal of Materials Chemistry, 2001. **11**(9): p. 2262-2270.

41. Tan, J., et al., *Stable ferromagnetism and half-metallicity in two-dimensional polyporphyrin frameworks*. RSC Advances, 2013. **3**(19): p. 7016-7022.

42. Yamaguchi, Y., *Theoretical study of two-dimensionally fused zinc porphyrins: DFT calculations*. International Journal of Quantum Chemistry, 2009. **109**(7): p. 1584-1597.

7 Engineering the electronic and optical properties of 2D porphyrin-paddlewheel metal-organic frameworks

Metal-organic frameworks (MOFs) are promising photocatalytic materials due to their high surface area and tuneability of their electronic structure. In this Chapter, we discuss how to engineer the band structures and optical properties of a family of two-dimensional (2D) porphyrin-based MOFs, consisting of *M*-tetrakis(4-carboxyphenyl)porphyrin structures (*M*-TCPP, where *M* = Zn^{2+} or Co^{2+}) and metal (Co^{2+}, Ni^{2+}, Cu^{2+} or Zn^{2+}) paddlewheel clusters, with the aim of optimising their photocatalytic behaviour in solar fuel synthesis reactions (water-splitting and/or CO_2 reduction). Based on density functional theory (DFT) and time-dependent DFT simulations with a hybrid functional, we studied three types of composition/structural modifications: a) varying the metal centre at the paddlewheel or at the porphyrin centre to modify the band alignment; b) partially reducing the porphyrin unit to chlorin, which leads to stronger absorption of visible light; and c) substituting the benzene bridging between the porphyrin and paddlewheel, by ethyne or butadiyne bridges, with the aim of modifying the linker to metal charge transfer behaviour. Our work offers new insights on how to improve the photocatalytic behaviour of porphyrin- and paddlewheel-based MOFs. All the periodic DFT calculations in this

Chapter have been carried out by me; some supporting calculations of cluster using time-dependent DFT were carried out by the group of Rachel Crespo-Otero at Queen Mary University of London.

7.1 Introduction

Metal-organic frameworks (MOFs) are materials where metal atoms or cluster are connected via organic linkers to form rigid frameworks, often with a porous structure [1]. They have found applications in gas (*e.g.* CO_2, H_2) storage and separation [2-6]. More recently, MOFs have been investigated as potential photocatalysts due to their tuneable electronic structure and optical behaviour, as there is a huge compositional space of transition metal ions/clusters or multidentate organic linkers that can be incorporated into the framework [7-9]. Several strategies have been designed to modify MOFs for enhanced photocatalytic performance, including linker functionalisation [10-12], mixing metals/linkers [13-16], and metal nanoparticle loading [17-20].

Porphyrin-like organic units are particularly attractive as a component of MOF photocatalysts, due to their remarkable light absorbing properties, which is also the basis of natural photosynthetic systems [21-23]. Several porphyrin-based MOFs have been investigated for photocatalysis. For example, Fateeva *et al.* reported a water-stable porphyrin-based MOF with Al-carboxylate clusters as metal nodes, capable of performing photocatalytic production of hydrogen from water, in the presence of Pt nanoparticles [19]. A MOF consisting of Zn metalloporphyrins connected to Zr_6O_8 clusters through carboxylic groups, coupled with an organometallic $[Fe_2S_2]$ complex, has also shown photocatalytic activity for hydrogen evolution [24]. Leng *et al.* [25] reported an indium-based porphyrinic MOF, USTC-8(In), where one-dimension In-oxo chains are connected by the porphyrin units, with excellent photocatalytic H_2 production under visible light. In this system, the out-of-plane In^{3+} ions detach from the porphyrin ligands

under excitation, avoiding the fast back electron transfer and thus electron-hole separation is improved. MOFs consisting of Ru_2 paddlewheels units and Zn-porphyrins were reported by Lan *et al.* [26] to exhibit visible-light photocatalytic activity for hydrogen evolution, without the presence of metal co-catalysts. In that case, the proximity of the Ru cluster to the porphyrin (~11 Å) was found to facilitate the electron transfer from the photoexcited porphyrins to the metal clusters.

There has been recent interest in creating two-dimensional (2D) photocatalytic MOFs, which could benefit from very accessible active sites and short paths for the photogenerated charge carriers to reach the solid-water interface. Wang *et al.* [20] have proposed ultrathin porphyrin-based MOFs consisting of Ti_7O_6 clusters and free-based porphyrin connected by H_2TCPP linkers, which exhibited excellent photocatalytic hydrogen evolution in the presence of Pt as co-catalyst. Porphyrin-based quasi-2D lanthanide MOFs with different thicknesses were synthesised by Jiang *et al.* [27], demonstrating that the thinner materials had higher Brunauer-Emmett-Teller (BET) surface area, light harvesting ability, carrier density, separation efficiency, and therefore better photocatalytic performance.

Despite the remarkable progress in recent years, porphyrin-based MOFs still need efficiency improvement in the light absorption and charge separation processes to become viable photocatalysts. The optical behaviour of porphyrin-based MOFs is still not well understood at a fundamental level, which hinders the optimisation process. Computer simulations base on density functional theory (DFT) can be very useful in rationalising the electronic and optical properties of MOFs [28]. Previous theoretical work from our group [29, 30] on 3D porphyrin-based MOFs similar to those synthesised by Fateeva *et al.* [19] has shown that the choice of metal at the porphyrin centre or at the metal clusters can be used to optimise the band alignment for the photocatalytic process. Also, we showed that when Al cations in the PMOFs are replaced by Fe cations, the position of the conduction

band edge is lowered significantly, and that the Fe/Al composition in a mixed metal system can be used to tune the band edge positions.

In this section, we investigate a class of 2D porphyrin-based MOFs consisting of *M*-tetrakis(4-carboxyphenyl)porphyrin structures (*M*-TCPP, where $M = Zn^{2+}$ or Co^{2+}) and metal paddlewheel clusters ($M_2(COO^-)_4$). It is known that the metal paddlewheel cluster structure can accommodate different metals, *e.g.* $M = Co^{2+}$, Ni^{2+}, Cu^{2+}, Zn^{2+}, Cd^{2+}, Mn^{2+} [31]. We consider here metal paddlewheels made of late 3*d* metals ($M = Co^{2+}$, Ni^{2+}, Cu^{2+} or Zn^{2+}). The paddlewheel cluster comprises of two divalent metal ions bridged together by four carboxylate ligands. Each paddlewheel is then linked to four porphyrin units (**Figure 7.1**). A MOF with this layer structure was synthesised by Choi *et al.* [32] in bulk form, with layers exhibiting AB staking. Zhao *et al.* [33, 34] showed how to grow this material anisotropically, with help of surfactants, to create 2D nanosheets with only 8±3 layers. Spoerke and co-workers [35] also reported the synthesis and characterisation of 2D structures consisting of Zn-paddlewheels and Zn-porphyrins and showed that these structures can serve as active component in photovoltaic systems.

The presence of porphyrin in a 2D pattern, and the possibility of tuning the electronic properties by changing the paddlewheel metal, make this family of materials potentially interesting for photocatalysis. One possible concern is the poor hydrolytic stability of some paddlewheel frameworks [36, 37]. At harsh environments (*i.e.* high loads of water), a hydrolysis reaction of water molecules with Cu-O-C group can induce the paddlewheel structural decomposition [36]. However, the stability in water depends on the nature of the metal in the paddlewheel and on the water loading [38, 39] which means that some of the 2D-MOFs investigated here could still be useful as photocatalysts. They are also promising in other applications (*e.g.* as photovoltaic materials), where the electronic properties are of interest.

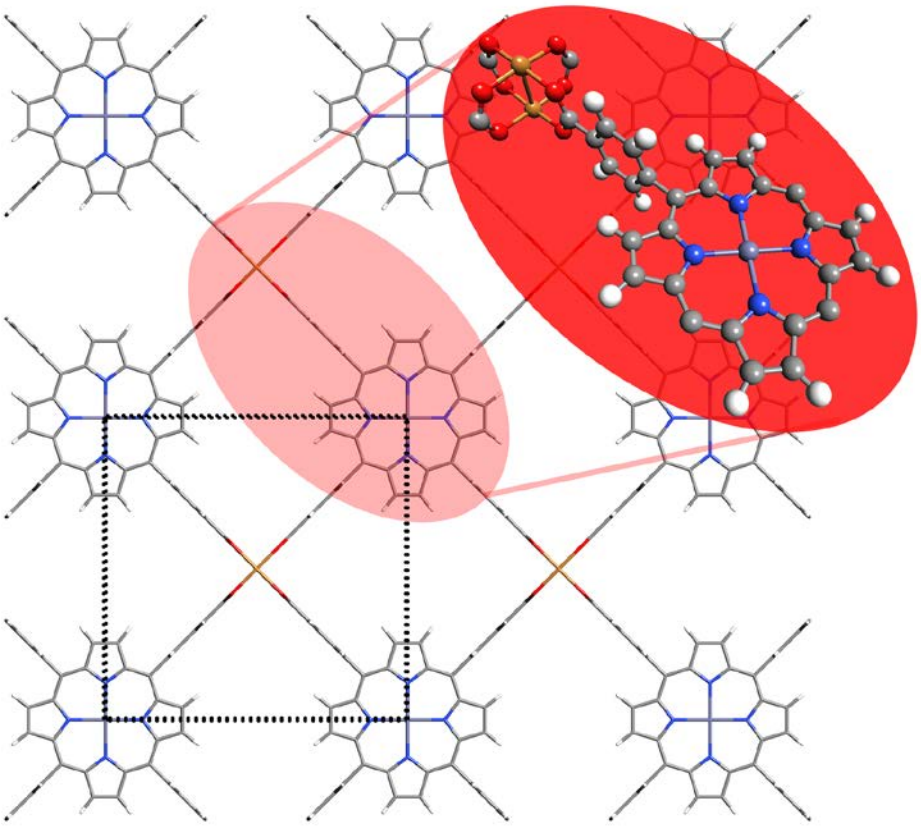

Figure 7.1. Structure of *M*-Zn-TCPP nanosheet. Inside the red-shaded circle, detailed structure of a single model of paddlewheel/linker/porphyrin conforming the MOF and dashed black lines show the unit cell. Colour code: grey = carbon, red = oxygen, white = hydrogen, blue = nitrogen, purple = zinc and orange = transition metal.

Due to their simplicity, these 2D-MOFs provide useful model systems to investigate how to engineer the electronic and optical behaviour of porphyrin-based MOFs. The aim of this Chapter is to investigate how different modifications (change in metal centres, functionalisation of the porphyrins, or changes in the organic bridge between the porphyrin and the paddlewheel) can tune the electronic and optical properties of 2D porphyrin-paddlewheel MOFs for photocatalytic and other applications.

7.2 Methodology

Calculations of the periodic models were performed using density functional theory (DFT) as implemented in the VASP program [40, 41]. The simulation cell consists of one Zn^{2+}

centred porphyrin linker and one metal paddlewheel node (**Figure 7.1**). Vacuum regions separating the layers from their periodic images have a width of ~20 Å.

The geometry of the atomic structure and lateral lattice constants were optimised using generalised gradient approximation (GGA) and Perdew-Burke-Ernzerhof (PBE) [42, 43] exchange-correlation functional. Hubbard corrections were applied for Cu^{2+}, Ni^{2+} and Co^{2+} corresponded to U_{eff} values of 4.0 eV, 6.4 eV and 3.3 eV, respectively [44], respectively, and Grimme's empirical corrections were used to properly account for dispersion effects [45]. The projector augmented wave (PAW) method [46, 47] was used to describe the interaction between the frozen core electrons (*i.e.* up to 3*p* for Ni, Cu, Zn and up to 1*s* for C, N, O) and its valence electrons and a kinetic energy cut-off of 400 eV was fixed for the plane-wave basis set expansion. A Γ-centred *k*-grid of 4×4×1 *k*-point was used, which leads to 6 irreducible reciprocal lattice points. During relaxation, the cell parameters are allowed to relax while keeping the cell volume constant, so that the vacuum gap is preserved. The forces on the atoms were minimised until they were less than 0.02 eV $Å^{-1}$.

All calculations were spin-polarised and we considered all possible spin states and relative orientations of the magnetic moments for the transition metal ions. For Cu^{2+} (d^9), only one spin state is possible, with one unpaired electron. For Ni^{2+} (d^8), two spin states are possible where there can be zero or two unpaired electrons, which correspond to low-spin (LS) or high-spin (HS), respectively. In the case of Co^{2+} (d^7), two spin states are possible also where there can be one or three unpaired electrons (LS and HS, respectively). For the spin-polarised ions, both antiferromagnetic (AFM) and ferromagnetic (FM) configurations were considered.

In order to calculate more accurate electronic structure and band gap values of the materials, we performed single-point calculations on the GGA-optimised structures, using a screened hybrid functional (HSE06) [48, 49]. For these calculations, a reduced mesh of

2×2×1 *k*-point mesh was used. All the electron energies are reported with respect to the vacuum reference. As in other periodic DFT codes, the band energies in VASP are given with respect to an internal energy reference. Therefore, to obtain absolute energy levels it is necessary to evaluate the electrostatic potential in the pseudo-vacuum region represented by an empty space within the simulations cell, with a zero potential gradient. This is chosen here as the planar average in middle of the vacuum gap between the nanosheets. The MacroDensity code was employed for this purpose [50].

Using the Gaussian16 code [51], time-dependent DFT calculations (TD-DFT) were also performed by our collaborators in Queen Mary University in order to examine the excited states in some selected cases. For these calculations, the MOF systems were represented by cluster models consisting of one porphyrin and one paddlewheel unit, where all the cleaved C bonds were saturated with H atoms (see **Figures A1**, **A2** and **A3** in **Appendix**). The geometries of the clusters were fixed to those obtained from the periodic calculations. For consistency, we used the same HSE06 functional as in the VASP calculations. Triplet states were used to describe the magnetic nature of the copper paddlewheel clusters. The calculations were all-electron (*i.e.* no pseudopotentials were employed) and a 6-311G(d,p) basis set was used to expand the wavefunctions.

7.3 Results and discussion

7.3.1 Framework geometry and magnetic ground states

We first discuss how the nature of the paddlewheel metal affects the geometric and electronic properties of the framework. **Table 7.1** summarises the relative stabilities and geometric parameters of the frameworks with different paddlewheel compositions (Co, Ni, Cu or Zn), spin state and magnetic ordering. The metal at the centre of the porphyrin was kept as Zn in all cases.

Except in the case of the non-magnetic Zn^{2+} cations, we need to investigate different spin states and magnetic ordering for each paddlewheel composition. The Cu paddlewheel exhibits antiferromagnetic (AFM) coupling between the two neighbouring metal centres in the paddlewheel. This is consistent with both experimental measurements in Cu paddlewheel clusters [52-54] and with the theoretical study by Rodriguez-Fortea *et al.* [55]. For Co, the preferred spin state of the metal cation is high-spin (HS), which involves a local magnetic moment $\mu = 3\mu_B$ per Co(II) cation. This result agrees with the experimental determination by Pakula and Berry, who showed that Co(II) species are in high-spin state in Co paddlewheel units [56], although they found that the local magnetic moments were aligned antiferromagnetically within the paddlewheel, whereas in our calculation we found that the ferromagnetic alignment is more stable.

Table 7.1. Relative stability and geometric parameters for different spin states and magnetic configurations of the 2D frameworks at each paddlewheel composition. μ is the local magnetic moment on each metal atom. *d*[*M*-*M*] is the distance between metal atoms in the paddlewheel. Energies are obtained from HSE calculations at PBE+U geometries.

M	Spin state	μ (μ_B)	Magnetic configuration	Relative stability (eV)	*a* (Å)	*d* [*M*-*M*] (Å)
Co(II)	**HS**	**3**	AFM	+0.25	16.75	2.45
			FM	**0**	**16.74**	**2.53**
	LS	1	AFM	+0.50	16.65	2.34
			FM	+0.69	16.63	2.36
Ni(II)	HS	2	AFM	+1.23	16.68	2.44
			FM	+0.43	16.71	2.58
	LS	**0**	--	**0**	**16.60**	**2.38**
Cu(II)	--	**1**	**AFM**	**0**	**16.70**	**2.45**
			FM	+0.02	17.73	2.45
Zn(II)	--	0	--	--	16.80	2.55

For the Ni case, our calculations give the low-spin state as the ground state, contrasting with the experimental measurements by Pang *et al.* [53] who found a high-spin antiferromagnetic ground state in Ni paddlewheel clusters. In general, the comparison between theoretically and experimentally determined electronic ground states is difficult

for these systems, because our calculations refer to systems with coordinatively unsaturated metal centres, *i.e.* only the four equatorial carboxylate ligands are considered, whereas in most experimental situations the metal centres in the paddlewheel are saturated by additional linkers or solvent molecules, *e.g.* water [53] or ethanol [56]. If we perform our calculation for the Ni-paddlewheel system with water molecules added in axial position making each Ni centre penta-coordinated, then we find that the high-spin antiferromagnetic state is the most stable, followed by the high-spin ferromagnetic ground state, which in this case is only 0.06 eV higher in energy. In any case, we have found that the band alignment presented below does not change much with the nature of the magnetic ground state. The results below refer to the magnetic ground states found theoretically in this work for the paddlewheel units with tetra-coordinated metal centres.

The cell parameter of Zn-paddlewheel framework (16.80 Å) can be compared with the experimental value obtained by X-ray diffraction for stacked 2D porphyrin-paddlewheel nanosheets with the same composition, which was 16.71 Å [57]. The discrepancy (0.5%) is small considering the approximations in the DFT simulation, both related to the exchange-correlation functional and to ignoring vibrational effects. Furthermore, the experimental value refers to the bulk material, whereas the simulation corresponds to a single-layer material. The variation of both the cell parameter and the *M-M* distance (*d* [*M-M*]) is consistent with the trend of ionic radii for Co^{2+}, Ni^{2+}, Cu^{2+} and Zn^{2+}, which is not monotonous along the period but has a minimum value for Ni^{2+} [58]. **Figure 7.2** exhibits the distance between the metal atoms within the paddlewheel and illustrates the magnetic ordering in each paddlewheel composition.

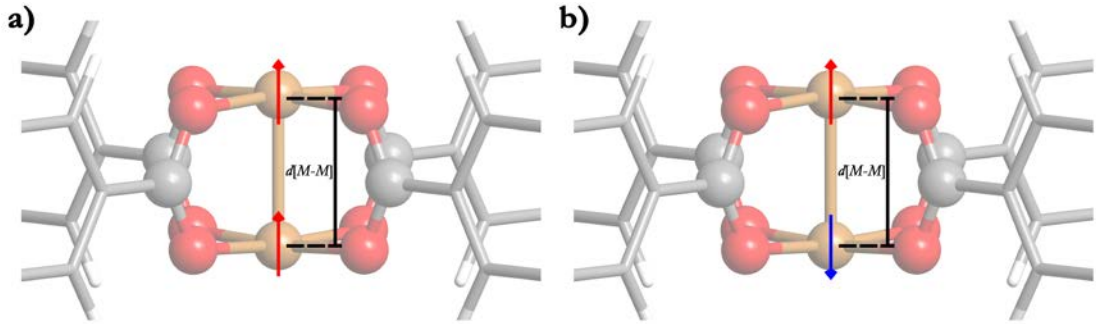

Figure 7.2. Structure of paddlewheel of *M*-Zn-TCPP nanosheet showing the a) FM and b) AFM magnetic orderings. The black lines show the distance between the metal atoms (*d* [*M*-*M*]). Colour code: grey = carbon, red = oxygen, white = hydrogen and orange = transition metal.

7.3.2 Effect of changing the paddlewheel metal on the band positioning

We now discuss the suitability of the band structure alignment for the photocatalysis of solar fuel synthesis from H_2O or CO_2, as a function of the nature of the metal in the paddlewheel. For this analysis, we need to align the band edges with respect to the vacuum potential, to obtain their absolute positions, and compare with the redox potentials for the photocatalytic reaction. The valence and conduction bands must straddle redox potentials for the given reaction. For example, for water-splitting, the valence band edge should be below the energy of the oxygen evolution reaction (OER):

$$H_2O \rightleftharpoons 2H^+_{(aq)} + \frac{1}{2}O_{2(g)} + 2e^-, \tag{7.1}$$

while the conduction band edge should be above the energy of the hydrogen evolution reaction (HER):

$$2H^+_{(aq)} + 2e^- \rightleftharpoons H_{2(g)} \tag{7.2}$$

The difference between these redox potentials is 1.23 eV and therefore the band gap needs to be higher than this value. The optimal band gap for water-splitting is ~2 eV [59] to take into consideration loss mechanisms, *i.e.* via thermal energy. At pH = 0 in vacuum scale, the potential value for OER is -5.67 eV and for HER is -4.44 eV. These potentials are shifted by $k_BT \times \text{pH} \times \ln 10$ (where k_B is Boltzmann's constant) for systems

at temperature *T* and pH > 0. The redox potentials values for water-splitting at a neutral pH and room temperature are -5.26 eV and -4.03 eV for OER (O_2/H_2O) and HER (H^+/H_2), respectively. For CO_2 reduction, the band edges have to straddle a larger redox potential difference with carbon dioxide reduction to methane (CO_2/CH_4) at -3.79 eV and carbon dioxide reduction to methanol (CO_2/CH_3OH) at -3.65 eV. All these potentials and the positions of the band edges and band gaps are shown in **Figure 7.3**.

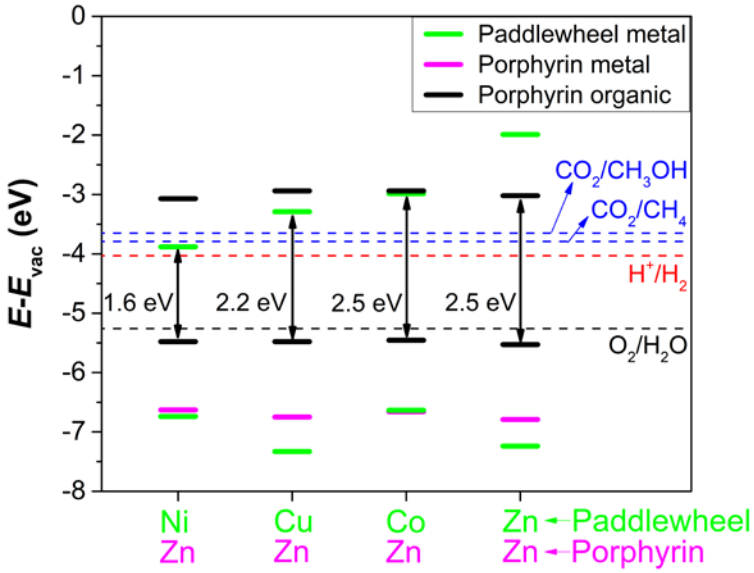

Figure 7.3. Band alignment of *M*-Zn-TCPP systems (*M* = Co^{2+}, Ni^{2+}, Cu^{2+} and Zn^{2+} is the metal in the paddlewheel). Levels from the paddlewheel metal, the porphyrin metal centre, and the organic part (C, N and H atoms) of porphyrins are shown in green, magenta and black, respectively. The energy levels of relevant half-reactions involved in water-splitting and CO_2 reduction to CH_4 and CH_3OH are also shown.

It is shown that the valence band, which is mainly contributed by the porphyrin unit, is approximately at -5.5 eV, is below the OER as required. The nature of the paddlewheel metal mainly affects the position of the conduction band edge. Whereas the lowest unoccupied molecular orbital (LUMO) of the porphyrin is always at the same energy (~-3 eV), the empty 3*d* levels of the paddlewheel transition metal centres can go below that value, lowering the band gap. For the Ni-Zn system, a lower-lying empty Ni 3*d* level narrows the band gap to 1.6 eV, where in the Co-Zn system, the lowest empty Co 3*d* level is at the same energy as the porphyrin's LUMO, so the band gap is not narrowed.

For water-splitting photocatalysis, the best metal in the paddlewheel is Cu, whose empty 3*d* levels bring the band gap to 2.2 eV. The Co-Zn system also has suitable band positions, albeit with a larger gap, which might be useful for photocatalytic CO_2 reduction reactions.

Taking the Cu-Zn system as reference, we can form a picture of how the photocatalytic water-splitting reaction could occur in a system like this. A water molecule would interact with the porphyrin unit (we have calculated an adsorption energy of -0.26 eV for water at the Zn-porphyrin in this MOF), where a photogenerated hole would drive the water oxidation reaction, evolving oxygen gas. A ligand-to-metal charge transfer (LCMT) would then have to take place, moving the excited electron from the excited levels of the porphyrin to the metal paddlewheel, where the reduction of protons would occur, driven by the high energy of the excited electron in the Cu 3*d* state.

TD-DFT calculations in the cluster model of the Cu-Zn-TCPP system, performed in collaboration with Crespo-Otero's group (Queen Mary University of London), confirm that the lowest-energy excitation (T_1) involves charge transfer from the porphyrin to the paddlewheel (**Appendix**: see **Table A1** for the list of excited states and **Table A2** for the relative charges of the porphyrin and paddlewheel units). However, this first excitation has zero oscillator strength, *i.e.* the charge transfer cannot be achieved via direct excitation. The lowest bright excitation (T_{44}) is a transition localised within the porphyrin unit, and corresponds to the so-called Soret band (or B band), which typically appears in the far visible or ultraviolet (UV) region of the spectrum [21, 60-62], as explained in **Chapter 1.2.2**. These calculations suggest two important limitations of these porphyrin-based MOFs in photocatalytic applications. First, most of the adsorption happens at energies in the far visible or UV range of the spectrum, so it would not be possible to take advantage of the energy from solar radiation, which lies in the visible region. Second, since the oscillator strength of the charge transfer is very low, we need to engineer the structure to make charge transfer more feasible. Therefore, in the next sections we will consider

possible modifications to theses MOFs, which could enhance their photocatalytic properties.

7.3.3 Effect of changing the metal from Zn to Co at the porphyrin centre

We now briefly consider the substitution of Zn by Co at the porphyrin centre, for which we have investigated the band positions in a system with Co at the centre of the porphyrin and Cu in the paddlewheel. The conduction band for this Cu-Co system is 0.3 eV below the porphyrin's LUMO, which is similar to what is observed for the Cu-Zn system (**Figure 7.4**).

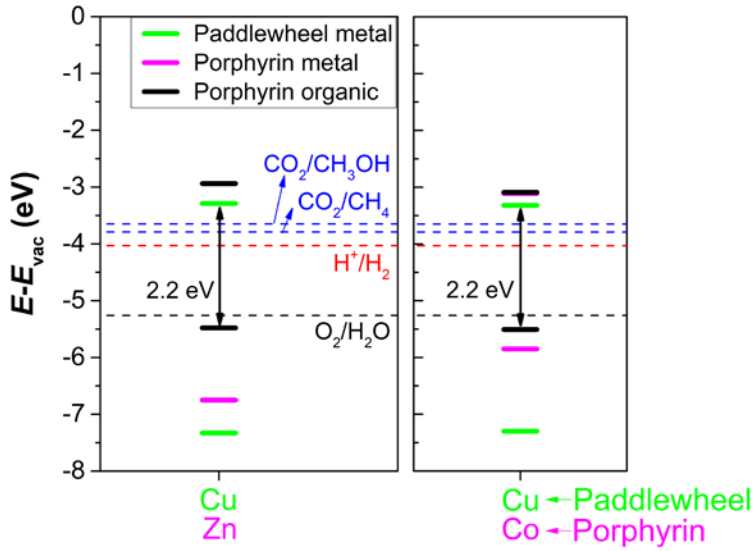

Figure 7.4. Comparison between band alignments of Cu-Zn-TCPP (left) and Cu-Co-TCPP (right) systems. The energy levels of the metal at paddlewheel, the metal at the porphyrin centre and organic part (C, N and H atoms) of porphyrins are shown in green, magenta and black, respectively. The energy levels of relevant half-reactions involved in water-splitting and CO_2 reduction to CH_4 and CH_3OH are also shown.

However, the highest filled 3*d* levels of the Co centres are significantly higher in energy than the highest filled 3*d* levels of Zn. The proximity between the high-lying filled Co 3*d* levels and the HOMO of the porphyrin will help stabilise a photogenerated hole, since the Co(II) centre can be readily oxidised to Co (III) (in contrast with the case of Zn, whose low-lying filled 3*d* levels prevent the oxidation). The presence of Co as a redox

centre in porphyrins has been widely used in the experimental design of porphyrin-based photocatalysts [63, 64].

Although Co-porphyrins seem more interesting for photocatalysis than Zn-porphyrins, in what follows we will consider other modifications of the porphyrin-based MOFs, while keeping the Zn at the porphyrin centre, for ease of calculations (the Co centres introduce additional magnetic degrees of freedom). The effect of other metal centres at the porphyrin on the electronic structure of porphyrin-based MOFs has been investigated in more detail in Ref. [29].

7.3.4 Effect of partially reducing porphyrin unit to chlorin

Until this point, we have explored substitutions of the metals at the paddlewheel and porphyrin units. Another route to modify the electronic properties and optical behaviour of these MOFs is to partially reduce the porphyrin unit to form chlorin. Chlorins fall in the generic class of hydroporphyrins, that is, porphyrin derivates in which one or more bonds are saturated by addition of hydrogen, resembling a photosynthetic chromophore found in nature [65]. It is known that chlorin exhibits stronger light absorption at lower energies compared to porphyrin [66]. Lu *et al.* have successfully synthesised chlorin-based MOFs that improve the photophysical properties of porphyrin-based MOFs for photodynamic therapy of colon cancers [67]. The motivation here is to study the increase of the light absorption of the MOF in the visible range to improve its photocatalytic efficiency.

The Cu-Zn-TCPP system was used as starting point, where one of the pyrrole rings was reduced by hydrogenation, as shown in **Figure 7.5**. After optimisation, this system exhibited negligible changes of cell parameters and geometry compared to the Cu-Zn-TCPP one. In this structure, because of the application of periodic boundary conditions, the position of the reduced pyrrole is ordered. However, using a 2×2×1

supercell, we have considered different relative positions of the reduced pyrrole in neighbouring chlorin units, and found that all configurations have similar energies (within 0.1 meV) and band gaps (within 0.05 eV).

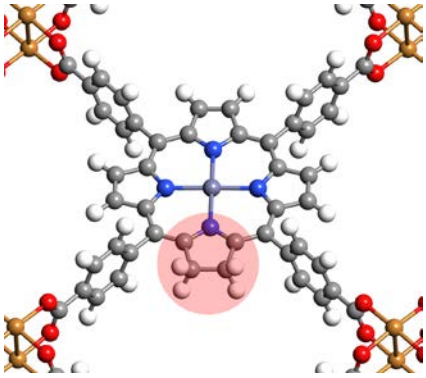

Figure 7.5. The Cu-Zn-Chlorin system: the Cβ atoms of the pink-shaded pyrrole are reduced. Colour code: grey = carbon, red = oxygen, white = hydrogen, blue = nitrogen and orange = copper.

The partial reduction leads to a narrower band gap (1.9 eV), but otherwise the electronic structure is similar to that of the unreduced Cu-Zn-TCPP system (**Figure 7.6**). Although the valence band is now slightly above the OER level, it is possible in practical applications to realign such small differences using a bias voltage [29, 30].

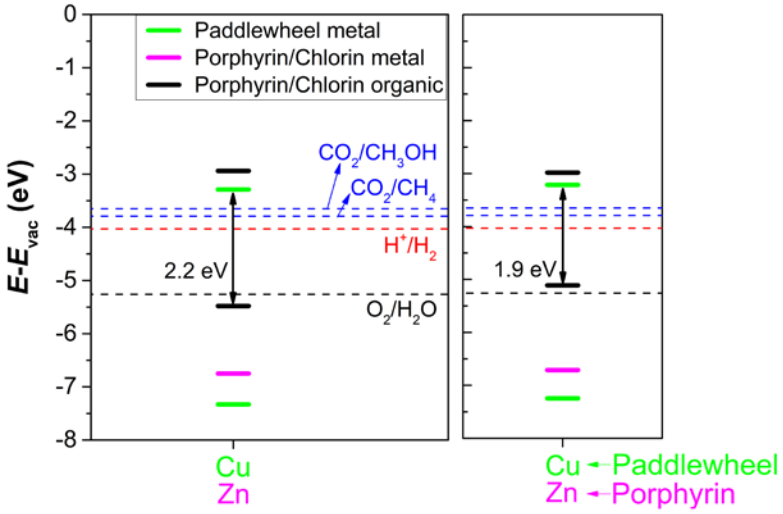

Figure 7.6. Comparison between band alignments of Cu-Zn-TCPP (left) and Cu-Zn-chlorin (right) systems. The bands of metal at paddlewheel, metal at the centre and organic part (C, N and H atoms) of porphyrins are shown in green, magenta and black, respectively. The energy levels of relevant half-reactions involved in water-splitting and CO_2 reduction to CH_4 and CH_3OH are also shown.

Excited states calculations were performed by our collaborators (Crespo-Otero's group at Queen Mary University of London) for these Cu-Zn-chlorin systems (energies of all calculated states and Bader charges of selected. States are listed in **Tables A3** and **A4** of **Appendix**). The first excited state (T_1), as in the unmodified porphyrin system, is a charge-transfer state, but with zero oscillator strength. The Soret band is also found at roughly the same energy in the porphyrin- and chlorin-based MOFs. However, the chlorin-based MOF has relatively bright state at lower energies (T_{16} at 2.3 eV) which is not present in the porphyrin-based system. This is consistent with previous work showing that chlorin increases light absorption in the lower-energy Q bands, thus improving photophysical behaviour under visible light [66, 67]. This is clearly observed in the absorption spectra of the cluster model of the Cu-Zn-chlorin system (**Figure 7.7**), which shows the presence of a peak in the visible range. This peak corresponds to the Q bands, which in the case of the unreduced Cu-Zn-TCPP system is still appreciable but is has a very small intensity.

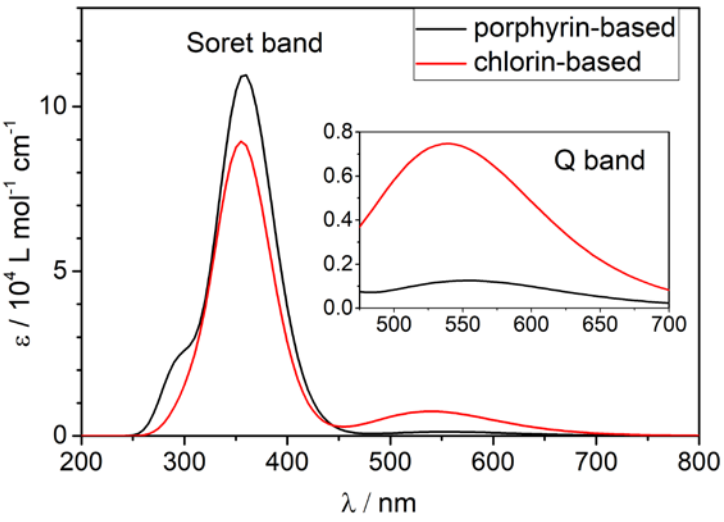

Figure 7.7. Light absorption spectra calculated using TD-DFT for the cluster models of the porphyrin-based (Cu-Zn-TCPP) and chlorin-based (Cu-Zn-chlorin) systems. The inset expands the spectrum in the region of the Q band.

All these results suggests that the partial reduction of porphyrin to chlorin units in these and MOFs could enhance the photocatalytic performance under visible light, but to the best of our knowledge this avenue has not been experimentally explored.

7.3.5 Changing the bridge between the porphyrin and paddlewheel

Finally, we consider the effect of modifying the bridging species between the porphyrin and the paddlewheel units. We investigate the substitution of the benzene rings by ethyne (C2) or butadiyne (C4) bridges (**Figure 7.8**). We have shown in previous work that it is possible to modify the properties of porphyrin-based structures by varying the nature of the bridging species linking the porphyrin, and in this way tune the band gap values [68].

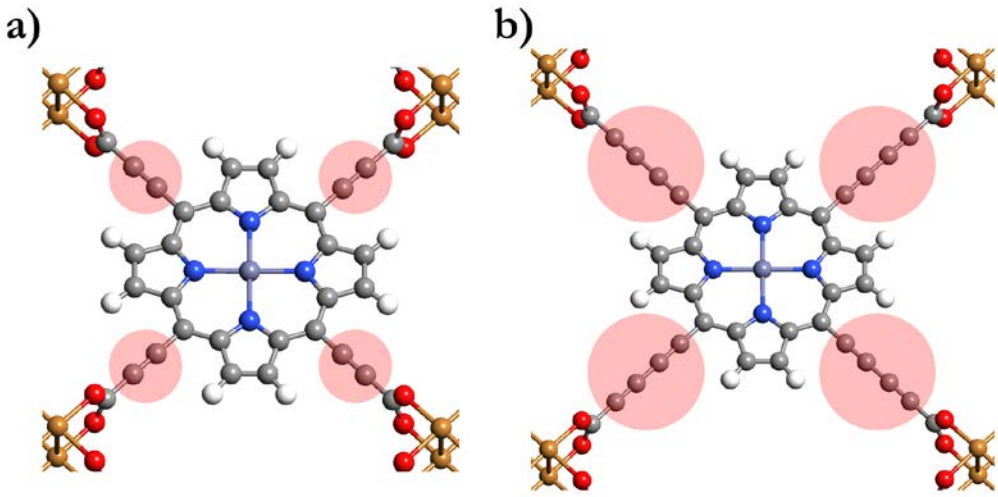

Figure 7.8. The two bridge-substituted systems: a) Cu-Zn-C2 and b) Cu-Zn-C4. The benzene ring has been substituted by the ethyne and butadiyne bridges, respectively, highlighted by pink-shaded circles. Colour code: grey = carbon, red = oxygen, white = hydrogen, blue = nitrogen and orange = copper.

The substitution of the benzene rings by C2 and C4 bridges induce significant narrowing of the band gaps (with values of 1.8 eV and 1.7 eV for C2 and C4, respectively) compared with the 2.2 eV value for the Cu-Zn-TCPP system (**Figure 7.9**). The gap narrowing is achieved mainly as consequence of the lowering of the conduction bands, since the valence bands are almost unaltered, going only slightly down in energy.

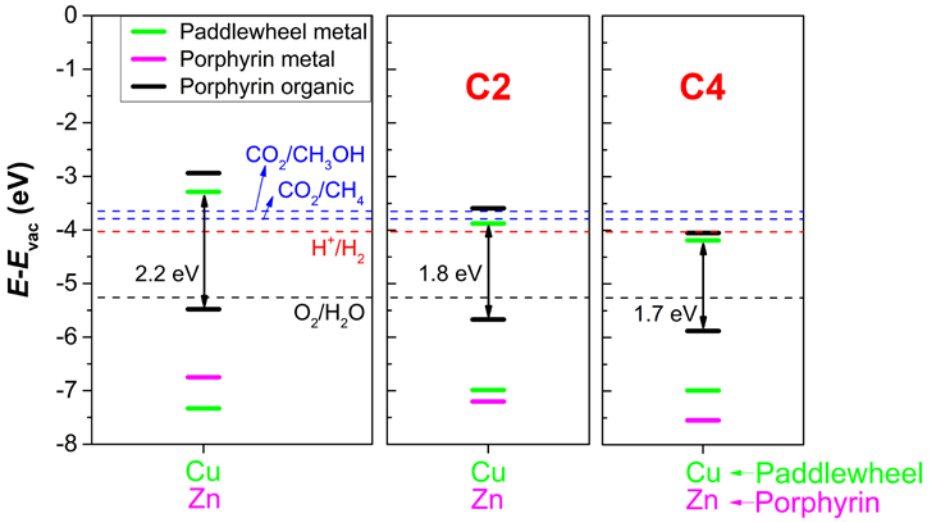

Figure 7.9. Comparison between band alignments of Cu-Zn-TCPP (left), Cu-Zn-C2 (middle) and -C4 (right) systems. The bands of metal at paddlewheel, metal at the centre and organic atoms of porphyrins (C, N and H) are shown in green, magenta and black, respectively. The energy levels of relevant half-reactions involved in water-splitting and CO_2 reduction to CH_4 and CH_3OH are also shown.

It is interesting to discuss the effect of the different bridges on the charge transfer. The excited state calculations (performed by our collaborators) for the system with C2 bridge show that there are now several relatively bright states involving charge transfer from the porphyrin to the paddlewheel (see **Tables A5** and **A6** in **Appendix**). Bright states T_{30}, T_{34}, and T_{36}, which are at energies in the region of the Soret band, now involve significant charge transfer from the porphyrin to the paddlewheel. This effect would lead to direct charge transfer separation via light absorption and could potentially be beneficial for the photocatalytic behaviour of the system. Modifying the nature and length of the bridging units between the porphyrin and the metal cluster is thus the key to tune the charge transfer behaviour.

The length of the bridging unit can also be expected to modify LMCT behaviour from excited states localised in the porphyrin. To illustrate this, we present here a simple model based on Marcus theory [69, 70], where we consider the porphyrin and the paddlewheel as two separate fragments. When light is absorbed at the bright states of the porphyrin, before any charge transfer takes place, the excitation will decay to the first

excited state of the porphyrin (Kasha's rule). We make use of Marcus theory to describe the electron transfer between the excited porphyrin fragment (donor) and the paddlewheel fragment (acceptor). To consider the electrostatic interactions between the charged fragments (porphyrin$^+$ and paddlewheel$^-$), we have simply added a classical electrostatic term to the energy of the charge transfer state, considering the distance between these fragments (and assuming a full electron transfer).

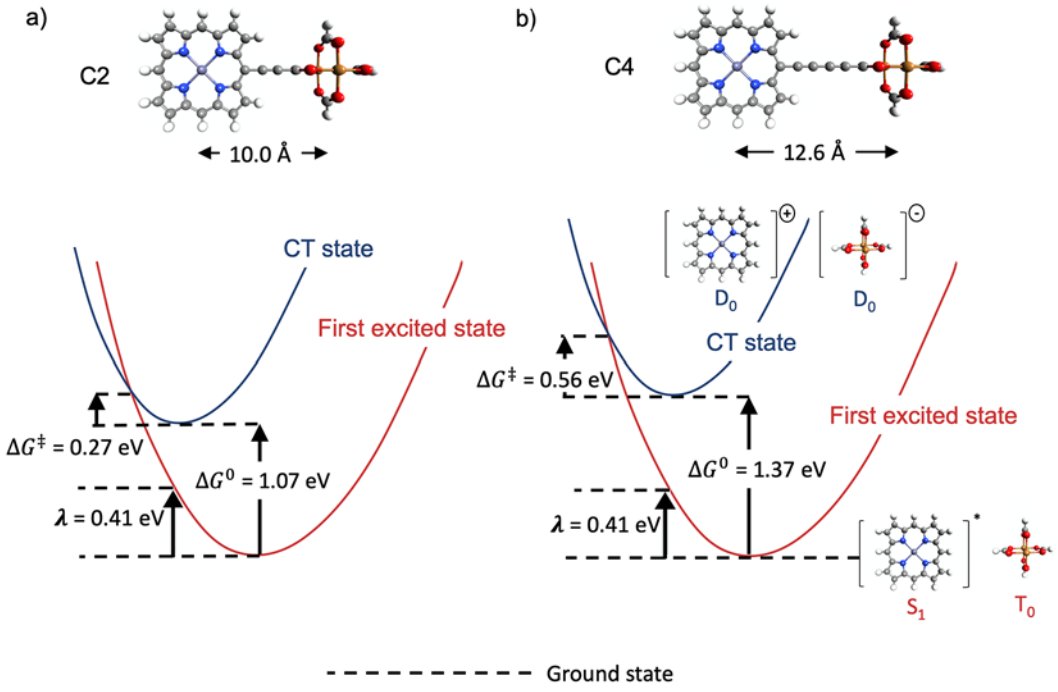

Figure 7.10. Marcus parabolas and energy levels showing the transfer process in a) the C2 bridge and b) the C4 bridge. The excited state is shown in red and the charge-transfer state in blue.

In our model calculations, we find that the charge-transfer state is always above the first excited state ($\Delta G^0 > 0$). In this case, the barrier (with respect to the charge-transfer state) is given by $\Delta G^{\ddagger} = (\Delta G^0 - \lambda)^2/4\lambda$, where λ is the reorganisation energy (the change in energy of the first excited state when moved to the geometry of the charge-transfer state, which in this simple model is independent of the length of the bridging unit). The energy of the charge-transfer state, and then the value of ΔG^0, is 0.3 eV lower for the C2 bridge than that for the C4 bridge, due to the stronger electrostatic

attraction for the shorter bridge. This means that in the C2 system the kinetic barrier to go from state to the other will also be lower, as shown in **Figure 7.10**. Our analysis suggests that the introduction of shorter bridging units between the porphyrin and the metal clusters should lower the kinetic barriers for the LMCT process. This is consistent with the experimental work from Lan *et al.* [26], who concluded that electron transfer from the photoexcited porphyrins to Ru clusters was facilitated by the proximity of the Ru cluster to the porphyrin in their MOF.

7.4 Conclusions

We have presented a computer simulation of two-dimensional, porphyrin(chlorin)-based MOFs, consisting of metalloporphyrin units (with Zn^{2+} or Co^{2+} at the centre) and metal paddlewheel clusters (made of Co^{2+}, Ni^{2+}, Cu^{2+} or Zn^{2+}), bridged by different organic linear chains. Our results illustrate several ways in which the electronic and optical properties of these MOFs can be modified by the different composition or structural degrees of freedom. Changing the metal in the paddlewheel cluster from Zn to Co, Cu, or Ni, lowers the position of the empty 3*d* levels in that order. For Cu and Ni, the empty 3*d* levels are slightly below the LUMO of the porphyrin, which is convenient to achieve charge separation via linker to metal charge transfer (LCMT). The copper paddlewheel seems ideal for water-splitting photocatalysis in terms of the resulting band gap and relative position of empty levels. Changing the metal at the centre of the porphyrin from Zn to Co does not change of the band edges or the band gap, but creates an easy redox centre capable of stabilising the photogenerated hole at the porphyrin.

Perhaps even more important than engineering the band alignment and gap, is to enhance the visible light absorption and to facilitate charge separation in the framework. To address the first issue, we consider the partial reduction of porphyrin to chlorin in the MOF, which we demonstrate leads to stronger adsorption in the visible range of the

spectrum. Charge separation, on the other hand, is found to be sensitive to the nature and length of the bridging units between the porphyrin and the paddlewheel. For example, using an ethyne bridge (C2) introduces charge-transfer bright states in the energy region of the Soret band. Finally, we used a simple model based on Marcus theory to illustrate that the energy barriers to the LMCT process can be expected to decrease with the length of the bridge. Overall, our study suggests different avenues to modify porphyrin-based MOFs to improve their photocatalytic performance in applications such as water-splitting and CO_2 reduction.

7.5 References

1. Zhou, H.C., J.R. Long, and O.M. Yaghi, *Introduction to Metal–Organic Frameworks.* Chemical Reviews, 2012. **112**(2): p. 673-674.
2. Zhu, G., et al., *Porphyrin-based porous sheet: Optoelectronic properties and hydrogen storage.* International Journal of Hydrogen Energy, 2015. **40**(9): p. 3689-3696.
3. Ma, S. and H.-C. Zhou, *Gas storage in porous metal–organic frameworks for clean energy applications.* Chemical Communications, 2010. **46**(1): p. 44-53.
4. Li, B., et al., *Porous Metal–Organic Frameworks for Gas Storage and Separation: What, How, and Why?* The Journal of Physical Chemistry Letters, 2014. **5**(20): p. 3468-3479.
5. Li, H., et al., *Recent advances in gas storage and separation using metal–organic frameworks.* Materials Today, 2018. **21**(2): p. 108-121.
6. Li, H., et al., *Porous metal-organic frameworks for gas storage and separation: Status and challenges.* EnergyChem, 2019. **1**(1): p. 100006.
7. Wang, J.-L., C. Wang, and W. Lin, *Metal–Organic Frameworks for Light Harvesting and Photocatalysis.* ACS Catalysis, 2012. **2**(12): p. 2630-2640.

8. Santaclara, J.G., et al., *Understanding metal–organic frameworks for photocatalytic solar fuel production.* CrystEngComm, 2017. **19**(29): p. 4118-4125.

9. Wang, Q., et al., *Recent advances in MOF-based photocatalysis: environmental remediation under visible light.* Inorganic Chemistry Frontiers, 2020. **7**(2): p. 300-339.

10. Fu, Y., et al., *An Amine-Functionalized Titanium Metal–Organic Framework Photocatalyst with Visible-Light-Induced Activity for CO2 Reduction.* Angewandte Chemie International Edition, 2012. **51**(14): p. 3364-3367.

11. Hendon, C.H., et al., *Engineering the Optical Response of the Titanium-MIL-125 Metal–Organic Framework through Ligand Functionalization.* Journal of the American Chemical Society, 2013. **135**(30): p. 10942-10945.

12. Hendrickx, K., et al., *Understanding Intrinsic Light Absorption Properties of UiO-66 Frameworks: A Combined Theoretical and Experimental Study.* Inorganic Chemistry, 2015. **54**(22): p. 10701-10710.

13. Abednatanzi, S., et al., *Mixed-metal metal–organic frameworks.* Chemical Society Reviews, 2019. **48**(9): p. 2535-2565.

14. Li, R., et al., *Nickel-substituted zeolitic imidazolate frameworks for time-resolved alcohol sensing and photocatalysis under visible light.* Journal of Materials Chemistry A, 2014. **2**(16): p. 5724-5729.

15. Goh, T.W., et al., *Utilizing mixed-linker zirconium based metal-organic frameworks to enhance the visible light photocatalytic oxidation of alcohol.* Chemical Engineering Science, 2015. **124**: p. 45-51.

16. Grau-Crespo, R., et al., *Modelling a Linker Mix-and-Match Approach for Controlling the Optical Excitation Gaps and Band Alignment of Zeolitic Imidazolate Frameworks.* Angewandte Chemie International Edition, 2016. **55**(52): p. 16012-16016.

17. Yang, Q., Q. Xu, and H.-L. Jiang, *Metal–organic frameworks meet metal nanoparticles: synergistic effect for enhanced catalysis.* Chemical Society Reviews, 2017. **46**(15): p. 4774-4808.

18. Fang, X., et al., *Single Pt Atoms Confined into a Metal–Organic Framework for Efficient Photocatalysis.* Advanced Materials, 2018. **30**(7): p. 1705112.

19. Fateeva, A., et al., *A Water-Stable Porphyrin-Based Metal–Organic Framework Active for Visible-Light Photocatalysis.* Angewandte Chemie International Edition, 2012. **51**(30): p. 7440-7444.

20. Wang, X., et al., *An ultrathin porphyrin-based metal-organic framework for efficient photocatalytic hydrogen evolution under visible light.* Nano Energy, 2019. **62**: p. 250-258.

21. Giovannetti, R., *The use of spectrophotometry UV–vis for the study of porphyrins.* InTechOpen, 2012. **Macro To Nano Spectroscopy**.

22. Lu, Q., et al., *2D Transition-Metal-Dichalcogenide-Nanosheet-Based Composites for Photocatalytic and Electrocatalytic Hydrogen Evolution Reactions.* Advanced Materials, 2015. **28**(10): p. 1917-1933.

23. Paschenko, V.Z., et al., *Excitation energy transfer in covalently bonded porphyrin heterodimers.* Optics and Spectroscopy, 2012. **112**(4): p. 519-527.

24. Sasan, K., et al., *Incorporation of iron hydrogenase active sites into a highly stable metal–organic framework for photocatalytic hydrogen generation.* Chemical Communications, 2014. **50**(72): p. 10390-10393.

25. Leng, F., et al., *Boosting Photocatalytic Hydrogen Production of Porphyrinic MOFs: The Metal Location in Metalloporphyrin Matters.* ACS Catalysis, 2018. **8**(5): p. 4583-4590.

26. Lan, G., et al., *Electron Injection from Photoexcited Metal–Organic Framework Ligands to Ru2 Secondary Building Units for Visible-Light-Driven Hydrogen Evolution.* Journal of the American Chemical Society, 2018. **140**(16): p. 5326-5329.

27. Jiang, Z.W., et al., *Controllable Synthesis of Porphyrin-Based 2D Lanthanide Metal–Organic Frameworks with Thickness- and Metal-Node-Dependent Photocatalytic Performance.* Angewandte Chemie International Edition, 2020. **59**(8): p. 3300-3306.

28. Mancuso, J.L., et al., *Electronic Structure Modeling of Metal–Organic Frameworks.* Chemical Reviews, 2020. **120**(16): p. 8641-8715.

29. Hamad, S., et al., *Electronic structure of porphyrin-based metal–organic frameworks and their suitability for solar fuel production photocatalysis.* Journal of Materials Chemistry A, 2015. **3**(46): p. 23458-23465.

30. Aziz, A., et al., *Porphyrin-based metal-organic frameworks for solar fuel synthesis photocatalysis: band gap tuning via iron substitutions.* Journal of Materials Chemistry A, 2017. **5**(23): p. 11894-11904.

31. Chung, H., et al., *Structural Variation in Porphyrin Pillared Homologous Series: Influence of Distinct Coordination Centers for Pillars on Framework Topology.* Crystal Growth & Design, 2009. **9**(7): p. 3327-3332.

32. Choi, E.-Y., et al., *Highly tunable metal–organic frameworks with open metal centers.* CrystEngComm, 2009. **11**(4): p. 553-555.

33. Zhao, M., et al., *Ultrathin 2D Metal–Organic Framework Nanosheets.* Advanced Materials, 2015. **27**(45): p. 7372-7378.

34. Zhao, M., et al., *Two-Dimensional Metal–Organic Framework Nanosheets.* Small Methods, 2017. **1**(1-2): p. 1600030.

35. Spoerke, E.D., et al., *MOF-Sensitized Solar Cells Enabled by a Pillared Porphyrin Framework.* The Journal of Physical Chemistry C, 2017. **121**(9): p. 4816-4824.

36. Tan, K., et al., *Stability and Hydrolyzation of Metal Organic Frameworks with Paddle-Wheel SBUs upon Hydration.* Chemistry of Materials, 2012. **24**(16): p. 3153-3167.

37. Chen, Y., et al., *A Copper(II)-Paddlewheel Metal–Organic Framework with Exceptional Hydrolytic Stability and Selective Adsorption and Detection Ability of Aniline in Water*. ACS Applied Materials & Interfaces, 2017. **9**(32): p. 27027-27035.

38. Liu, B., et al., *Critical role of water stability in metal–organic frameworks and advanced modification strategies for the extension of their applicability*. Environmental Science: Nano, 2020. **7**(5): p. 1319-1347.

39. Ding, M., X. Cai, and H.-L. Jiang, *Improving MOF stability: approaches and applications*. Chemical Science, 2019. **10**(44): p. 10209-10230.

40. Kresse, G., Furthmüller, J., *Efficient iterative schemes for ab initio total-energy calculations using a plane-wave basis set*. Phys. Rev. B: Condens. Matter Mater. Phys., 1996. **54**(16): p. 11169 - 11186.

41. Kresse, G., Furthmüller, J., *Efficiency of ab-initio total energy calculations for metals and semiconductors using a plane-wave basis set*. Comput. Mater. Sci., 1996. **6**: p. 15 - 50.

42. Perdew, J.P., K. Burke, and M. Ernzerhof, *Generalized Gradient Approximation Made Simple*. Physical Review Letters, 1996. **77**(18): p. 3865-3868.

43. Perdew, J.P., K. Burke, and M. Ernzerhof, *Generalized Gradient Approximation Made Simple [Phys. Rev. Lett. 77, 3865 (1996)]*. Physical Review Letters, 1997. **78**(7): p. 1396-1396.

44. Wang, L., T. Maxisch, and G. Ceder, *Oxidation energies of transition metal oxides within the GGA+U framework*. Physical Review B, 2006. **73**(19): p. 195107.

45. Grimme, S., *Semiempirical GGA-type density functional constructed with a long-range dispersion correction*. Journal of Computational Chemistry, 2006. **27**(15): p. 1787-1799.

46. Blöchl, P.E., *Projector augmented-wave method*. Phys. Rev. B, 1994. **50**(24): p. 17953-17979.

47. Kresse, G. and D. Joubert, *From ultrasoft pseudopotentials to the projector augmented-wave method*. Phys. Rev. B, 1999. **59**(3): p. 1758-1775.

48. Heyd, J., G.E. Scuseria, and M. Ernzerhof, *Hybrid functionals based on a screened Coulomb potential*. The Journal of Chemical Physics, 2003. **118**(18): p. 8207-8215.

49. Heyd, J., G.E. Scuseria, and M. Ernzerhof, *Erratum: "Hybrid functionals based on a screened Coulomb potential" [J. Chem. Phys. 118, 8207 (2003)]*. The Journal of Chemical Physics, 2006. **124**(21): p. 219906.

50. Butler, K.T., C.H. Hendon, and A. Walsh, *Electronic Chemical Potentials of Porous Metal–Organic Frameworks*. Journal of the American Chemical Society, 2014. **136**(7): p. 2703-2706.

51. Frisch, M.J., et al., *Gaussian 16 Rev. C.01*. 2016: Wallingford, CT.

52. Johnston, L.L., et al., *Copper benzenedicarboxylate coordination polymers incorporating a long-spanning neutral co-ligand: Effect of anion inclusion and carboxylate pendant-arm length on topology and magnetism*. Polyhedron, 2010. **29**(1): p. 303-311.

53. Pang, Y., et al., *Copper(II) and nickel(II) coordination polymers assembled from 2,4-dibenzoylisophthalic acid and different N-donor co-ligands: syntheses, crystal structures, and magnetic properties*. CrystEngComm, 2011. **13**(16): p. 5142-5151.

54. Zhao, J., et al., *Two (3,6)-connected porous metal–organic frameworks based on linear trinuclear $[Co_3(COO)_6]$ and paddlewheel dinuclear $[Cu_2(COO)_4]$ SBUs: gas adsorption, photocatalytic behaviour, and magnetic properties*. Journal of Materials Chemistry A, 2015. **3**(13): p. 6962-6969.

55. Rodríguez-Fortea, A., et al., *Exchange Coupling in Carboxylato-Bridged Dinuclear Copper(II) Compounds: A Density Functional Study*. Chemistry – A European Journal, 2001. **7**(3): p. 627-637.

56. Pakula, R.J. and J.F. Berry, *Cobalt complexes of the chelating dicarboxylate ligand "esp": a paddlewheel-type dimer and a heptanuclear coordination cluster.* Dalton Transactions, 2018. **47**(39): p. 13887-13893.

57. Williams, D.E., et al., *Energy Transfer on Demand: Photoswitch-Directed Behavior of Metal–Porphyrin Frameworks.* Journal of the American Chemical Society, 2014. **136**(34): p. 11886-11889.

58. Shannon, R.D., *Revised effective ionic radii and systematic studies of interatomic distances in halides and chalcogenides.* Acta Crystallographica Section A, 1976. **32**(5): p. 751-767.

59. Stavale, F. and J. Simmchen, *Artificial Photosynthesis Inspired by PSII: Water Splitting on Heterogeneous Photocatalysts*, in *Encyclopedia of Interfacial Chemistry*, K. Wandelt, Editor. 2018, Elsevier: Oxford. p. 327-333.

60. Yang, R., et al., *A Selective Optode Membrane for Histidine Based on Fluorescence Enhancement of Meso−Meso-Linked Porphyrin Dimer.* Analytical Chemistry, 2002. **74**(5): p. 1088-1096.

61. Gulino, A., et al., *Optical pH Meter by Means of a Porphyrin Monolayer Covalently Assembled on a Molecularly Engineered Silica Surface.* Chemistry of Materials, 2005. **17**(16): p. 4043-4045.

62. Di Natale, C., et al., *Porphyrins-based opto-electronic nose for volatile compounds detection.* Sensors and Actuators B: Chemical, 2000. **65**(1): p. 220-226.

63. Hong, Y.H., et al., *Photocatalytic Oxygenation Reactions with a Cobalt Porphyrin Complex Using Water as an Oxygen Source and Dioxygen as an Oxidant.* Journal of the American Chemical Society, 2019. **141**(23): p. 9155-9159.

64. Call, A., et al., *Highly Efficient and Selective Photocatalytic CO2 Reduction to CO in Water by a Cobalt Porphyrin Molecular Catalyst.* ACS Catalysis, 2019. **9**(6): p. 4867-4874.

65. Barkigia, K.M., et al., *Models of photosynthetic chromophores: molecular structure of the bacteriochlorin (2,3,12,13-tetrahydro-5,10,15,20-tetraphenylporphinato)(pyridine)zinc(II).* Inorganic Chemistry, 1991. **30**(9): p. 2233-2236.

66. Palma, M., G.I. Cárdenas-Jirón, and M.I. Menéndez Rodríguez, *Effect of Chlorin Structure on Theoretical Electronic Absorption Spectra and on the Energy Released by Porphyrin-Based Photosensitizers.* The Journal of Physical Chemistry A, 2008. **112**(51): p. 13574-13583.

67. Lu, K., C. He, and W. Lin, *A Chlorin-Based Nanoscale Metal–Organic Framework for Photodynamic Therapy of Colon Cancers.* Journal of the American Chemical Society, 2015. **137**(24): p. 7600-7603.

68. Posligua, V., et al., *Band Structures of Periodic Porphyrin Nanostructures.* The Journal of Physical Chemistry C, 2018. **122**(41): p. 23790-23798.

69. Marcus, R.A., *Electron transfer reactions in chemistry. Theory and experiment.* Reviews of Modern Physics, 1993. **65**(3): p. 599-610.

70. Marcus, R.A., *On the Theory of Oxidation - Reduction Reactions Involving Electron Transfer. I.* The Journal of Chemical Physics, 1956. **24**(5): p. 966-978.

8 Adsorption of porphyrin molecules at the surface and edge of graphene and in-plane porphyrin-graphene heterostructures

In this Chapter, graphitic structures with Zn-porphyrin units adsorbed or decorating the edges were investigated in terms of their interactions to understand their structural and electronic properties. Through a systematic investigation of the possible positions of porphyrin units on top of the surface of graphene, we have analysed the strength of the interaction and the diffusion barriers. We show that porphyrin should be capable of diffusing easily and therefore reach the edges of graphene, where it adsorbs more strongly, which could be useful for photocatalytic applications. Also, this could enable the embedding of porphyrin units in the graphene matrix during graphene growth and thus create not just an edge-modified graphene, but also intrasheet functionalisation which could be potential catalysts for CO_2 and CO reduction, as has been already reported in Ref. [1].

8.1 Introduction

The properties of graphene, arising from its two-dimensional (2D) sp^2 hybridised carbon lattice, make it an enticing material for developing novel carbon-based electronics and a

formidable playground to explore fundamental solid state physics [2, 3]. Due to its excellent electronic conductivity, mechanical properties and large specific surface area, graphene is considered as a suitable component in devices for solar energy conversion, including artificial photosynthesis and photovoltaic applications [4-6].

On the other hand, the interaction of graphitic nanostructures with porphyrin-based systems has become a hot topic since it can realise the combination of the conductive properties of graphene sheets with light-absorbing and other functional properties of the porphyrins [7, 8]. Porphyrins are stable functional dyes with large extinction coefficients in the visible light region and photochemical electron transfer ability, therefore their presence in graphene could enhance their usage as photoactive materials. There is evidence that porphyrins can interact with carbon materials, such as graphite, fullerenes and carbon nanotubes through π-π interactions that take place between their electron-abundant aromatic cores and conjugated surfaces of the carbon materials, making them photoactive [9-11]. It is known that π-π interactions exist between graphene and porphyrins since Geng *et al.* [11] reported an efficient method for preparations of high-quality graphene via porphyrin exfoliation of graphite, taking advantage of those interactions. Using UV-visible spectroscopy, they found that the Soret band of the porphyrins is reduced and Q bands are shifted to greater wavelengths as the result of the π-π interactions with graphene.

In previous chapters of this thesis, we have considered the properties of graphitic and porphyrinic structures separately. In this Chapter, we theoretically investigate a range of arrays including adsorbed porphyrin molecules on top of graphene and also at the interface of the zigzag edges of graphene nanoribbon, in order to predict their structural and electronic properties in terms of their interactions and evaluate their photocatalytic applications.

8.2 Computational methods

All calculations are executed using density functional theory (DFT), as implemented in the VASP code [12, 13]. We employed the generalised gradient approximation (GGA) for the exchange-correlation functional, in particular a dispersion-corrected Perdew-Burke-Ernzerhof functional (PBE+D3) [14, 15]. As VASP uses three-dimensional (3D) periodic boundary conditions, vacuum regions of at least 10 Å were considered between the nanostructures, to minimise the interaction with periodic images.

The projector-augmented wave (PAW) method [16] is used to describe the ion-electron interactions, and a planewave basis set with a kinetic cutoff energy as 520 eV is adopted to expand the Kohn-Sham orbitals for all calculations. The Brillouin zone is sampled by adopting a Γ-centred *k*-point mesh with an equivalent *k*-spacing of 0.2 $Å^{-1}$. These calculations have been tested for convergence with respect to the kinetic cutoff energy and *k*-point grid. Geometry optimisations were performed unit all forces were less than 0.01 eV $Å^{-1}$.

Electron energies are reported with respect to the vacuum reference since, as in most of periodic DFT codes, VASP energies are given with respect to an internal energy reference. Therefore, to obtain absolute energy levels it was necessary to evaluate the electrostatical potential in the pseudo-vacuum region represented by the empty space within the simulation cell, with zero potential gradient. This was chosen as a planar average in the vacuum gap between 2D graphene and graphene nanoribbons, employing the MacroDensity code [17].

8.3 Results and discussion

8.3.1 Adsorption of porphyrin molecule on graphene

We considered a graphene nanosheet which each unit cell includes 288 carbon atoms. The reason to select a large system is to avoid interactions between the porphyrin molecules. The optimised C-C bond length in graphene was 1.425 Å, which agrees with previous reports [18].

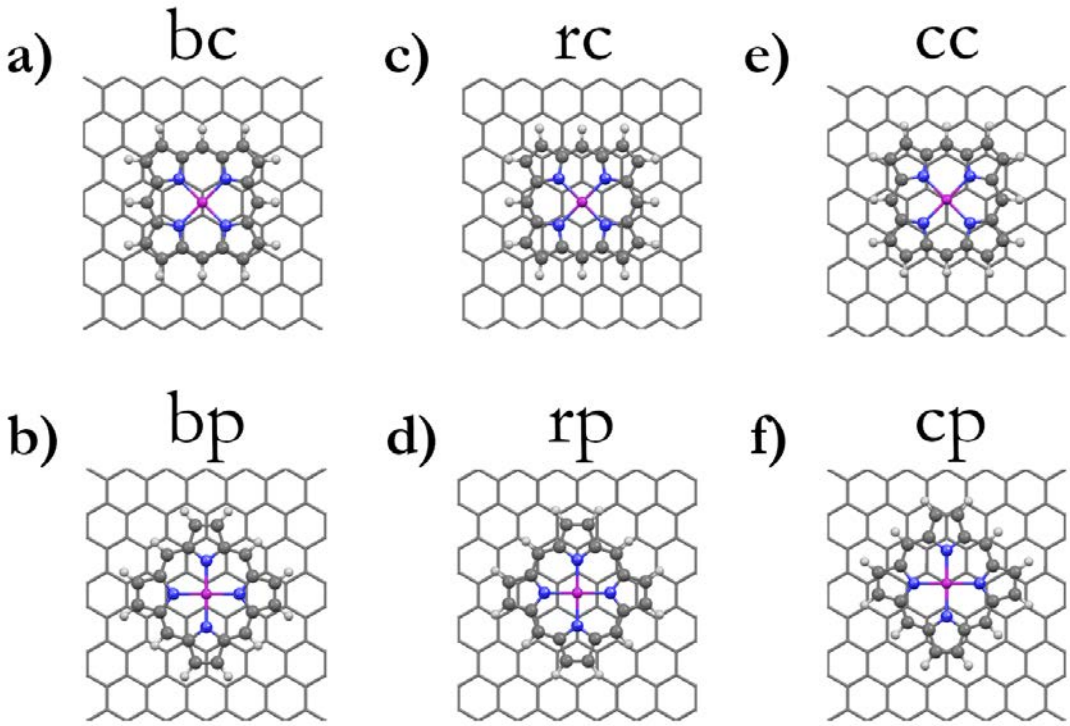

Figure 8.1. Positions of porphyrin adsorbed on graphene surface: a) bond-crossed (bc), b) bond-parallel (bp), c) ring-crossed (rc), d) ring-parallel (rp), e) carbon-crossed (cc) and f) carbon-parallel (cp). Colour code: grey = carbon, white = hydrogen, blue = nitrogen and purple = zinc.

The optimised porphyrin molecule was placed on top of graphene considering six different positions (**Figure 8.1**), which are bond-crossed (bc), bond-parallel (bp), ring-crossed (rc), ring-parallel (rp), carbon-crossed (cc) and carbon-parallel (cp). The bond-centred positions take the centre of the porphyrin unit lying above a C-C bond, whereas the ring-centred and carbon-centred ones take the metallic centre lying in the

middle of a graphene ring and on a carbon atom, respectively. The terms 'crossed' and 'parallel' refer to the position that the C-N bonds take when the porphyrin is rotated 45º on the z-axis. The 'crossed' ones (**Figure 8.1a**, **c** and **e**) form a cross within the C-N bonds and the 'parallel' positions (**Figure 8.1b**, **d** and **f**) have their C-N bonds parallel to the edges of the unit cell.

In all of these positions, the starting distance between the centre of the molecule and the graphene surface was 3.47 Å, reported by Pham *et al.* as the optimal in similar hybrid systems [3]. After relaxation, bp, cc and cp positions showed that distances *d* have minimal variations (~0.03 Å in average) compared with the optimal one. In **Table 8.1**, we can see that the position bp is the most stable position at graphene surface, which agrees with the results of Pham *et al.*, where they showed that a tetraphenyl metal-free porphyrin is adsorbed at graphene with its centre lying above a C-C bond [3].

Also, these three positions (bp, cc and cp) exhibited the highest adsorption energy (E_{ads}) among all, having values of about -1.4 eV (see **Table 8.1**). These results lead us to think that E_{ads} values obtained are a function of the distance between porphyrin units and graphene (higher E_{ads} when *d* decreases and vice versa), therefore the position which porphyrins adopt on the graphene surface is crucial to obtain an ideal adsorption. Although these results suggest that the porphyrin molecules would try to resemble a similar geometry between them, it should be noted that these three positions (bp, cc and cp) were not altered after relaxation, staying flat in the same initial orientation without any rotation.

Following this idea, in **Table 8.1** we can see that distances obtained in positions rp, bc and rc increase (~ 0.1 Å compared with the optimal distance), having lower E_{ads} values which confirms our latter assumption (higher E_{ads} when *d* decreases and lower E_{ads} when *d* increases). In term of E_{ads}, we have the following ascending order: bp < cc < cp < rp < bc < rc. Distances follow the same trend, except for bc position and the reason could

be related to the interaction of nitrogen atoms within the porphyrin unit with carbon atoms of graphene surface.

Table 8.1. Distances (*d*) between graphene surface and the metal centre of porphyrin, adsorption energies (E_{ads}) and relative stabilities calculated for each position.

Position	*d* (Å)	E_{ads} (eV)	Relative stability (meV)
bp	3.490	-1.469	0.0
cc	3.499	-1.459	9.4
cp	3.503	-1.454	14.7
rp	3.568	-1.427	42.0
bc	3.522	-1.413	55.5
rc	3.590	-1.410	58.3

Comparing their total energies, the bp is the most stable position by ~30 meV in average, among all considered positions whose relative stability values also follow the same trend displayed by E_{ads}. This is in agreement with Pham *et al.*, where they showed that a tetraphenyl metal-free porphyrin is physisorbed at graphene with its centre lying above a C-C bond [3]. This calculated energy is thus due to dispersion and to the electrostatic interaction coming from the charge redistribution on the graphene induced by the polar bonds of the porphyrin molecule.

8.3.2 Porphyrin molecule diffusion

In order to analyse the barrier of diffusion of porphyrin on graphene, the nudged elastic band (NEB) method was employed to find the minimum energy path (MEP) considering the bc, bp, cc and cp positions.

In this method, the constrained optimisation is done by adding spring forces along the band between images and by projecting out the component of the force due to the potential perpendicular to the band [19]. The MEP consists of six intermediate images between the optimal initial and final geometries already calculated, as illustrated in **Figure 8.2 – left** (porphyrin moves from a C-C bond in the graphene surface to an adjacent

parallel C-C bond for the bond-centred positions, and for the carbon-centred positions the porphyrin moves from a C atom towards an adjacent parallel C atom, considering the metal centre as reference).

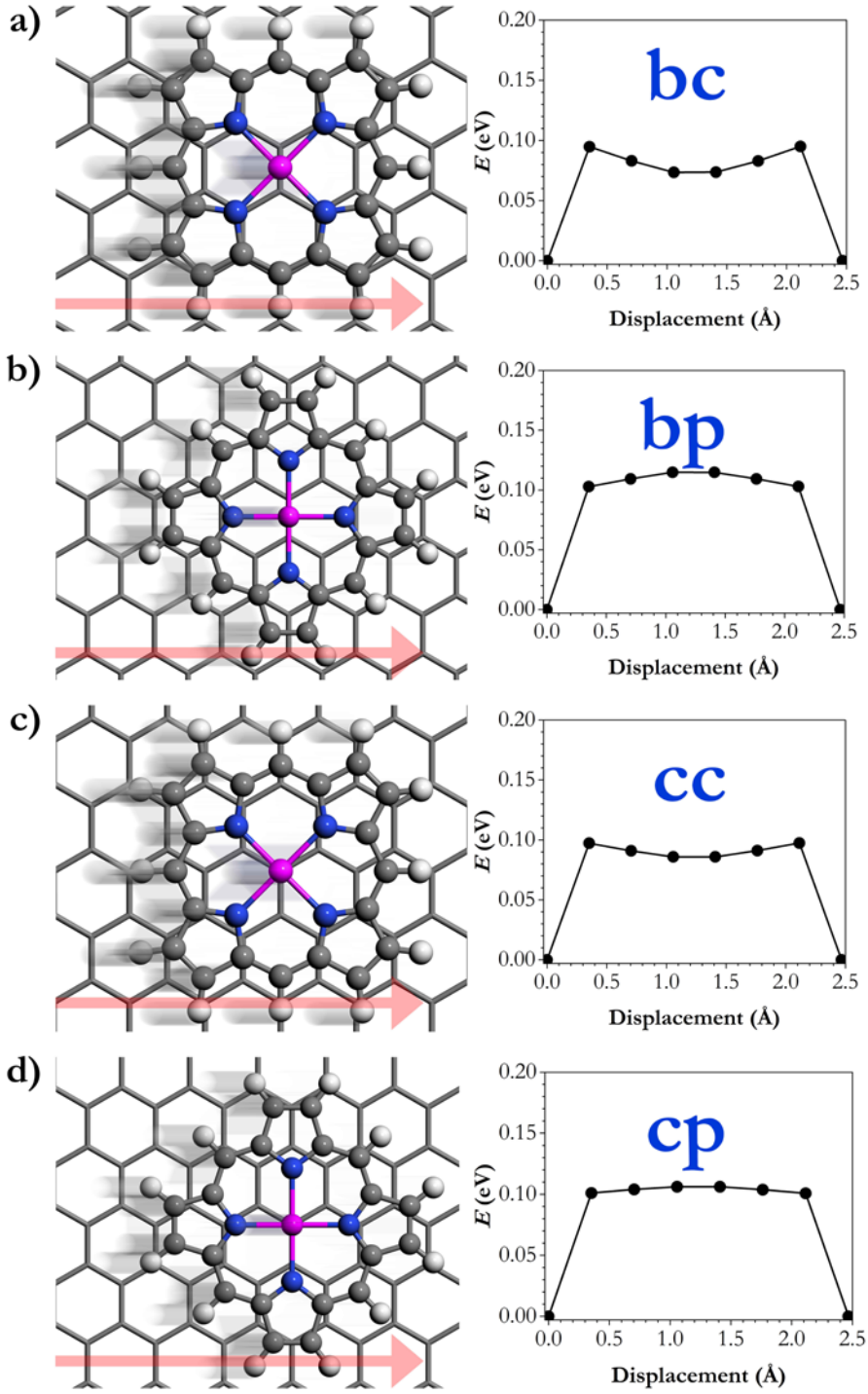

Figure 8.2. NEB calculated energy barrier for the translation of the porphyrin molecule towards the graphitic edge considering the a) bc, b) bp, c) cc and d) cp positions. Colour code: grey = carbon, white = hydrogen, blue = nitrogen and purple = zinc.

The NEB plots for the four positions exhibit energy barriers of around 0.1 eV which means that diffusion of the molecule will occur at any significant temperature. It also means that the molecules will easily reach the edge, where the adsorption can be expected to be stronger. The 'crossed' positions (bc and cc) exhibit a slightly lower energy barrier compared to the value obtained for the 'parallel' ones (bp and cp), which means that the bc and cc are slightly favourable for the translation towards the edge, regardless of the starting point (bond or carbon).

It is worth noting that the MEPs of 'crossed' positions (bc and cc) show a similar behaviour, having a local minimum at the middle of the path (**Figure 8.2a** and **c**), meanwhile the MEPs of 'parallel' positions (bp and cp) exhibit a local maximum at the same section of the path (**Figure 8.2b** and **d**). NEB calculations were done by Bhandary *et al.* [20] considering Fe-porphyrins (adsorbed on graphene with underlying Ni substrate) traveling from a hexagonal site (centre of the ring) to the top of a carbon atom, which is similar as our cc and cp positions. They found a diffusion barrier of about 33 meV, which indicates that Fe-porphyrins can diffuse easily from the hexagonal ground state adsorption site to the top of the next energetically available carbon atom at room temperature. This corroborates our calculated energy barriers which is in the same order of magnitude. However, it slightly varies from our results since ferrimagnetism induced in graphene by the underlying Ni substrate dictates the nature and strength of magnetic interaction between Fe-porphyrin and Ni substrate.

8.3.3 Single porphyrin unit at zigzag edges of graphene nanoribbon

In the previous section, we explored the ability of porphyrins to diffuse at the graphene surface. To complete this analysis, we considered two possible positions that a single porphyrin unit can be placed in the same plane as graphene when it reaches to the zigzag

edge: in the first one, the porphyrin unit is decorating the zigzag edge fusing the lateral β- and *meso*-carbon atoms with the edge (crossed-like position, see **Figure 8.3a**) and in the second, one of the porphyrin rings (only *meso*-carbon atoms) is used to place the molecule at the zigzag edge (parallel-like position, see **Figure 8.3b**).

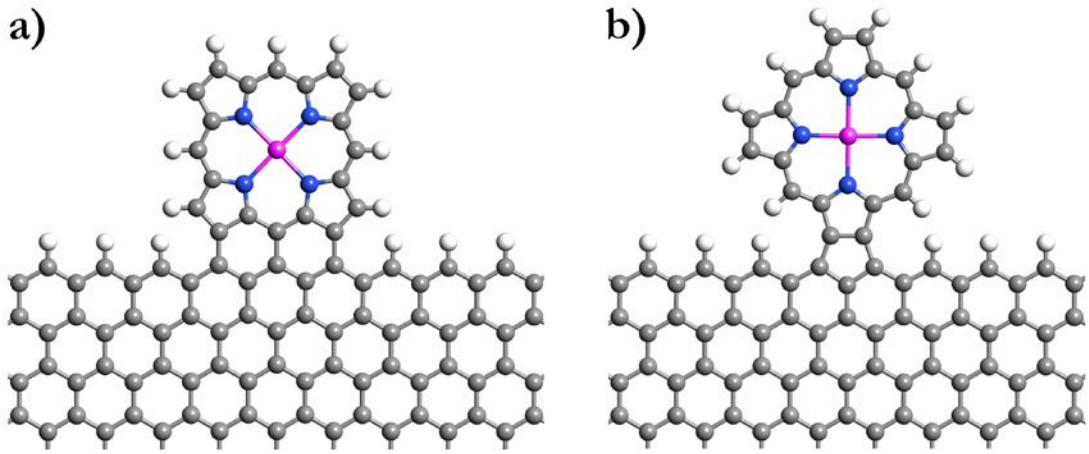

Figure 8.3. a) Crossed-like and b) parallel-like positions of a porphyrin unit at the zigzag edge. Colour code: grey = carbon, white = hydrogen, blue = nitrogen and purple = zinc.

Energy of formation (E_{form}) was calculated for those positions in a graphene nanoribbon having 0.66 eV and 1.18 eV for the crossed-like and parallel-like positions, respectively. Equations 8.1 and 8.2 were used to calculate E_{form} for crossed- and parallel-like positions, respectively:

$$E_{\text{form}} = \left(E_{\text{G+P}} + 3E_{\text{H}_2}\right) - \left(E_{\text{G}} + E_{\text{P}}\right) \quad (8.1)$$

$$E_{\text{form}} = \left(E_{\text{G+P}} + 2E_{\text{H}_2}\right) - \left(E_{\text{G}} + E_{\text{P}}\right) \quad (8.2)$$

where E_{G+P} is the energy of the complex formed by the nanoribbon with the porphyrin at the edge, E_{H_2} is the energy of hydrogen molecules evolved per adsorbed porphyrin (3 H_2 molecules for crossed-like position and 2 H_2 molecules for parallel-like position), and E_G and E_P are the energies of graphene nanoribbon and porphyrin molecule, respectively, considering all hydrogens saturating the carbon atoms.

The fact that these energies are positive means that the process of adsorption is endothermic. However, it will still be favourable entropically because H_2 gas is being evolved. The adsorption in the crossed-like position is the less endothermic, and it also evolves more H_2 gas than the adsorption in the parallel-like position. Therefore, we can expect that this one will be the dominant position. Experiments carried out by He *et al.* [21] showed that 97% of Al-porphyrin molecules were coupled to the graphene zigzag edge with the same alignment as our crossed-like position, which demonstrates our assumption as the preferred one, regardless of the metal at the centre of the porphyrin molecule.

In **Figure 8.3**, it is evident that the parallel-like position exhibit more strain to the graphene nanoribbon than the crossed-like due to a five-membered ring formed at the edge. Meanwhile, the crossed-like position follows the same honeycomb pattern of graphene, having as a result less strain on the whole structure.

8.4 Conclusions

In this Chapter, we have explored the interaction of porphyrins with the surface and edges of graphene.

Regarding the adsorption of porphyrin unit on top of graphene surface, bp is the most stable position, having an adsorption energy of -1.47 eV. The NEB analysis shows that diffusion of the molecule at the graphene surface takes place with a very small barrier in the order of 0.1 eV.

When porphyrin reaches the edge of graphene, it should be attached in a crossed-like configuration evolving 3 H_2 molecules per adsorbed porphyrin, which makes the process entropically driven.

Given the above results, it can be expected that porphyrin molecules in contact with graphene accumulate at the edges, which could be useful for photocatalytic applications.

8.5 References

1. Tripkovic, V., et al., *Electrochemical CO2 and CO Reduction on Metal-Functionalized Porphyrin-like Graphene.* The Journal of Physical Chemistry C, 2013. **117**(18): p. 9187-9195.
2. Geim, A.K. and K.S. Novoselov, *The rise of graphene.* Nature Materials, 2007. **6**: p. 183.
3. Pham, V.D., et al., *Molecular adsorbates as probes of the local properties of doped graphene.* Scientific Reports, 2016. **6**: p. 24796.
4. Loh, K.P., S.W. Tong, and J. Wu, *Graphene and Graphene-like Molecules: Prospects in Solar Cells.* Journal of the American Chemical Society, 2016. **138**(4): p. 1095-1102.
5. Lu, Q., et al., *2D Transition-Metal-Dichalcogenide-Nanosheet-Based Composites for Photocatalytic and Electrocatalytic Hydrogen Evolution Reactions.* Advanced Materials, 2015. **28**(10): p. 1917-1933.
6. Yang, M.-Q., et al., *Artificial photosynthesis over graphene–semiconductor composites. Are we getting better?* Chemical Society Reviews, 2014. **43**(24): p. 8240-8254.
7. Dasler, D., et al., *Direct Covalent Coupling of Porphyrins to Graphene.* Journal of the American Chemical Society, 2017. **139**(34): p. 11760-11765.
8. Zeng, J. and K.-Q. Chen, *A nearly perfect spin filter and a spin logic gate based on a porphyrin/graphene hybrid material.* Physical Chemistry Chemical Physics, 2018. **20**(6): p. 3997-4004.
9. Wojcik, A. and P.V. Kamat, *Reduced Graphene Oxide and Porphyrin. An Interactive Affair in 2-D.* ACS Nano, 2010. **4**(11): p. 6697-6706.

10. Bala Murali Krishna, M., et al., *Synthesis and structural, spectroscopic and nonlinear optical measurements of graphene oxide and its composites with metal and metal free porphyrins.* Journal of Materials Chemistry, 2012. **22**(7): p. 3059-3068.

11. Geng, J., et al., *Preparation of graphene relying on porphyrin exfoliation of graphite.* Chemical Communications, 2010. **46**(28): p. 5091-5093.

12. Kresse, G., Furthmüller, J., *Efficient iterative schemes for ab initio total-energy calculations using a plane-wave basis set.* Phys. Rev. B: Condens. Matter Mater. Phys., 1996. **54**(16): p. 11169 - 11186.

13. Kresse, G., Furthmüller, J., *Efficiency of ab-initio total energy calculations for metals and semiconductors using a plane-wave basis set.* Comput. Mater. Sci., 1996. **6**: p. 15 - 50.

14. Perdew, J.P., K. Burke, and M. Ernzerhof, *Generalized Gradient Approximation Made Simple.* Physical Review Letters, 1996. **77**(18): p. 3865-3868.

15. Perdew, J.P., K. Burke, and M. Ernzerhof, *Generalized Gradient Approximation Made Simple [Phys. Rev. Lett. 77, 3865 (1996)].* Physical Review Letters, 1997. **78**(7): p. 1396-1396.

16. Kresse, G. and D. Joubert, *From ultrasoft pseudopotentials to the projector augmented-wave method.* Phys. Rev. B, 1999. **59**(3): p. 1758-1775.

17. Butler, K.T., C.H. Hendon, and A. Walsh, *Electronic Chemical Potentials of Porous Metal–Organic Frameworks.* Journal of the American Chemical Society, 2014. **136**(7): p. 2703-2706.

18. Cooper, D.R., et al., *Experimental Review of Graphene.* ISRN Condensed Matter Physics, 2012. **2012**: p. 501686.

19. Henkelman, G., B.P. Uberuaga, and H. Jónsson, *A climbing image nudged elastic band method for finding saddle points and minimum energy paths.* The Journal of Chemical Physics, 2000. **113**(22): p. 9901-9904.

20. Bhandary, S., O. Eriksson, and B. Sanyal, *Defect controlled magnetism in FeP/graphene/Ni(111).* Scientific Reports, 2013. **3**(1): p. 3405.

21. He, Y., et al., *Fusing tetrapyrroles to graphene edges by surface-assisted covalent coupling.* Nature Chemistry, 2017. **9**(1): p. 33-38.

9 Future work

Overall, this thesis described how computer simulations of carbon-based and porphyrin-based nanostructures can be useful to study and analyse their potential applications in catalysis and photocatalysis. However, as the possibilities of different combinations, designs and structures are only limited by our imagination, there is always an opportunity for future students and researchers to take this work and develop or improve the ideas and applications of the nanostructures already described.

9.1 Considering other metals at the porphyrin centre of the 2D PMOFs

As described in **Chapter 7.3.3**, it is possible to consider other types of atoms at the centre of the porphyrin. For example, the presence of Mn atoms within the porphyrin unit has been studied by Sharma *et al.* [1] where they considered a porphyrin-based MOF with Mn(II) centres as a visible light responsive device. They showed that it is possible to achieve a photocatalytic cycloaddition of CO_2 with epoxides to generate cyclic carbonates at mild conditions. The enhanced catalytic activity has been attributed to visible light absorption of porphyrin metalloligand leading to photo-thermal effect which facilitates the activation of the Mn catalytic site.

Another possible metal to be considered at the centre of the porphyrin unit could be the Fe atom. As mentioned in **Chapter 7.1**, when iron atoms are present the position of the conduction band edge is lowered significantly and also an occupied d_{xy} state is

introduced in the gap region above the valence band [2, 3]. Iron is therefore an ideal metal centre useful to engineer the band structures of this kind of porphyrin-based MOFs.

This gives as an idea of the effect of Mn or Fe atoms when they are present inside the porphyrin units, and as a possible future project could be to consider a full set of new metals including these suggestions and study their band alignment and perform TD-DFT calculations to know their photophysical behaviour under visible light.

9.2 Electron transfer in hybrid graphene-porphyrin structures

In **Chapter 8**, we showed how porphyrin molecules are capable of diffusing easily towards the edges of graphene to be used as potential photocatalysts. However, it is important to discuss charge transfer between porphyrin units and graphene since it would be the key to improve the photophysical properties of this kind of hybrid materials.

Given the size of the models employed in this study, we have been unable to obtain results that are precise enough (in terms of the grid used to represent the charge density) to do a reliable analysis of charge transfer. This is something that should be investigated in the future, when computers with larger memory are available. If electrons move towards the graphene nanosheet, that would mean that the porphyrin is acting as an electron donor to the graphene, suggesting a very different kind of interaction from the simple dispersion-based attraction that is often assumed.

Also, a full set of different metals at the centre of the porphyrin molecules could be considered to study their effect when they are in contact with the graphene surface or edges. This study could be done employing the same methods (PBE-D3) and could be compared with a nonlocal functional, such as optPBE-vdW (as explained in **Chapter 2.6.3**), to describe in a proper way the dispersion interactions.

9.3 References

1. Sharma, N., S.S. Dhankhar, and C.M. Nagaraja, *A Mn(II)-porphyrin based metal-organic framework (MOF) for visible-light-assisted cycloaddition of carbon dioxide with epoxides.* Microporous and Mesoporous Materials, 2019. **280**: p. 372-378.
2. Aziz, A., et al., *Porphyrin-based metal-organic frameworks for solar fuel synthesis photocatalysis: band gap tuning via iron substitutions.* Journal of Materials Chemistry A, 2017. **5**(23): p. 11894-11904.
3. Hamad, S., et al., *Electronic structure of porphyrin-based metal–organic frameworks and their suitability for solar fuel production photocatalysis.* Journal of Materials Chemistry A, 2015. **3**(46): p. 23458-23465.

10 Concluding remarks

In this thesis we have theoretically investigated graphitic and porphyrin-based nanostructures with a range of potential applications (mainly in catalysis or photocatalysis). Some of this work has been done in collaboration with experimentalists, and trying to explain measured properties, while in other cases the work has been purely computational and with a predictive purpose.

Graphite (or few-layer graphene) can be strongly influenced by the edge structure of the graphene planes and our analysis of the thermodynamics of edge folding indicates a preference for multiple concentric folds at the edges, as seen in experiments. Also, we have presented the interaction between graphitic edges and ferrihydrite-like nanostructure and our density functional theory (DFT) calculations showed evidence that the C/ferrihydrite interface is stabilised in presence of pyridinic nitrogen, which is accompanied by charge transfer from N atom to Fe ion. This result has been corroborated with near edge X-ray absorption fine structure (NEXAFS) spectrum of a Fe/N-C sample. Our calculations through this ferrihydrite-like model together with our proposed sets of single-atom Fe sites in graphitic structures suggest that these systems could represent a promising collection of electrocatalysts.

Moving on to the porphyrin realm, we demonstrated that their multifunctionality lies in the combination of the metal and its rigid planar aromatic structure which allows such complexes to play relevant roles in electron transfer, light-harvesting and photocatalytic processes. Through the examination of band structures, we showed that it is possible to design porphyrin nanostructures with specific band gap values by varying the type of linkage used between each porphyrin. Another approach to this purpose has been

explored in our 2D porphyrin-paddlewheel MOFs, where we explained how their band structure and optical properties can be tailored by changing the nature of the metallic centre of porphyrins, as well as the metallic ions at the paddlewheel. Both studies have led us to conclude that the photoreceptor and functional groups of different lengths (linkers or bridges) within and between porphyrin units, respectively, are vital specifications to design promising photocatalytic materials.

As we can see, porphyrins are excellent for photocatalytic purposes so graphitic structures can take advantage of porphyrin features to enhance their electrocatalytic performance. The combination a porphyrin/graphene framework concept has an incredible catalytic potential exhibited in the last chapter where we gave useful insights in terms of interactions between both.

We sincerely hope that our contributions will inspire further theoretical and also experimental studies towards the understanding of carbon-based, porphyrin-based and hybrid carbon-porphyrin nanostructures.

Appendix

Excited states of Cu-paddlewheel / Zn-porphyrin system

The TD-DFT calculations used to support our results in **Chapter 7** were mostly performed in the group of Dr Rachel Crespo-Otero at Queen Mary University of London, with only small contributions from me (in the creation of models and in the interpretation). The model we have employed for the TD-DFT calculation of excited stated in the Cu-Zn-TCPP system is shown in **Figure A1**.

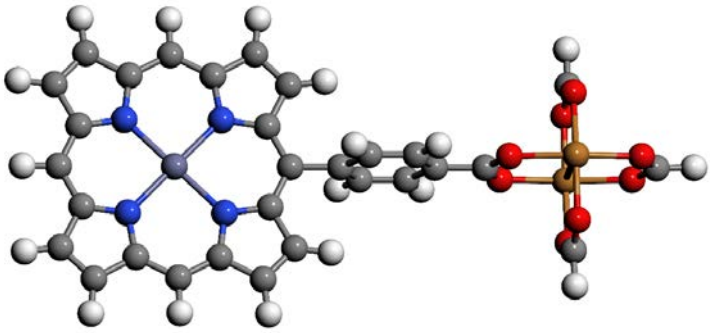

Figure A1. Molecular model of Cu-Zn-porphyrin system. Colour code: grey = carbon, red = oxygen, white = hydrogen, blue = nitrogen and orange = copper.

The excited states energies and oscillator strengths obtained for this model are presented in **Table A1**, and the atomic (Bader) charges in **Table A2**.

Table A1. Excited states and oscillator strengths calculated for the Cu-Zn-TCPP system. Bright states are highlighted in orange.

States	Energy (eV)	Oscillator strength
T_1	1.43	0.00
T_2	1.50	0.00
T_3	1.61	0.00
T_4	1.62	0.00

T_5	1.86	0.00
T_6	1.91	0.00
T_7	1.93	0.00
T_8	2.01	0.00
T_9	2.01	0.00
T_{10}	2.01	0.00
T_{11}	2.02	0.00
T_{12}	2.24	0.02
T_{13}	2.24	0.01
T_{14}	2.28	0.00
T_{15}	2.28	0.00
T_{16}	2.29	0.00
T_{17}	2.38	0.00
T_{18}	2.38	0.00
T_{19}	2.86	0.00
T_{20}	2.86	0.00
T_{21}	2.89	0.00
T_{22}	2.90	0.00
T_{23}	3.08	0.00
T_{24}	3.14	0.00
T_{25}	3.15	0.00
T_{26}	3.16	0.00
T_{27}	3.17	0.00
T_{28}	3.22	0.00
T_{29}	3.24	0.00
T_{30}	3.24	0.00
T_{31}	3.26	0.00
T_{32}	3.27	0.00
T_{33}	3.28	0.00
T_{34}	3.28	0.00
T_{35}	3.29	0.00
T_{36}	3.29	0.00
T_{37}	3.31	0.00
T_{38}	3.33	0.00
T_{39}	3.33	0.00
T_{40}	3.36	0.00
T_{41}	3.41	0.00
T_{42}	3.42	0.00
T_{43}	3.44	0.00
T_{44}	3.44	1.47
T_{45}	3.45	0.00
T_{46}	3.46	0.83
T_{47}	3.56	0.00
T_{48}	3.57	0.00
T_{49}	3.57	0.00
T_{50}	3.61	0.00
T_{51}	3.64	0.00
T_{52}	3.66	0.00
T_{53}	3.70	0.00
T_{54}	3.70	0.00
T_{55}	3.73	0.01

T_{56}	3.74	0.00
T_{57}	3.76	0.00
T_{58}	3.80	0.07
T_{59}	3.81	0.03
T_{60}	3.81	0.03
T_{61}	3.84	0.02
T_{62}	3.86	0.00
T_{63}	3.87	0.02
T_{64}	3.89	0.00
T_{65}	3.98	0.00
T_{66}	4.00	0.00
T_{67}	4.08	0.00
T_{68}	4.09	0.00
T_{69}	4.11	0.00
T_{70}	4.14	0.00
T_{71}	4.18	0.00
T_{72}	4.19	0.00
T_{73}	4.20	0.00
T_{74}	4.21	0.16
T_{75}	4.22	0.30

Table A2. Bader charges of the Cu-Zn-TCPP system, calculated for the paddlewheel, bridge and porphyrin units (ΔQ_{PW}, ΔQ_{bridge} and ΔQ_{porph}, respectively), for the ground state, first excited state, and the two brightest states (highlighted in orange). The oscillator strengths are also shown.

States	ΔQ_{PW}	ΔQ_{bridge}	ΔQ_{porph}	Oscillator strength
T_0	0	0	0	-
T_1	-0.72	-0.04	0.76	0.00
T_{44}	0	0	0	1.47
T_{46}	0	0	0	0.83

Excited states after partial reduction of porphyrin to chlorin

The structural model used is shown in **Figure A2**. The excited states energies and oscillator strengths obtained for this model are presented in **Table A3** and the Bader charges are in **Table A4**.

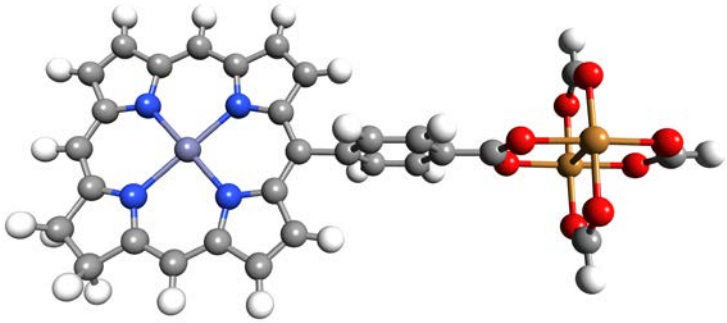

Figure A2. Molecular model of Cu-Zn-chlorin system. Colour code: grey = carbon, red = oxygen, white = hydrogen, blue = nitrogen and orange = copper.

Table A3. Excited states and oscillator strengths calculated for the Cu-Zn-chlorin system. Bright states are highlighted in orange.

States	Energy (eV)	Oscillator strength
T_1	1.10	0.00
T_2	1.43	0.00
T_3	1.44	0.00
T_4	1.52	0.00
T_5	1.61	0.00
T_6	1.86	0.00
T_7	1.91	0.00
T_8	2.01	0.00
T_9	2.01	0.00
T_{10}	2.03	0.00
T_{11}	2.24	0.02
T_{12}	2.24	0.01
T_{13}	2.28	0.00
T_{14}	2.28	0.00
T_{15}	2.29	0.00
T_{16}	2.31	0.13
T_{17}	2.36	0.00
T_{18}	2.46	0.01
T_{19}	2.71	0.00
T_{20}	2.77	0.00
T_{21}	2.93	0.00
T_{22}	2.96	0.00

T_{23}	2.98	0.00
T_{24}	3.02	0.00
T_{25}	3.02	0.00
T_{26}	3.06	0.00
T_{27}	3.10	0.00
T_{28}	3.13	0.00
T_{29}	3.18	0.00
T_{30}	3.19	0.00
T_{31}	3.28	0.00
T_{32}	3.29	0.00
T_{33}	3.29	0.00
T_{34}	3.31	0.00
T_{35}	3.35	0.00
T_{36}	3.39	0.00
T_{37}	3.39	0.00
T_{38}	3.43	0.01
T_{39}	3.43	0.00
T_{40}	3.44	0.00
T_{41}	3.45	0.86
T_{42}	3.48	0.88
T_{43}	3.53	0.00
T_{44}	3.57	0.00
T_{45}	3.60	0.00
T_{46}	3.60	0.11
T_{47}	3.61	0.00
T_{48}	3.62	0.00
T_{49}	3.62	0.00
T_{50}	3.64	0.04
T_{51}	3.78	0.00
T_{52}	3.82	0.00
T_{53}	3.84	0.04
T_{54}	3.86	0.00
T_{55}	3.87	0.02
T_{56}	3.94	0.22
T_{57}	4.02	0.00
T_{58}	4.03	0.00
T_{59}	4.04	0.00
T_{60}	4.05	0.00
T_{61}	4.07	0.00
T_{62}	4.08	0.00
T_{63}	4.09	0.00
T_{64}	4.10	0.00
T_{65}	4.10	0.01
T_{66}	4.11	0.00
T_{67}	4.14	0.00
T_{68}	4.14	0.00
T_{69}	4.14	0.05
T_{70}	4.15	0.00
T_{71}	4.17	0.00
T_{72}	4.17	0.00
T_{73}	4.23	0.03

T_{74}	4.25	0.00
T_{75}	4.27	0.00

Table A4. Bader charges of the Cu-Zn-chlorin system, calculated for the paddlewheel, bridge and porphyrin units (ΔQ_{PW}, ΔQ_{bridge} and ΔQ_{porph}, respectively), for the ground state, first excited state, and the two brightest states (highlighted in orange). The oscillator strengths are also shown.

States	ΔQ_{PW}	ΔQ_{bridge}	ΔQ_{porph}	Oscillator strength
T_0	0	0	0	
T_1	-0.83	0.05	0.78	0.00
T_{16}	0	-0.01	0.01	0.13
T_{41}	-0.01	0.11	-0.10	0.86

Excited states of system with C2 bridge

The model for the system with a C2 bridge between the porphyrin and the paddlewheel is shown in **Figure A3**. The excited states energies and oscillator strengths are presented in **Table A5**, and the Bader charges in **Table A6**.

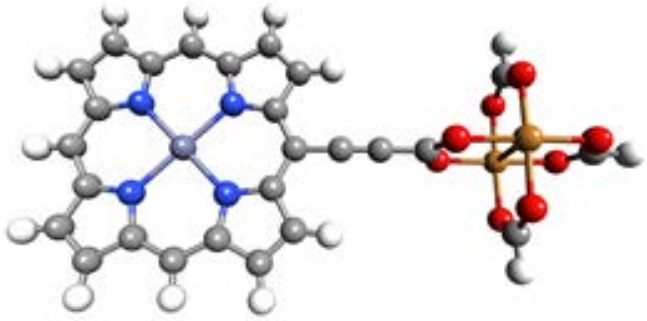

Figure A3. Molecular model for the system where the benzene bridge is substituted by an ethyne (C2) bridge. Colour code: grey = carbon, red = oxygen, white = hydrogen, blue = nitrogen and orange = copper.

Table A5. Excited states and oscillator strengths calculated for the Cu-Zn-C2 system. Bright states are highlighted in orange.

States	Energy (eV)	Oscillator strength
T_1	1.40	0.04
T_2	1.54	0.00
T_3	1.57	0.06
T_4	1.65	0.00
T_5	1.89	0.00
T_6	1.93	0.00
T_7	1.95	0.00
T_8	2.00	0.00
T_9	2.03	0.00
T_{10}	2.04	0.00
T_{11}	2.08	0.00
T_{12}	2.24	0.02
T_{13}	2.24	0.01
T_{14}	2.27	0.00
T_{15}	2.28	0.00
T_{16}	2.29	0.00
T_{17}	2.31	0.00
T_{18}	2.32	0.02
T_{19}	2.86	0.03
T_{20}	2.93	0.00
T_{21}	2.99	0.00
T_{22}	3.04	0.00

T_{23}	3.04	0.00
T_{24}	3.05	0.05
T_{25}	3.12	0.00
T_{26}	3.15	0.00
T_{27}	3.17	0.00
T_{28}	3.18	0.00
T_{29}	3.22	0.03
T_{30}	3.27	0.66
T_{31}	3.30	0.00
T_{32}	3.32	0.02
T_{33}	3.34	0.73
T_{34}	3.34	0.10
T_{35}	3.37	0.00
T_{36}	3.41	0.56
T_{37}	3.44	0.00
T_{38}	3.46	0.00
T_{39}	3.46	0.00
T_{40}	3.49	0.00
T_{41}	3.53	0.00
T_{42}	3.54	0.00
T_{43}	3.55	0.00
T_{44}	3.57	0.00
T_{45}	3.64	0.00
T_{46}	3.66	0.05
T_{47}	3.66	0.00
T_{48}	3.67	0.00
T_{49}	3.67	0.00
T_{50}	3.68	0.05
T_{51}	3.69	0.00
T_{52}	3.70	0.00
T_{53}	3.74	0.00
T_{54}	3.75	0.00
T_{55}	3.79	0.00
T_{56}	3.80	0.00
T_{57}	3.82	0.04
T_{58}	3.83	0.01
T_{59}	3.86	0.02
T_{60}	3.90	0.02
T_{61}	3.90	0.00
T_{62}	3.93	0.00
T_{63}	3.93	0.00
T_{64}	3.94	0.01
T_{65}	3.96	0.01
T_{66}	4.09	0.00
T_{67}	4.09	0.22
T_{68}	4.10	0.00
T_{69}	4.16	0.00
T_{70}	4.16	0.00
T_{71}	4.21	0.00
T_{72}	4.22	0.11
T_{73}	4.26	0.00

T_{74}	4.26	0.01
T_{75}	4.27	0.00

Table A6. Bader charges of the Cu-Zn-C2 system, calculated for the paddlewheel, bridge and porphyrin units (ΔQ_{PW}, ΔQ_{bridge} and ΔQ_{porph}, respectively), for the ground state and some relevant excited states. The oscillator strengths are also shown.

States	ΔQ_{PW}	ΔQ_{bridge}	ΔQ_{porph}	Oscillator strength
T_0	0	0	0	-
T_1	-0.31	0.03	0.28	0.04
T_3	-0.33	0.03	0.30	0.06
T_{30}	-0.34	0.05	0.29	0.66
T_{33}	0	0.03	-0.03	0.73
T_{34}	-0.48	-0.11	0.59	0.10
T_{36}	-0.23	0.06	0.17	0.56